

# **Design and Implementation of Flight Dynamics Control Strategies for a Smartphone-based Quadrotor**

Thesis for obtaining the degree of

**MASTER OF SCIENCE IN ENGINEERING**  
with emphasis in Automation

**Alejandro Astudillo Vigoya**

[alejandro.astudillo@correounivalle.edu.co](mailto:alejandro.astudillo@correounivalle.edu.co)



School of Electrical and Electronic Engineering  
UNIVERSIDAD DEL VALLE  
Cali, COLOMBIA

December 4, 2017



*Supervised by:*

Dr.-Ing. Esteban Rosero  
Industrial Control Research Group - GICI  
School of Electrical and Electronic Engineering  
Universidad del Valle

Bladimir Bacca Ph.D.  
Perception and Intelligent Systems Research Group - PSI  
School of Electrical and Electronic Engineering  
Universidad del Valle



# **Abstract**

The field of autonomous systems control is young, but operational experience is rapidly growing, making research on collaborative systems of great importance. Improving aerial robots in particular could be key in facing future environmental challenges..... In this work, two main problems are addressed: the cooperative source seeking problem and the cooperative level curve tracking problem by a group of agents under undirected constrained communications. .....



# **Resumen**

The field of autonomous systems control is young, but operational experience is rapidly growing, making research on collaborative systems of great importance. Improving aerial robots in particular could be key in facing future environmental challenges..... In this work, two main problems are addressed: the cooperative source seeking problem and the cooperative level curve tracking problem by a group of agents under undirected constrained communications. .....



# Contents

<b>Abstract</b>	v
<b>Resumen</b>	vii
<b>List of Figures</b>	xiii
<b>List of Tables</b>	xvii
<b>1 Introduction</b>	3
1.1 Unmanned Aircraft Vehicles (UAV) . . . . .	3
1.1.1 Fixed-Wing UAVs . . . . .	4
1.1.2 Rotary-Wing UAVs . . . . .	5
1.2 Literature Review . . . . .	6
1.2.1 Control Strategies and State Estimation in Quadrotors . . . . .	6
1.2.2 Quadrotor Flight Modes . . . . .	8
1.2.3 Smartphones in Control Systems . . . . .	9
1.2.4 Smartphone-based Quadrotors . . . . .	10
1.3 Motivation . . . . .	12
1.4 Research Problem . . . . .	13
1.5 Objectives . . . . .	13
1.6 Outline . . . . .	14
<b>2 Dynamic Model of the Quadrotor</b>	15
2.1 Quadrotors Configurations . . . . .	15
2.1.1 The ‘+’ Configuration . . . . .	16
2.1.2 The ‘X’ Configuration . . . . .	18
2.2 Non-linear Model . . . . .	21
2.2.1 Newton-Euler Approach . . . . .	21
2.2.2 Euler-Lagrange Approach . . . . .	25
2.3 Linearized Model . . . . .	28
2.3.1 Jacobian Linearization . . . . .	28
2.3.2 Thrust Compensation . . . . .	29
2.4 Conclusions . . . . .	30

<b>3 Smartphone-based Quadrotor Prototype</b>	<b>31</b>
3.1 Quadrotor Components . . . . .	32
3.1.1 Frame . . . . .	32
3.1.2 Smartphone . . . . .	33
3.1.3 Motors and Electronic Speed Controllers . . . . .	34
3.1.4 Smartphone-to-ESC Gateway . . . . .	35
3.1.5 Battery . . . . .	36
3.1.6 3D-printed Parts . . . . .	37
3.1.7 Assembled Smartphone-based Quadrotor . . . . .	39
3.2 Quadrotor Parameters . . . . .	40
3.2.1 Mass . . . . .	40
3.2.2 Moments of Inertia . . . . .	41
3.2.3 Motors Thrust . . . . .	44
3.2.4 Motors Torque . . . . .	45
3.3 Conclusions . . . . .	47
<b>4 Control Strategies and State Estimation</b>	<b>49</b>
4.1 Concept and Generalities . . . . .	50
4.1.1 State Space Representation . . . . .	50
4.1.2 Controllability and Observability . . . . .	50
4.2 Control Strategies . . . . .	51
4.2.1 Linear Quadratic Integral (LQI) Controller . . . . .	52
4.2.2 $H_\infty$ Controller . . . . .	55
4.3 Controllers Design and Simulation . . . . .	57
4.3.1 Stabilize Mode . . . . .	57
4.3.2 Altitude Hold Mode . . . . .	61
4.3.3 GNSS-Dependent Flight Modes . . . . .	67
4.4 State Estimation Through Kalman Filter . . . . .	73
4.4.1 Attitude Estimation . . . . .	73
4.4.2 Position Measurement . . . . .	74
4.4.3 States Estimation . . . . .	74
4.5 Conclusions . . . . .	76
<b>5 Implementation and Results</b>	<b>77</b>
5.1 Android Application . . . . .	77
5.2 Ground Control Station . . . . .	78
5.3 Flight Tests . . . . .	79
5.3.1 Stabilize Mode . . . . .	79
5.3.2 Altitude Hold Mode . . . . .	81
5.3.3 GNSS-Dependent Mode . . . . .	84
5.4 Conclusions . . . . .	86
<b>6 Conclusions and Outlook</b>	<b>87</b>

<b>Appendix A Publications</b>	<b>89</b>
<b>Appendix B Supplementary Material</b>	<b>91</b>
<b>Appendix C Control Signals in Flight Tests</b>	<b>93</b>
<b>Bibliography</b>	<b>113</b>



# List of Figures

1.1	Skywalker X8 Fixed-wing UAV . . . . .	4
1.2	Altavian Octorotor Rotary-wing UAV . . . . .	5
1.3	Quadrotor aircraft X650 . . . . .	6
1.4	Smartphone-based ball tracking robot . . . . .	10
1.5	UPenn's smartphone-based quadrotor . . . . .	11
2.1	Quadrotor geometry in '+' configuration . . . . .	16
2.2	Quadrotor geometry in 'X' configuration . . . . .	19
3.1	Quadrotor prototype's hardware overview . . . . .	31
3.2	LJI 500-X4 carbon fiber frame . . . . .	32
3.3	LG Nexus 5X, smartphone used as flight controller . . . . .	33
3.4	Motors and ESC used in the Quadrotor <sup>1</sup> . . . . .	35
3.5	Arduino Mega ADK . . . . .	36
3.6	LiPo battery that powers the Quadrotor . . . . .	37
3.7	Smartphone support . . . . .	38
3.8	Arduino Mega ADK and EMAX 4in1 ESCs designed supports . . . . .	38
3.9	3D Designed Dome . . . . .	39
3.10	Assembled Smartphone-based Quadrotor Prototype . . . . .	40
3.11	Bifilar pendulum experiment geometry for inertia identification . . . . .	42
3.12	Rotation about $x$ , $y$ and $z$ axes during the bifilar pendulum experiments . . . . .	43
3.13	Thrust test configuration . . . . .	44
3.14	Motors thrust test results . . . . .	45
3.15	Motors torque experiment configuration . . . . .	46
3.16	Motors torque experiment results . . . . .	47
4.1	Closed-loop system with LQI controller for reference tracking . . . . .	54
4.2	Control loop with generalized plant . . . . .	55
4.3	Generalized plant with the weighting filters $W_s$ and $W_k$ . . . . .	56
4.4	Closed-loop response of stabilize mode controlled by a LQI controller . . . . .	59
4.5	Upper bounded singular values of $S$ and $K_H S$ in stabilize mode . . . . .	60
4.6	HSV energy histogram of $K_H$ in stabilize mode . . . . .	61
4.7	Closed-loop response of stabilize mode controlled by a $H_\infty$ controller . . . . .	62

4.8	Closed-loop response of altitude hold mode controlled by a LQI controller . . . . .	64
4.9	Upper bounded singular values of $S$ and $K_H S$ in altitude hold mode . . . . .	65
4.10	HSV energy histogram of $K_H$ in altitude hold mode . . . . .	66
4.11	Closed-loop response of altitude hold mode controlled by a $H_\infty$ controller . . . . .	66
4.12	Position response of the GNSS-Dependent modes with a LQI controller . . . . .	69
4.13	Attitude response of the GNSS-Dependent modes with a LQI controller . . . . .	69
4.14	Upper bounded singular values of $S$ and $K_H S$ in GNSS-Dependent modes . . . . .	70
4.15	HSV energy histogram of $K_H$ in GNSS-Dependent modes . . . . .	71
4.16	Position response of the GNSS-Dependent modes with a $H_\infty$ controller . . . . .	72
4.17	Attitude response of the GNSS-Dependent modes with a $H_\infty$ controller . . . . .	72
4.18	Static test of the smartphone GNSS receiver and barometer . . . . .	75
5.1	HSV energy histogram of $K_H$ in GNSS-Dependent modes . . . . .	77
5.2	HSV energy histogram of $K_H$ in GNSS-Dependent modes . . . . .	78
5.3	Rotation about $x$ , $y$ and $z$ axes during the bifilar pendulum experiments . . . . .	79
5.4	Rotation about $x$ , $y$ and $z$ axes during the bifilar pendulum experiments . . . . .	80
5.5	Rotation about $x$ , $y$ and $z$ axes during the bifilar pendulum experiments . . . . .	81
5.6	Rotation about $x$ , $y$ and $z$ axes during the bifilar pendulum experiments . . . . .	82
5.7	Closed-loop of the controlled system with an $H_\infty$ controller. . . . .	83
5.8	Rotation about $x$ , $y$ and $z$ axes during the bifilar pendulum experiments . . . . .	84
5.9	Closed-loop of the controlled system with an $H_\infty$ controller. . . . .	85
5.10	Rotation about $x$ , $y$ and $z$ axes during the bifilar pendulum experiments . . . . .	85
C.1	Rotation about $x$ , $y$ and $z$ axes during the bifilar pendulum experiments . . . . .	94
C.2	Rotation about $x$ , $y$ and $z$ axes during the bifilar pendulum experiments . . . . .	95
C.3	Rotation about $x$ , $y$ and $z$ axes during the bifilar pendulum experiments . . . . .	96
C.4	Rotation about $x$ , $y$ and $z$ axes during the bifilar pendulum experiments . . . . .	97
C.5	Rotation about $x$ , $y$ and $z$ axes during the bifilar pendulum experiments . . . . .	98
C.6	Rotation about $x$ , $y$ and $z$ axes during the bifilar pendulum experiments . . . . .	99
C.7	Rotation about $x$ , $y$ and $z$ axes during the bifilar pendulum experiments . . . . .	100
C.8	Rotation about $x$ , $y$ and $z$ axes during the bifilar pendulum experiments . . . . .	101
C.9	Rotation about $x$ , $y$ and $z$ axes during the bifilar pendulum experiments . . . . .	102
C.10	Rotation about $x$ , $y$ and $z$ axes during the bifilar pendulum experiments . . . . .	103
C.11	Rotation about $x$ , $y$ and $z$ axes during the bifilar pendulum experiments . . . . .	104
C.12	Rotation about $x$ , $y$ and $z$ axes during the bifilar pendulum experiments . . . . .	105
C.13	Closed-loop of the controlled system with an $H_\infty$ controller. . . . .	106
C.14	Rotation about $x$ , $y$ and $z$ axes during the bifilar pendulum experiments . . . . .	106
C.15	Rotation about $x$ , $y$ and $z$ axes during the bifilar pendulum experiments . . . . .	107
C.16	Rotation about $x$ , $y$ and $z$ axes during the bifilar pendulum experiments . . . . .	108
C.17	Closed-loop of the controlled system with an $H_\infty$ controller. . . . .	109

- C.18 Rotation about  $x$ ,  $y$  and  $z$  axes during the bifilar pendulum experiments 109  
C.19 Rotation about  $x$ ,  $y$  and  $z$  axes during the bifilar pendulum experiments 110  
C.20 Rotation about  $x$ ,  $y$  and  $z$  axes during the bifilar pendulum experiments 111



# List of Tables

3.1	Sample Rates of the Sensors in the Smartphone . . . . .	34
3.2	Maximum Power Consumption of the Quadrotor's Components . . . . .	37
3.3	Mass values of all the Quadrotor's components . . . . .	41
3.4	Bifilar pendulum experiment results . . . . .	43







# Chapter 1

## Introduction

In recent years, the interest in unmanned aircraft vehicles (UAVs) research, has increased substantially. This is due to the several potential new services that this type of robotic devices offers, such as search and rescue, observation, mapping, inspection, etc. On the other hand, smartphones have become essential devices for humans and easily acquirable development tools. The interaction between these two technologies allows the development of low cost aerial robots based on an everyday item such as smartphones, facilitating both the distribution of its control software and its implementation by other researchers.

### 1.1 Unmanned Aircraft Vehicles (UAV)

An UAV is an aircraft capable of flying without having a human on board. These aircrafts are commonly known as ‘drones’ due to the similarity of the sound they produce with that of a male bee (drone). Although they can perform flight missions in a completely autonomous way, the UAVs are complemented with remote display and control systems (Ground Control Station - GCS), and communication systems between the UAV and the GCS. These three components describe what is known as Unmanned Aircraft Systems (UAS).

The UAS were initially designed for military applications, where the presence of a human could be of high risk [1]. However, their use has been widely extended to multiple applications such as education [2], agriculture [3], search and rescue [4], delivery [5], research [6], among others.

UAVs are modelled as rigid bodies with freedom of movement in a three-dimensional space, hence have six degrees of freedom (*DoF*), three translational (position) and three rotational (attitude). These aircrafts are classified mainly according to the propulsion direction exerted by the actuators. Thus, there are two groups of UAVs:

Fixed-wing and Rotary-wing UAVs, which are described below.

### 1.1.1 Fixed-Wing UAVs

A fixed-wing UAV is an aircraft which consists of an airframe attached to a rigid wing that generate lift using the UAVs forward airspeed and geometry. This type of UAVs need a constant forward movement in order to produce air flow around its wing, which can be generated by the thrust of propeller pushing the air flow in opposite direction of the UAV movement, or flying against to the wind. An example of a fixed-wing UAV is shown in Fig. 1.1.



Figure 1.1: Skywalker X8 Fixed-wing UAV<sup>1</sup>

Since they need a minimum airspeed to achieve their lift in flight, these aircrafts require a runway or catapult for take-off and landing. However, its geometry allows to achieve long-term flights (greater than 60 minutes) at high speeds (greater than  $20 \text{ m/s}$ ) by taking advantage of its aerodynamic efficiency. Also, they are capable of carrying big and heavy payloads without significantly affecting the duration of the flight.

The six *DoF* of a fixed-wing UAV are controlled using elevators, ailerons and rudders, which are control surfaces built in the wing. The use of the control surfaces allows rotations to be made about any of the three perpendicular axes that intersect at the UAV center of gravity (*CoG*), and therefore control the rotational *DoF*. The translational *DoF* are directly affected by the rotations that the UAV suffers and its forward airspeed, and therefore can be indirectly controlled using the aforementioned control surfaces.

---

<sup>1</sup>Fixed-wing UAV image taken from <https://goo.gl/LNEriU>

### 1.1.2 Rotary-Wing UAVs

Rotary-wing UAVs consist of one or multiple propellers attached to an airframe, generating an air flow and therefore generating the necessary thrust to move while overcoming the gravitational force. These UAVs are capable of doing a vertical take-off and landing (VTOL), so it is not necessary to use a catapult or runway for it. The number of rotors in the UAV determines the classification to which they belong, which usually includes: helicopter (one rotor), trirotor (three rotors), quadrotor (four rotors), hexarotor (six rotors), and octarotors (eight rotors), as the one shown in Fig. 1.2.



Figure 1.2: Altavian Octorotor Rotary-wing UAV<sup>2</sup>

The main advantage of the rotary-wing UAVs is that they do not need to be constantly moving forward in order to have enough lift that sustains the aircraft in flight, as their propellers rotation generates the lift force by itself. This makes the UAV capable of sustaining itself in a desired position.

Rotary-wing UAVs do not have control surfaces that change the direction of the air flow in order to control its six *DoF*. Instead, it uses the unbalance of thrust exerted by its motors and propellers to control the rotations of the rigid body and indirectly control its horizontal translational movement. As the motors' thrust is always pushing the airframe vertically, the vertical translational movement is independently controlled by the total thrust exerted by all the UAVs' motors.

Due to the simplicity in its construction, the most common small-size rotary-wing UAV type developed by manufacturers and hobbyists, is the quadrotor. The quadrotors, also known as quadcopters, are typically based on a light airframe built with fiberglass or carbon fiber, and four motors that serve as actuation devices, as shown in Fig. 1.3. These aircrafts can be built in a relatively simple and inexpensive manner,

---

<sup>2</sup>Rotary-wing UAV image taken from <https://goo.gl/WPVYAg>

besides being easy to control and model, when being compared with other multi-rotors. This is the reason why a quadrotor was established as the experimental platform in this project.



Figure 1.3: Quadrotor aircraft X650 <sup>3</sup>

## 1.2 Literature Review

### 1.2.1 Control Strategies and State Estimation in Quadrotors

Since UAVs represent a challenge for the modelling and design of controllers, from basic to advanced, these aircrafts are widely used in the teaching and research of control systems theory. For instance, [7] implemented a PID controller (with two tuning methods) and a Linear-Quadratic regulator (LQR) for altitude control in a quadrotor, comparing them and establishing the advantages of using a PID controller tuned using the LQR equations. Moreover, [8] exposes the develop of a low cost quadrotor attitude controller based on a PID control strategy with saturation constraints, achieving the quadrotor attitude stabilization with set-points of less than  $0.23 \text{ rad}$ . Another comparison between PID and LQR control strategies is done in [9]. In this case, both controllers are used for trajectory tracking in a Qball-X4 quadcopter, getting smoother results with the LQR implementation.

In [10], a quaternion-based LQR gain scheduling controller is designed and simulated, successfully achieving six *DoF* control of the quadrotor. A position and

---

<sup>3</sup>Quadrotor XAircraft X650 image taken from <https://goo.gl/ug5FJs>

heading regulation system using a LQR is also presented in [11]. Here, the implementation of the designed controller is carried out, in which the elevation regulation with oscillations of  $0.1\text{ m}$  is observed. On the other hand, [12] designed a feed-forwarding LQR, which achieve to control quadrotor attitude with errors of less than  $0.08\text{ rad}$ .

A trajectory tracking controller based on a LQR and an Extended Kalman Filter (EKF) is shown in [13]. This approach use the non-linear quadrotor dynamics model to estimate the quadrotor states and calculte the control signals based on the estimations.

Another quadrotor control strategy found in literature is the Model Predictive Control (MPC). In [14], a MPC controller for trajectory tracking is compared to a PID controller, getting an improvement in setting time and overshoot. [15] proposed a non-linear quaternion based control law complemented with an active disturbance rejection strategy that attempts to control the attitude of a quadrotor.

In [16], a Linear Parameter-Varying (LPV) control strategy is developed. Here, an adaptive control is implemented in order to control independently a family of multi-sized quadrotors using the same controller approach. On the other hand, [17] proposes a fuzzy adaptive sliding mode controller that aims to overcome actuators fault within the quadrotor attitude control system. Another adaptive control strategy was developed in [18], [19] and [20], where parameters uncertainties were taken into account in order to control variable payload quadrotors.

Finally, in [21] and [22], the authors designed  $H_\infty$  controllers for reference tracking in quadrotors, evidencing the advantages of the implementation of this controller in terms of robustness.

Regarding about state estimation in quadrotors, after carrying out the literary review, it was found that the Kalman filter (KF) is a widely used estimation algorithm in all its different variants. For instance, in [23], a KF for altitude estimation based on the model of a moving particle was developed. A two stage KF for both quadrotor state and parameter estimation is presented in [24]. This KF is designed in order to detect and identify faults in the quadrotor actuators. As the quadrotor dynamic model is strictly non-linear, the EKF is a popular variation of the KF used in multiple ongoing research, such as [25], [26], and [27]. Other variation of the KF is the Unscented Kalman Filter (UKF) which uses a deterministic sampling approach in order to estimate the state of a non-linear model. In [28], an UKF is used to estimate the orientation of a quadrotor on a test bench, comparing its estimations with the measurements of an incremental encoder and the estimations of a standard KF. The results of this comparison show that the UKF estimations are more similar to the measured orientation, than the estimates of KF.

In [29] a model-free technique implemented within a Thau observer is presented. This state estimator aims to compensate uncertainties and unmodeled dynamics. Also, other projects have used on-board cameras, for the acquisition of extra data that improve the state estimation, as seen in [30], [31] and [32], demonstrating that the use of vision-based odometry improves the quadrotor state estimation despite depending on inaccurate sensors.

### 1.2.2 Quadrotor Flight Modes

In quadrotors, the on-board flight controllers keep some of the quadrotors *DoF* in a desired value autonomously in order to allow pilots to perform tasks during a flight. These controllers have different modes that can control from three to six *DoF* depending on the will of the pilot. Flight modes commonly found in commercial flight controllers may be as basic to only control its attitude or as complex to let the quadrotor follow a complex trajectory with multiple waypoints [33].

The main flight modes, widely used in commercial flight controllers, are described below according to the number of controlled *DoF*, in ascending order.

- **Stabilize Mode**

This mode allows the pilot to fly the quadrotor manually while the flight controller self-levels the quadrotor attitude and regulates its current heading. Thus, the stabilize mode attempts to control three *DoF* of the quadrotor.

The attitude references can be set or changed by the pilot using the remote control, but their default value is  $0 \text{ rad}$ . On the other hand, the quadrotor heading is simply set to be regulated in its current state, enabling its rate using the remote control.

As the stabilize mode does not take into account the control of the quadrotor position, the pilot needs to regularly change the attitude references manually to keep the quadrotor in a desired position, as it is affected by wind disturbances. Also, the pilot needs to regularly adjust the quadrotor thrust, so a desired altitude is maintained.

- **Altitude Hold Mode**

The altitude hold mode adds automatic elevation control to the Stabilize mode. This way, in addition to controlling the attitude, the quadrotor thrust is set by the flight controller in order to maintain the quadrotor in a desired altitude,

getting four controlled *DoF*.

In this mode, the pilot can remotely control the rate of change of the elevation (with a default value of 0  $m/s$ ), as well as the attitude references.

- **GNSS-Dependent Flight Modes**

The Global Navigation Satellite System (GNSS)-Dependent flight modes, are those that automatically attempt to regulate the six *DoF* of the quadrotor in order to maintain a desired position, heading and altitude during a flight. The main GNSS-Dependent Flight Modes are: Loiter mode, Auto Mode, and Return-To-Launch (RTL) Mode.

In Loiter mode, the quadrotor attitude is self-leveled, while the position and altitude reference can be modified by the pilot using the remote controller. The position and altitude references are initialized using the current quadrotor position and altitude when this mode is set.

The Auto mode attempts to make a quadrotor follow automatically a pre-programmed path connecting multiple position and heading waypoints. This mode use the same controller as the Loiter mode, but its references are set automatically following a waypoints list.

During a flight mission, the home location is set as the position and altitude where the quadrotor took off. The RTL mode is used in case of emergency or when a the last waypoint is reached within a flight mission. This mode is equivalent to the Auto mode, but only has two waypoints. The first waypoint consists in the position of the home location with a previously set security altitude (*RTL* altitude) greater than the take-off altitude. When this waypoint is reached, the home location is set as the following waypoint so the quadrotor starts its landing, while keeping the position controlled.

### 1.2.3 Smartphones in Control Systems

Current smartphone processors are able to perform complex calculations such as those required in the implementation of real time control strategies. Multiple research projects have been carried out using smartphones as tools for development of control systems in robotics.

A survey about the trend of using smartphones as main processing component in robotics for research and education was carried out in [34]. In [35], it is proposed a low cost differential robot controlled using a smartphone as processing and sensing device, taking advantage of the ROS framework for Android. [36] expose the

development of an adaptive cruise control algorithm for an object-following robot controlled by a smartphone on board. Also, an autonomous smartphone-based robot platform for football competitions, exposed in Fig. 1.4, was designed and shown in [37].



Figure 1.4: Smartphone-based ball tracking robot <sup>4</sup>

There are many ongoing research related to the possibility of using smartphones to implement control strategies, such as [38], as configuration and monitoring interfaces in control systems as seen in [39, 40, 41], and as a tool in both education and design of control strategies seen in [42, 43]. Following this trend, in the Universidad del Valle, it was developed a smartphone-based platform for monitoring, control and communication in portable laboratories, where a controller for a pendulum, based in the Lego Mindstorms EV3 platform, was implemented [44].

#### 1.2.4 Smartphone-based Quadrotors

Multiple attempts to unite the technologies of quadrotors and smartphones have been made. Some of this attempts are described below.

In [45], the possibility of using old discarded smartphones as sensors and processor in a quadrotor was studied. In [46], a smartphone was used as mission planner for a quadrotor using a commercial flight controller on board. [47] implemented a flight control system in a smartphone, using its sensors and computational power to stabilize the quadrotor attitude and control its altitude. Also, in the University

---

<sup>4</sup>Smartphone-based ball tracking robot image taken from [37]

of Pennsylvania [48], a Google Tango smartphone was used as a quadrotor flight controller, including an image-based positioning system based on RGB-D images captures. The state estimation algorithms, control and planning were firstly implemented in a ODROID-XU board with additional sensors, but then, in [49], this algorithms were ported to the processor of the updated smartphone used in the project. The quadrotor developed in this project is shown in Fig. 1.5.



Figure 1.5: UPenn’s smartphone-based quadrotor <sup>5</sup>

In [50], a PID controller aimed to be executed in a smartphone on board a quadrotor, which is also responsible for estimating the rotational dynamics of the quadrotor using the measurements made by the smartphone, was implemented. Following this project, [51] exposes in detail the development of a model-free PID controller for a smartphone-based quadrotor, including the processing of delayed feedback in the controller. After that, in [52], a Linear-Quadratic-Integral (LQI) controller was implemented and compared with the model-free PID controller set before. Finally, [53] developed a non-linear complementary filter for position and attitude estimation in a smartphone-based quadrotor.

### Smartphone-based Quadrotor Limitations

The idea of using a smartphone as flight controller in an UAV opens the possibility of a quick and inexpensive development [53]. A smartphone offers other advantages compared with off-the-shelf flight controllers, for instance its powerful quad, hexa or octa-core processors and communications interfaces. However, smartphones and the Android operating system have some limitations that set challenges when implementing a control system in it.

---

<sup>5</sup>UPenn smartphone-based quadrotor image taken from [49]

Android is not a real-time operating system and therefore, can not assure execution of algorithms, like estimation and control, with a constant sample time. Furthermore, the sensors embedded in commercial smartphones are made for applications that do not have high requirements of accuracy nor precision, and therefore may not be appropriate for sensing quadrotor dynamics. Nonetheless, as explained by [54], due to its computing capabilities, smartphones can overcome this limitations while using a temporized thread to execute the control system algorithms and implementing a sensor fusion technique to improve the states estimation reliability. This thread must be executed with a lower sample time compared to the one of the sensors embedded in the smartphone. This will ensure that the execution is not delayed by the sensors acquisition process.

## 1.3 Motivation

Quadrotor control is a difficult and interesting problem. As established by [55] and [56], quadrotor dynamics are affected by nonlinearity, parameters perturbations, uncertainties and disturbances: this include unknown and variable payloads, aerodynamical parameters of the system, wind changes, and sensors inaccuracies. Numerous studies have been developed in designing optimal and robust controllers that allow UAVs to fly and accomplish missions rejecting disturbances and being robust to parameter uncertainties as seen in [57, 58, 59, 60].

Although there are embedded systems with high computational capacity that can serve as controllers of a quadrotor, smartphones are available, easily accessible for people and also have a large computational capacity, hence multiple instrumentation and communication elements integrated in the same device. In the last years, computing capacity and sensor technology in smartphones have decreased in price but increased in performance. Smartphones have become an inexpensive tool capable of commanding an UAV. The challenge then, is to use smartphones as quadrotor flight controllers for autonomous flights following specific missions, taking advantage of the fact that the phones today are very powerful computers that include elements of sensing, processing and signal communication.

This research project aims to design and implement algorithms that will be executed in a smartphone to estimate and control the dynamics of a quadrotor. This project confronts several challenges such as using a smartphone as a hardware development platform, trying to use a non real-time operating system for real-time applications, designing optimal and high order controllers using Java, and executing that controllers in a smartphone.

## 1.4 Research Problem

The existing research challenges include how to develop and implement efficient control algorithms for smartphones using the Android operating system, and assess, adapt and develop the appropriate communication, sensing and performance technologies with smartphones in the execution of missions using quadrotors.

Then, the question to be answered is: how to develop control strategies in a smartphone in order to control the flight dynamics of a quadrotor so it can develop flight missions while the instrumentation and computing capacity of the smartphone is used?

## 1.5 Objectives

In order to find a solution for the research problem, the following general and specific objectives are proposed:

### General Objective

Design and implement algorithms for control and estimation of flight dynamics executed in a smartphone for the quadrotor of the Industrial Control Research Group.

### Specific Objectives

1. Conduct a study and analysis of the state of the art related to the control and estimation of states of quadrotors.
2. Integrate the existing quadrotor with a smartphone that contains the appropriate sensors for the control and estimation of states.
3. Obtain a dynamic model of the quadrotor.
4. Design and implement the algorithms for control and estimation of states for the quadrotor.
5. Integrate the experimentation platform with the control and estimation algorithms in the smartphone.
6. Evaluate the performance of the control strategies.

## 1.6 Outline

This thesis is organized as follows.

In Chapter 1, the definition and classification of UAVs are given. After that, a short literature review regarding control and estimation in quadrotors, flight modes, and smartphones in control systems, is detailed. Finally, the motivation and scope of this project are presented.

The dynamic model of the quadrotor is described in Chapter 2. Here, the non-linear and linearized quadrotor model are obtained taking into account the main quadrotor geometry configurations and their inputs setting.

Chapter 3 focuses on the smartphone-based quadrotor prototype description, detailing all its components and their interactions, as well as the specific parameters of the prototype.

The control and estimation algorithms design is presented in Chapter 4. In this chapter, specific controllers for each quadrotor flight mode are designed and simulated.

In Chapter 5, the results of the implementation of the control and estimation algorithms, as well as the description of the Android application and the GCS are detailed.

Finally, in Chapter 6, the thesis conclusions and suggestions for future developments and improvements, are shown.

# Chapter 2

## Dynamic Model of the Quadrotor

In this chapter, the dynamics of the quadrotor and the calculation of the mathematical model through two different approaches, are provided. In addition, the necessary considerations for the choice of a geometry configuration are exposed. This dynamic model and its inputs setting are needed to design the quadrotor flight controllers.

Section 2.1 presents the description of two of the main used quadrotor geometry configurations. Also, this section presents what it means to choose one or the other configuration for the setting of the quadrotor inputs.

The dynamic model of the quadrotor, obtained using the Newton-Euler and Euler-Lagrange approaches, neglecting the gyroscopic effects produced by the propellers, is shown in Section 2.2.

Finally, Section 2.3 describes an overview of the Jacobian linearization method applied to the quadrotor dynamic model and the thrust compensation needed to be implemented in a real quadrotor.

### 2.1 Quadrotors Configurations

The term ‘quadrotor’ refers to a rotary-wing UAV which thrust is generated using four motors and propellers. Quadrotors can be build in multiple ways. There are two basic configurations which are widely used by commercial manufacturers and hobbyists. These two configurations are the ‘+’ and the ‘X’.

### 2.1.1 The ‘+’ Configuration

The geometry used in quadrotors built in ‘+’ configuration is shown in Fig. 2.1.

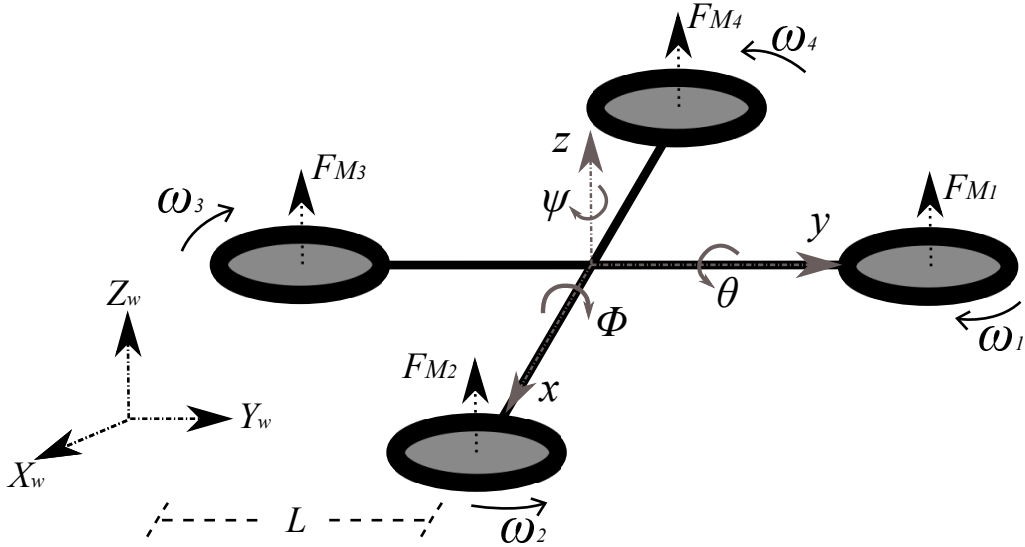


Figure 2.1: Quadrotor geometry in ‘+’ configuration

In Fig. 2.1,  $(\phi, \theta, \psi)$  are the angular deviations (pitch, roll and yaw, respectively) of the quadrotor about the body-frame;  $(x, y, z)$  are the body-frame axes;  $(X_w, Y_w, Z_w)$  are the earth-frame axes;  $L$  is the distance from the quadrotor center of gravity (*CoG*) to the motors center;  $F_{M_i}$  is the thrust force exerted by each motor  $M_i$ ; and  $\omega_i$  is the angular velocity of  $M_i$ , with  $i = 1, 2, 3, 4$ . In this configuration, the body-frame axes  $x$  and  $y$ , coincide with the lines that connect motors of opposite sides in the quadrotor frame.

The quadrotor is a system with six *DoF*. Since a quadrotor has four actuators, it can be considered an underactuated system. This means that, it is only possible to reach a desired state for four *DoF*. However, it is possible to indirectly control the two remaining *DoF* choosing the control signals appropriately. These control signals, or inputs, represent the quadrotor basic movements and are described below.

- **Thrust  $T_u$  [N]**

The thrust  $T_u$  is the total thrust force exerted parallel to the body-frame  $z$ -axis by the four motors. This thrust, can also generate accelerations in the direction of the  $X_w$  and  $Y_w$  axes. This happens when  $|\theta| > 0$  or  $|\phi| > 0$ .

This control signal affects the speed of rotation of all motors, and therefore their thrust, in equal magnitude, and is set as

$$T_u = \sum_{i=1}^4 F_{M_i}. \quad (2.1)$$

- **Yaw Torque  $\tau_\psi$  [N · m]**

From Fig. 2.1,  $M_1$  and  $M_3$  have a clockwise (CW) rotation while  $M_2$  and  $M_4$  rotate counter-clockwise (CCW). This configuration of opposite pairs rotational directions allows the system to control its conservation of momentum, and thus change its yaw angle in a controlled manner. This is done unbalancing the total momentum around the  $z$ -axis and without the need of a tail rotor used in the standard helicopter structure ([61]). In ‘+’ configuration, the fact that the pitch and roll angles are controlled using only two motors that rotate in the same direction, leads to large changes in the thrust force of the other two motors to achieve conservation of momentum.

This conservation of momentum is controlled using the torque generated by each motor ( $\tau_{M_i}$ ) around the body-frame  $z$ -axis. It produces a turn in the opposite direction to the rotation of the motor. Taking into account that the torque  $\tau_\psi$  is positive when it generates a clock-wise rotation around the  $z$ -axis, only  $M_2$  and  $M_4$  contribute positively to it. While the other tow motors have a negative contribution to  $\tau_\psi$ . Thus, the total torque around the  $z$ -axis is depicted as

$$\tau_\psi = \tau_{M_2} + \tau_{M_4} - \tau_{M_1} - \tau_{M_3}. \quad (2.2)$$

Each torque  $\tau_{M_i}$  has a linear relationship with the thrust applied by the motor, with  $K_M$  being the proportional constant and

$$\tau_{M_i} = K_M F_{M_i}. \quad (2.3)$$

Replacing (2.3) in (2.2) the total torque  $\tau_\psi$  dependence on the forces  $F_{M_i}$  is got as

$$\tau_\psi = K_m (F_{M_2} + F_{M_4} - F_{M_1} - F_{M_3}). \quad (2.4)$$

- **Roll Torque  $\tau_\theta$  [N · m]**

The roll torque  $\tau_\theta$  is described as the torque exerted on the  $x$ -axis and about the  $y$ -axis. In the ‘+’ configuration, the only motors that affect the quadrotor rotation with respect to the  $x$ -axis are  $M_2$  and  $M_4$ . These do not affect the rotation with respect to the  $y$ -axis. In this case, the torques are generated by the forces  $F_{M_2}$  and  $F_{M_4}$  being applied at a distance  $L$  from the quadrotor *CoG*. Considering a positive  $\tau_\theta$  as the one causing a counter clock-wise rotation about the  $y$ -axis, the roll torque in ‘+’ is set as

$$\tau_\theta = L(F_{M_4} - F_{M_2}). \quad (2.5)$$

- **Pitch Torque**  $\tau_\phi$  [ $N \cdot m$ ]

Unlike the roll torque, the pitch torque  $\tau_\phi$  is the one exerted on the  $y$ -axis about the  $x$ -axis. As Fig. 2.1 shows,  $M_1$  and  $M_3$  are the motors applying the forces that create this torque. Being  $\tau_\phi$  positive when clock-wise rotation about the  $x$ -axis is caused, it is defined for a ‘+’ configuration as

$$\tau_\phi = L(F_{M_3} - F_{M_1}). \quad (2.6)$$

### Inputs Setting in ‘+’ Configuration

Summarizing, the ‘+’ configuration quadrotor inputs are established as linear combinations of the motors forces  $F_{M_i}$ . Equations (2.1), (2.4), (2.5) and (2.6) integrate a linear equations system where the vector of inputs  $\mathbf{u}_{(+)}$  is

$$\mathbf{u}_{(+)} = \begin{bmatrix} T_u \\ \tau_\psi \\ \tau_\theta \\ \tau_\phi \end{bmatrix} = \begin{bmatrix} 1 & 1 & 1 & 1 \\ -K_m & K_m & -K_m & K_m \\ 0 & -L & 0 & L \\ -L & 0 & L & 0 \end{bmatrix} \begin{bmatrix} F_{M_1} \\ F_{M_2} \\ F_{M_3} \\ F_{M_4} \end{bmatrix}. \quad (2.7)$$

### 2.1.2 The ‘X’ Configuration

Following the same nomenclature used in the ‘+’ configuration, in ‘X’ configuration, the quadrotor frame is rotated  $\pi/4$  rad about the  $z$ -axis in the body-frame, as shown in Fig. 2.2.

In this case, the front-line in the quadrotor is set between  $M_1$  and  $M_4$ . In ‘X’ configuration, the roll and pitch torques are applied using the forces exerted by all the motors at a distance  $L_X = L \cdot \cos(\pi/4)$  ([62]). This geometry is shown in Fig. 2.2.

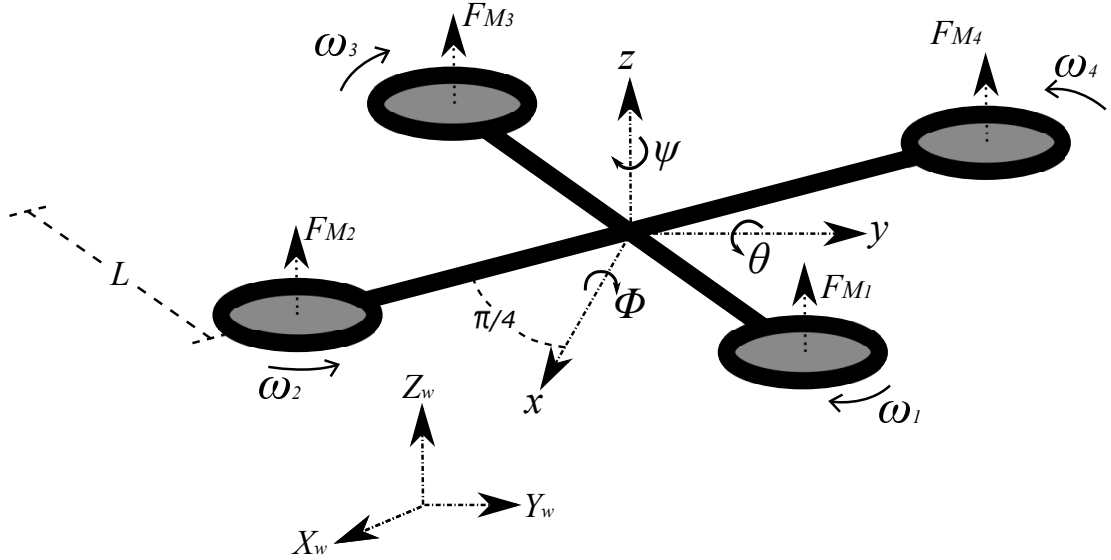


Figure 2.2: Quadrotor geometry in ‘X’ configuration

The inputs description for the quadrotor ‘X’ configuration is defined as follows.

- **Thrust**  $T_u$  [N]

The total thrust exerted by the four motors in the quadrotor is not changed between the ‘+’ and ‘X’ configurations. Hence, the thrust  $T_u$  is defined as

$$T_u = \sum_{i=1}^4 F_{M_i}. \quad (2.8)$$

- **Yaw Torque**  $\tau_\psi$  [ $N \cdot m$ ]

As the  $z$ -axis is not modified between the ‘+’ and ‘X’ configurations, and the motors rotate in the same direction as in the other configuration, the yaw torque  $\tau_\psi$  is set as

$$\tau_\psi = K_m(F_{M_2} + F_{M_4} - F_{M_1} - F_{M_3}). \quad (2.9)$$

- **Roll Torque**  $\tau_\theta$  [ $N \cdot m$ ]

As shown in Fig. 2.2, roll and pitch torques are affected by the effects of

all the quadrotor motors. For the roll torque  $\tau_\theta$ , the motors  $M_3$  and  $M_4$  contribute positively, while  $M_1$  and  $M_2$  have a negative contribution to it. In this case, the roll torque is depicted as

$$\tau_\theta = L_X(F_{M_3} + F_{M_4} - F_{M_2} - F_{M_1}). \quad (2.10)$$

- **Pitch Torque  $\tau_\phi$  [N · m]**

Due to the *CW* positive direction of the  $\phi$  angle, and considering the sign of the contribution exerted by each force  $F_{M_i}$ , the pitch torque for the ‘X’ configuration is defined as

$$\tau_\phi = L_X(F_{M_2} + F_{M_3} - F_{M_1} - F_{M_4}). \quad (2.11)$$

### Inputs Setting in ‘X’ Configuration

In the ‘X’ configuration, the quadrotor inputs remain the same regarding the ‘+’ configuration. However both  $\tau_\theta$  and  $\tau_\phi$  are affected by the interaction of all the motors and the change in the distance of the point of application of the forces  $F_{M_i}$  on the  $x$  and  $y$  axes. The linear equations system that shows the inputs setting for a quadrotor in ‘X’ configuration is defined as

$$\mathbf{u}_{(X)} = \begin{bmatrix} T_u \\ \tau_\psi \\ \tau_\theta \\ \tau_\phi \end{bmatrix} = \begin{bmatrix} 1 & 1 & 1 & 1 \\ -K_m & K_m & -K_m & K_m \\ -L_X & -L_X & L_X & L_X \\ -L_X & L_X & L_X & -L_X \end{bmatrix} \begin{bmatrix} F_{M_1} \\ F_{M_2} \\ F_{M_3} \\ F_{M_4} \end{bmatrix}. \quad (2.12)$$

### Maximum Torque About $x$ and $y$ axes in ‘X’ Configuration

In ‘+’ configuration, the torques around the  $x$  and  $y$  axes are set using just two motors applying a force at a distance  $L$  from the quadrotor *CoG*. This implies that, for instance, in the case of roll torque  $\tau_\theta$  the maximum torque  $\tau_{\theta max(+)}$  is achieved when  $F_{M_4} = F_{M_{i max}}$  and  $F_{M_3} = 0$ , where  $F_{M_{i max}}$  is the maximum thrust of the motors. Then, in ‘+’ configuration, the  $\tau_{\theta max(+)}$  is set as

$$\tau_{\theta max(+)} = L \cdot F_{M_{i max}} \quad (2.13)$$

On the other hand, the torques around the  $x$  and  $y$  axes in ‘X’ configuration depend on the forces of the four motors in the quadrotor, which are applied at a distance  $L_X = L \cdot \cos(\pi/4)$  from the quadrotor *CoG*. Continuing with the example of the roll torque, in ‘X’ configuration the maximum torque  $\tau_{\theta max(X)}$  is achieved when

$F_{M_3} = F_{M_4} = F_{M_{i\max}}$  and  $F_{M_1} = F_{M_2} = 0$ . Hence, the maximum torque about the  $y$ -axis in ‘X’ configuration is

$$\begin{aligned}\tau_{\theta\max(X)} &= L \cdot \cos(\pi/4) \cdot 2 \cdot F_{M_{i\max}} \\ \tau_{\theta\max(X)} &= 2 \cdot \cos(\pi/4) \cdot \tau_{\theta\max(+)}\end{aligned}\quad (2.14)$$

Thereby, the quadrotor in ‘X’ configuration has  $2 \cdot \cos(\pi/4)$  times more available torque to rotate about the  $x$  and  $y$  axes, when compared with the ‘+’ configuration, and therefore it can achieve 41.42 % more rotational acceleration about the  $x$  and  $y$  axes.

## 2.2 Non-linear Model

This section describes the dynamic modeling used to develop the quadrotor control, based on the study carried out in [61] and [1]. This model represents the quadrotor as a solid symmetrical object, subject to a total thrust ( $T_u$ ) and three torques ( $\tau_\psi$ ,  $\tau_\theta$  and  $\tau_\phi$ ), assuming that the quadrotor *CoG* coincides with the origin of the body-frame and without considering the dynamics of the actuators. The modeling of the quadrotor system is done by two different methods. The Newton-Euler approach is based on the quadrotor body-frame, while the Euler-Lagrange approach bases its translational equations in the earth-frame while keeping its rotational equations related to the body-frame.

### 2.2.1 Newton-Euler Approach

Following the quadrotor geometry shown in Fig. 2.2, the quadrotor position vector ( $\Xi$ ), composed by the translational position ( $\Gamma_W$  [m]) and rotational position ( $\Theta_W$  [rad]) regarding the earth-frame, is defined as

$$\Xi = \begin{bmatrix} \Gamma_W \\ \Theta_W \end{bmatrix} = \begin{bmatrix} X_W \\ Y_W \\ Z_W \\ \psi \\ \theta \\ \phi \end{bmatrix}. \quad (2.15)$$

On the other hand, the quadrotor velocity vector ( $\nu$ ) is composed by the translational ( $\mathbf{V}_B$  [ $m \cdot s^{-1}$ ]) and rotational ( $\Omega_B$  [ $rad \cdot s^{-1}$ ]) velocities with respect to the body-frame

as

$$\nu = \begin{bmatrix} \mathbf{V}_B \\ \boldsymbol{\Omega}_B \end{bmatrix} = \begin{bmatrix} \dot{x} \\ \dot{y} \\ \dot{z} \\ \dot{\psi} \\ \dot{\theta} \\ \dot{\phi} \end{bmatrix}. \quad (2.16)$$

Therefore exists a generalized matrix

$$\zeta_{\Theta} = \begin{bmatrix} \mathbf{R}_b^w & \mathbf{0}_{3 \times 3} \\ \mathbf{0}_{3 \times 3} & \mathbf{T}_b^w \end{bmatrix}, \quad (2.17)$$

that ensures that

$$\dot{\Xi} = \zeta_{\Theta} \nu, \quad (2.18)$$

where  $\mathbf{0}_{3 \times 3}$  is a  $3 \times 3$ -matrix filled with zeros,  $\mathbf{R}_b^w$  is the rotation matrix and  $\mathbf{T}_b^w$  the transfer matrix from the body to the world-frame, defined as

$$\mathbf{R}_b^w = \begin{bmatrix} c_\theta c_\psi & c_\psi s_\theta s_\phi - c_\phi s_\psi & s_\phi s_\psi + c_\phi c_\psi s_\theta \\ c_\theta s_\psi & s_\psi s_\theta s_\phi + c_\phi c_\psi & c_\phi s_\psi s_\theta - s_\phi c_\psi \\ -s_\theta & c_\theta s_\phi & c_\theta c_\phi \end{bmatrix}, \quad (2.19)$$

$$\mathbf{T}_b^w = \begin{bmatrix} 1 & s_\phi t_\theta & c_\phi t_\theta \\ 0 & c_\phi & -s_\phi \\ 0 & s_\phi/c_\theta & c_\phi/c_\theta \end{bmatrix}, \quad (2.20)$$

with  $s_\theta = \sin(\theta)$ ,  $c_\theta = \cos(\theta)$ , and  $t_\theta = \tan(\theta)$ .

As the quadrotor is assumed to be a rigid body of 6 *DoF*, its dynamics consider the mass ( $m$  [ $kg$ ]) and the inertia matrix ( $\mathbf{J}$  [ $kg \cdot m^2$ ]) of it, and are described as

$$\mathbf{M}_B \ddot{\nu} + \mathbf{S}_\nu = \boldsymbol{\Lambda} \quad (2.21)$$

where

$$\mathbf{M}_B = \begin{bmatrix} m\mathbf{I}_{3 \times 3} & \mathbf{0}_{3 \times 3} \\ \mathbf{0}_{3 \times 3} & \mathbf{J} \end{bmatrix} = \begin{bmatrix} m & 0 & 0 & 0 & 0 & 0 \\ 0 & m & 0 & 0 & 0 & 0 \\ 0 & 0 & m & 0 & 0 & 0 \\ 0 & 0 & 0 & J_{zz} & 0 & 0 \\ 0 & 0 & 0 & 0 & J_{yy} & 0 \\ 0 & 0 & 0 & 0 & 0 & J_{xx} \end{bmatrix},$$

$$\dot{\nu} = \begin{bmatrix} \dot{\mathbf{V}}_B \\ \dot{\Omega}_B \end{bmatrix}, \quad (2.22)$$

$$\mathbf{S}_\nu = \begin{bmatrix} \Omega_B \times m\mathbf{V}_B \\ \Omega_B \times \mathbf{J}\Omega_B \end{bmatrix} = \begin{bmatrix} m(\ddot{x} + \dot{z}\dot{\theta} - \dot{y}\dot{\phi}) \\ m(\ddot{y} + \dot{x}\dot{\phi} - \dot{z}\dot{\psi}) \\ m(\ddot{z} + \dot{y}\dot{\psi} - \dot{x}\dot{\theta}) \\ J_{zz}\dot{\psi} + \dot{\theta}\dot{\phi}(J_{xx} - J_{yy}) \\ J_{yy}\dot{\theta} + \dot{\psi}\dot{\phi}(J_{zz} - J_{xx}) \\ J_{xx}\dot{\phi} + \dot{\psi}\dot{\theta}(J_{yy} - J_{zz}) \end{bmatrix},$$

$$\Lambda = \begin{bmatrix} \mathbf{F}_B \\ \tau_B \end{bmatrix} = [F_x \ F_y \ F_z \ \tau_z \ \tau_y \ \tau_x]^T,$$

being  $\mathbf{J}$  diagonal due to the assumption of a perfect symmetric quadrotor body,  $\mathbf{I}$  the identity matrix,  $\dot{\mathbf{V}}_B$  is the quadrotor translational acceleration in the body-frame,  $\dot{\Omega}_B$  is the quadrotor angular acceleration in the body-frame,  $\mathbf{F}_B$  is the quadrotor force vector and  $\tau_B$  is the quadrotor torques vector.

The forces and torques vector  $\Lambda$  results from the effect of the gravitational force (represented in  $\mathbf{G}_\Lambda$ ), the quadrotor inputs created by the motor forces (represented in  $\mathbf{U}_\Lambda$ ), and the gyroscopic effects produced when the motors propellers are rotating (represented in  $\mathbf{P}_\Lambda$ ). However in this project, for simplicity in the dynamic model, it is not taken into account the  $\mathbf{P}_\Lambda$  contribution to the  $\Lambda$  vector and thus  $\mathbf{P}_\Lambda \approx \mathbf{0}_{6 \times 1}$ .

The gravitational force affects just the  $\mathbf{F}_B$  component in  $\Lambda$ , proportionally to its magnitude  $|\vec{g}| = g = 9.807 \text{ m/s}^2$ .  $\mathbf{G}_\Lambda$  is the contribution of the gravitational force to the vector  $\Lambda$  and is expressed as

$$\mathbf{G}_\Lambda = \begin{bmatrix} \hat{\mathbf{F}}_{Gb} \\ \mathbf{0}_{3 \times 1} \end{bmatrix} = \begin{bmatrix} \mathbf{R}_b^w \mathbf{F}_{G\xi} \\ \mathbf{0}_{3 \times 1} \end{bmatrix} = \begin{bmatrix} \mathbf{R}_w^b \begin{bmatrix} 0 \\ 0 \\ -mg \end{bmatrix} \\ \mathbf{0}_{3 \times 1} \end{bmatrix} = \begin{bmatrix} mg \sin(\theta) \\ mg \cos(\theta) \sin(\phi) \\ -mg \cos(\theta) \sin(\phi) \\ \mathbf{0}_{3 \times 1} \end{bmatrix} \quad (2.23)$$

were  $\mathbf{F}_{G\xi} = \mathbf{R}_b^w \hat{\mathbf{F}}_{Gb}$  is the translational force due to gravity in the earth-frame, and  $\mathbf{R}_w^b = (\mathbf{R}_b^w)^{-1}$  is the rotation matrix from the world to the body-frame.

From Section 2.1, it follows that the quadrotor inputs are proportional to the motor forces  $F_{M_i}$ , and do not affect the  $x$  and  $y$  components of  $\mathbf{F}_B$ . These inputs, depend on the quadrotor configuration ('+' or 'X') and are set as

$$\mathbf{u}_\Lambda = \begin{bmatrix} 0 \\ 0 \\ u_1 \\ u_2 \\ u_3 \\ u_4 \end{bmatrix} = \begin{bmatrix} 0 \\ 0 \\ T_u \\ \tau_\psi \\ \tau_\theta \\ \tau_\phi \end{bmatrix} \quad (2.24)$$

where  $T_u$ ,  $\tau_\psi$ ,  $\tau_\theta$  and  $\tau_\phi$  depend on the configuration of the quadrotor as exposed in (2.7) and (2.12).

Thus, (2.21) can be redefined as

$$\mathbf{M}_B \dot{\nu} + \mathbf{S}_\nu = \mathbf{G}_\Lambda + \mathbf{u}_\Lambda. \quad (2.25)$$

The quadrotor acceleration vector  $\dot{\nu}$  in the body-frame is then isolated from (2.25), getting

$$\dot{\nu} = \mathbf{M}_B^{-1}(-\mathbf{S}_\nu + \mathbf{G}_\Lambda + \mathbf{u}_\Lambda), \quad (2.26)$$

or expressed as a system of equations

$$\begin{aligned} \ddot{x} &= \dot{y}\dot{\phi} - \dot{z}\dot{\theta} + g \sin(\theta), \\ \ddot{y} &= \dot{z}\dot{\psi} - \dot{x}\dot{\phi} + g \cos(\theta) \sin(\phi), \\ \ddot{z} &= \dot{x}\dot{\theta} - \dot{y}\dot{\psi} - g \sin(\theta) + \frac{u_1}{m}, \\ \ddot{\psi} &= \dot{\phi}\dot{\theta} \frac{J_{xx} - J_{yy}}{J_{zz}} + \frac{u_2}{J_{zz}}, \\ \ddot{\theta} &= \dot{\phi}\dot{\psi} \frac{J_{zz} - J_{xx}}{J_{yy}} + \frac{u_3}{J_{yy}}, \\ \ddot{\phi} &= \dot{\theta}\dot{\psi} \frac{J_{yy} - J_{zz}}{J_{xx}} + \frac{u_4}{J_{xx}}, \end{aligned} \quad (2.27)$$

with the inputs set as

$$\begin{bmatrix} u_1 \\ u_2 \\ u_3 \\ u_4 \end{bmatrix} = \begin{bmatrix} T_u \\ \tau_\psi \\ \tau_\theta \\ \tau_\phi \end{bmatrix} = \begin{bmatrix} 1 & 1 & 1 & 1 \\ -K_m & K_m & -K_m & K_m \\ 0 & -L & 0 & L \\ -L & 0 & L & 0 \end{bmatrix} \begin{bmatrix} F_{M_1} \\ F_{M_2} \\ F_{M_3} \\ F_{M_4} \end{bmatrix} \quad (2.28)$$

for quadrotors in ‘+’ configuration, and

$$\begin{bmatrix} u_1 \\ u_2 \\ u_3 \\ u_4 \end{bmatrix} = \begin{bmatrix} T_u \\ \tau_\psi \\ \tau_\theta \\ \tau_\phi \end{bmatrix} = \begin{bmatrix} 1 & 1 & 1 & 1 \\ -K_m & K_m & -K_m & K_m \\ -L_X & -L_X & L_X & L_X \\ -L_X & L_X & L_X & -L_X \end{bmatrix} \begin{bmatrix} F_{M_1} \\ F_{M_2} \\ F_{M_3} \\ F_{M_4} \end{bmatrix} \quad (2.29)$$

for quadrotors in ‘X’ configuration.

Defining the state vector as

$$\mathbf{x} = [x \ \dot{x} \ y \ \dot{y} \ z \ \dot{z} \ \psi \ \dot{\psi} \ \theta \ \dot{\theta} \ \phi \ \dot{\phi}]^T, \quad (2.30)$$

the quadrotor non-linear dynamics model  $\mathbf{f}(\mathbf{x}, \mathbf{u})$  got with a Newton-Euler approach is

$$\dot{\mathbf{x}} = \mathbf{f}(\mathbf{x}, \mathbf{u}) = \begin{bmatrix} \dot{x} \\ \dot{y}\dot{\phi} - \dot{z}\dot{\theta} + g \sin(\theta) \\ \dot{y} \\ \dot{z}\dot{\psi} - \dot{x}\dot{\phi} + g \cos(\theta) \sin(\phi) \\ \dot{z} \\ \dot{x}\dot{\theta} - \dot{y}\dot{\psi} - g \sin(\theta) + \frac{u_1}{m} \\ \dot{\psi} \\ \dot{\phi}\dot{\theta} \frac{J_{xx} - J_{yy}}{J_{zz}} + \frac{u_2}{J_{zz}} \\ \dot{\theta} \\ \dot{\phi}\dot{\psi} \frac{J_{zz} - J_{xx}}{J_{yy}} + \frac{u_3}{J_{yy}} \\ \dot{\phi} \\ \dot{\theta}\dot{\psi} \frac{J_{yy} - J_{zz}}{J_{xx}} + \frac{u_4}{J_{xx}} \end{bmatrix} \quad (2.31)$$

## 2.2.2 Euler-Lagrange Approach

The general coordinates representing the position and attitude of the quadrotor are defined as

$$\boldsymbol{\Xi} = [\xi_{\mathbf{W}} \ \boldsymbol{\Theta}_{\mathbf{B}}]^T, \quad (2.32)$$

where  $\xi_{\mathbf{W}} = [X_W \ Y_W \ Z_W]^T$  is the vector representing the position of the *CoG* of the quadrotor relative to the earth-frame shown in Fig. 2.2 and  $\boldsymbol{\Theta}_{\mathbf{B}} = [\psi \ \theta \ \phi]^T$  represent the quadrotor attitude.

The Lagrangian of the quadrotor is defined by

$$L(\boldsymbol{\Xi}, \dot{\boldsymbol{\Xi}}) = K_{trans} + K_{rot} - E_{pot}, \quad (2.33)$$

where  $K_{trans}$  is the quadrotor translational kinetic energy,  $K_{rot}$  is the quadrotor rotational kinetic energy,  $E_{pot}$  is the quadrotor potential energy, and  $z$  is the quadrotor elevation. Hence, the Lagrangian in (2.33) is rewritten as

$$L(\boldsymbol{\Xi}, \dot{\boldsymbol{\Xi}}) = \frac{m}{2} \dot{\xi}_{\mathbf{W}}^T \dot{\xi}_{\mathbf{W}} + \frac{1}{2} \dot{\Theta}_{\mathbf{B}}^T J \dot{\Theta}_{\mathbf{B}} - mgz. \quad (2.34)$$

The dynamic model of the quadrotor is derived from the Euler-Lagrange equation

$$\frac{d}{dt} \frac{\partial L}{\partial \dot{\boldsymbol{\Xi}}} - \frac{\partial L}{\partial \boldsymbol{\Xi}} = \begin{bmatrix} F_{\xi} \\ \tau \end{bmatrix}, \quad (2.35)$$

where  $F_{\xi} = R_b^w \hat{F}_b$  is the translational force applied to the quadrotor by its four motors, and  $\tau = [\tau_{\psi} \ \tau_{\theta} \ \tau_{\phi}]^T$ .

In the quadrotor body-frame, the translational force  $\hat{F}_b$  is only applied in the  $z$ -axis, and thus it is represented by

$$\hat{F}_b = \begin{bmatrix} 0 \\ 0 \\ T_u \end{bmatrix} = \begin{bmatrix} 0 \\ 0 \\ \sum_{i=1}^4 F_{M_i} \end{bmatrix}. \quad (2.36)$$

The system of equations that represent the dynamics of the quadrotor got using the Euler-Lagrange approach (2.35) is

$$\begin{aligned} \ddot{X}_W &= \frac{u_1}{m} (\cos(\phi) \sin(\theta) \cos(\psi) + \sin(\phi) \sin(\psi)), \\ \ddot{Y}_W &= \frac{u_1}{m} (\cos(\phi) \sin(\theta) \sin(\psi) - \sin(\phi) \cos(\psi)), \\ \ddot{Z}_W &= \frac{u_1}{m} (\cos(\phi) \cos(\theta)) - g, \\ \ddot{\psi} &= \dot{\phi} \dot{\theta} \frac{J_{xx} - J_{yy}}{J_{zz}} + \frac{u_2}{J_{zz}}, \\ \ddot{\theta} &= \dot{\phi} \dot{\psi} \frac{J_{zz} - J_{xx}}{J_{yy}} + \frac{u_3}{J_{yy}}, \\ \ddot{\phi} &= \dot{\theta} \dot{\psi} \frac{J_{yy} - J_{zz}}{J_{xx}} + \frac{u_4}{J_{xx}}, \end{aligned} \quad (2.37)$$

with the inputs set as

$$\begin{bmatrix} u_1 \\ u_2 \\ u_3 \\ u_4 \end{bmatrix} = \begin{bmatrix} T_u \\ \tau_\psi \\ \tau_\theta \\ \tau_\phi \end{bmatrix} = \begin{bmatrix} 1 & 1 & 1 & 1 \\ -K_m & K_m & -K_m & K_m \\ 0 & -L & 0 & L \\ -L & 0 & L & 0 \end{bmatrix} \begin{bmatrix} F_{M_1} \\ F_{M_2} \\ F_{M_3} \\ F_{M_4} \end{bmatrix} \quad (2.38)$$

for quadrotors in ‘+’ configuration, and

$$\begin{bmatrix} u_1 \\ u_2 \\ u_3 \\ u_4 \end{bmatrix} = \begin{bmatrix} T_u \\ \tau_\psi \\ \tau_\theta \\ \tau_\phi \end{bmatrix} = \begin{bmatrix} 1 & 1 & 1 & 1 \\ -K_m & K_m & -K_m & K_m \\ -L_X & -L_X & L_X & L_X \\ -L_X & L_X & L_X & -L_X \end{bmatrix} \begin{bmatrix} F_{M_1} \\ F_{M_2} \\ F_{M_3} \\ F_{M_4} \end{bmatrix} \quad (2.39)$$

for quadrotors in ‘X’ configuration ([63, 64]).

Defining the state vector as

$$\mathbf{x} = [X_W \ X_W \dot{ } \ Y \ Y_W \dot{ } \ Z_W \ Z_W \dot{ } \ \psi \ \dot{\psi} \ \theta \ \dot{\theta} \ \phi \ \dot{\phi}]^T, \quad (2.40)$$

the quadrotor non-linear dynamics model got with an Euler-Lagrange approach, can be represented as

$$\dot{\mathbf{x}} = \mathbf{f}(\mathbf{x}, \mathbf{u}) = \begin{bmatrix} \dot{X}_W \\ \frac{u_1}{m}(\cos(\phi) \sin(\theta) \cos(\psi) + \sin(\phi) \sin(\psi)) \\ \dot{Y}_W \\ \frac{u_1}{m}(\cos(\phi) \sin(\theta) \sin(\psi) - \sin(\phi) \cos(\psi)) \\ \dot{Z}_W \\ \frac{u_1}{m}(\cos(\phi) \cos(\theta)) - g \\ \dot{\psi} \\ \dot{\phi} \dot{\theta} \frac{J_{xx} - J_{yy}}{J_{zz}} + \frac{u_2}{J_{zz}} \\ \dot{\phi} \dot{\psi} \frac{J_{zz} - J_{xx}}{J_{yy}} + \frac{u_3}{J_{yy}} \\ \dot{\theta} \dot{\psi} \frac{J_{yy} - J_{zz}}{J_{xx}} + \frac{u_4}{J_{xx}} \end{bmatrix} \quad (2.41)$$

## 2.3 Linearized Model

### 2.3.1 Jacobian Linearization

The linearization of a non-linear system is done about an equilibrium point  $\bar{\mathbf{x}}$  achieved with a specific input called equilibrium input  $\bar{\mathbf{u}}$  where  $\mathbf{f}(\bar{\mathbf{x}}, \bar{\mathbf{u}}) \approx \mathbf{0}$ . In the quadrotor, such an equilibrium point can be the hover state where  $\Omega_{\mathbf{B}} \rightarrow \mathbf{0}_{3 \times 1}$ ,  $\dot{\Omega}_{\mathbf{B}} \rightarrow \mathbf{0}_{3 \times 1}$ , and  $\mathbf{V}_{\mathbf{B}} \rightarrow \mathbf{0}_{3 \times 1}$ . This is

$$\begin{aligned}\bar{\mathbf{x}} &= [\bar{x} \ \dot{\bar{x}} \ \bar{y} \ \dot{\bar{y}} \ \bar{z} \ \dot{\bar{z}} \ \bar{\psi} \ \dot{\bar{\psi}} \ \bar{\theta} \ \dot{\bar{\theta}} \ \bar{\phi} \ \dot{\bar{\phi}}]^T \\ &= [\bar{x} \ 0 \ \bar{y} \ 0 \ \bar{z} \ 0 \ 0 \ 0 \ 0 \ 0 \ 0 \ 0]^T,\end{aligned}\quad (2.42)$$

where  $\bar{x}$ ,  $\bar{y}$  and  $\bar{z}$  define a constant desired position in the body and earth-frame. When the quadrotor state is near the equilibrium point, the body and earth frames are assumed to coincide and thus  $\dot{\xi}_{\mathbf{W}} \rightarrow \mathbf{V}_{\mathbf{B}}$ ,  $X_W \rightarrow x$ ,  $Y_W \rightarrow y$ , and  $Z_W \rightarrow z$  ([65]).

The equilibrium point shown in 2.42, is obtained using a constant input value  $\bar{\mathbf{u}}$  where only the thrust that overcomes gravity is applied, as shown below.

$$\bar{\mathbf{u}} = [T_u \ \tau_{\psi} \ \tau_{\theta} \ \tau_{\phi}]^T = [mg \ 0 \ 0 \ 0]^T \quad (2.43)$$

The Jacobian linearization is based on the fact that if the quadrotor is not exactly at the equilibrium point, but close to it with a small deviation  $\delta_{\mathbf{x}} = \mathbf{x} - \bar{\mathbf{x}}$ , due to an input deviation  $\delta_{\mathbf{u}} = \mathbf{u} - \bar{\mathbf{u}}$  [66]. The non-linear system is represented by

$$\dot{\delta}_{\mathbf{x}} = \mathbf{f}(\bar{\mathbf{x}} + \delta_{\mathbf{x}}, \bar{\mathbf{u}} + \delta_{\mathbf{u}}). \quad (2.44)$$

Using the first order Taylor polynomial from (2.44) and considering that  $\mathbf{f}(\bar{\mathbf{x}}, \bar{\mathbf{u}}) \approx \mathbf{0}$ , the following expression is obtained.

$$\dot{\delta}_{\mathbf{x}} \approx \frac{\partial f(\mathbf{x}, \mathbf{u})}{\partial \mathbf{x}} \Big|_{\substack{\mathbf{x}=\bar{\mathbf{x}} \\ \mathbf{u}=\bar{\mathbf{u}}}} \delta_{\mathbf{x}} + \frac{\partial f(\mathbf{x}, \mathbf{u})}{\partial \mathbf{u}} \Big|_{\substack{\mathbf{x}=\bar{\mathbf{x}} \\ \mathbf{u}=\bar{\mathbf{u}}}} \delta_{\mathbf{u}} \quad (2.45)$$

The equation (2.45) describes a linear time-invariant representation of the non-linear dynamics of the quadrotor near an equilibrium point  $\bar{\mathbf{x}}$  and with an input that tends to be  $\bar{\mathbf{u}}$ , which is established as a state space model

$$\dot{\mathbf{x}}(t) = A\mathbf{x}(t) + B\mathbf{u}(t) \quad (2.46)$$

where

$$\mathbf{x} = [x \ \dot{x} \ y \ \dot{y} \ z \ \dot{z} \ \psi \ \dot{\psi} \ \theta \ \dot{\theta} \ \phi \ \dot{\phi}]^T,$$

$$\mathbf{u} = [T_u \ \tau_\psi \ \tau_\theta \ \tau_\phi]^T,$$

$$A = \frac{\partial f(\mathbf{x}, \mathbf{u})}{\partial \mathbf{x}} \Big|_{\substack{\mathbf{x}=\bar{\mathbf{x}} \\ \mathbf{u}=\bar{\mathbf{u}}}} = \begin{bmatrix} 0 & 1 & 0 & 0 & 0 & 0 & 0 & 0 & 0 & 0 & 0 & 0 \\ 0 & 0 & 0 & 0 & 0 & 0 & 0 & 0 & g & 0 & 0 & 0 \\ 0 & 0 & 0 & 1 & 0 & 0 & 0 & 0 & 0 & 0 & 0 & 0 \\ 0 & 0 & 0 & 0 & 0 & 0 & 0 & 0 & 0 & 0 & g & 0 \\ 0 & 0 & 0 & 0 & 0 & 1 & 0 & 0 & 0 & 0 & 0 & 0 \\ 0 & 0 & 0 & 0 & 0 & 0 & 0 & 0 & 0 & 0 & 0 & 0 \\ 0 & 0 & 0 & 0 & 0 & 0 & 0 & 0 & 0 & 0 & 0 & 0 \\ 0 & 0 & 0 & 0 & 0 & 0 & 0 & 0 & 0 & 0 & 0 & 0 \\ 0 & 0 & 0 & 0 & 0 & 0 & 0 & 0 & 0 & 0 & 0 & 0 \\ 0 & 0 & 0 & 0 & 0 & 0 & 0 & 0 & 0 & 0 & 0 & 0 \\ 0 & 0 & 0 & 0 & 0 & 0 & 0 & 0 & 0 & 0 & 0 & 0 \\ 0 & 0 & 0 & 0 & 0 & 0 & 0 & 0 & 0 & 0 & 0 & 0 \end{bmatrix}, \quad (2.47)$$

$$B = \frac{\partial f(\mathbf{x}, \mathbf{u})}{\partial \mathbf{u}} \Big|_{\substack{\mathbf{x}=\bar{\mathbf{x}} \\ \mathbf{u}=\bar{\mathbf{u}}}} = \begin{bmatrix} 0 & 0 & 0 & 0 & 0 & \frac{1}{m} & 0 & 0 & 0 & 0 & 0 & 0 \\ 0 & 0 & 0 & 0 & 0 & 0 & 0 & \frac{1}{J_{zz}} & 0 & 0 & 0 & 0 \\ 0 & 0 & 0 & 0 & 0 & 0 & 0 & 0 & 0 & \frac{1}{J_{yy}} & 0 & 0 \\ 0 & 0 & 0 & 0 & 0 & 0 & 0 & 0 & 0 & 0 & 0 & \frac{1}{J_{xx}} \end{bmatrix}^T.$$

### 2.3.2 Thrust Compensation

Given the fact that the forces  $F_{M_i}$  applied by the motors in the quadrotor are parallel to the body-frame  $z$ -axis and not to the earth-frame  $Z_W$ -axis, a compensated thrust input  $u_1^*$  must be set so that its projection  $u_1$  (third component of  $F_\xi$ ) on the  $Z_W$ -axis is such that it allows to keep the inputs of the system close to the equilibrium input, even though there are deviations in  $\theta$  or  $\phi$ .

Given the linearization consideration where the  $z$  and  $Z_W$  axes coincide, if a linear controller is designed to control the quadrotor, it takes the projection  $u_1$  of  $u_1^* = T_u$  on the  $Z_W$ -axis as its thrust control signal. From linear algebra, and following the geometry seen in Fig. 2.2, the projection  $u_1$  is defined as

$$u_1 = u_1^* \cos(\theta) \cos(\phi), \quad (2.48)$$

for any  $|\theta|$  and  $|\phi|$  magnitudes greater than zero. Thus, after each iteration of the control algorithm the real thrust input  $u_1^*$  is calculated as

$$u_1^* = \frac{u_1}{\cos(\theta) \cos(\phi)}, \quad (2.49)$$

keeping the desired vertical thrust, despite any deviation about the  $x$  or  $y$  axes.

For simplicity, the rest of the document assumes that  $u_1 = u_1^*$ , however during the real implementation the thrust compensation is taken into account.

## 2.4 Conclusions

This chapter describes the dynamic model of the quadrotor system, based on its reference frame and geometry configuration. The ‘+’ and ‘X’ quadrotor configurations are detailed, including the setting of the quadrotor inputs and its dependence on the quadrotor motors forces. The dynamic model is obtained using the Newton-Euler approach, for a body-frame base model, and an Euler-Lagrange approach, for a hybrid earth-frame-position/body-frame-attitude model. In order to design linear controllers for the flight dynamics of the quadrotor, a Jacobian linearization about an equilibrium point is implemented. This linearized model is valid for low translational and rotation speed flights with small angular deviations, where both of the non-linear models, got from different approaches, tend to be equivalent. This equilibrium point is achieved by an equilibrium input, which must be added to any control action set by the controller during its implementation. Finally, it is considered the decompensation of the force set by the controller to be exerted by the motors on the earth-frame  $Z_W$ -axis, so that it can be compensated in the real quadrotor implementation.

# Chapter 3

## Smartphone-based Quadrotor Prototype

In this chapter, the quadrotor prototype is presented. All the components that are used to build the prototype are described with the purpose of detailing the function that each component fulfils within the quadrotor. Furthermore, the specific parameters of the built quadrotor are shown and the procedure carried out to find them experimentally is explained. This is of great importance for the design of the controllers that allow the flight of the built system.

In Fig. 3.1, a small overview of the hardware related to the electrical signals within the quadrotor is presented. This overview shows the interrelation between the main components detailed below.

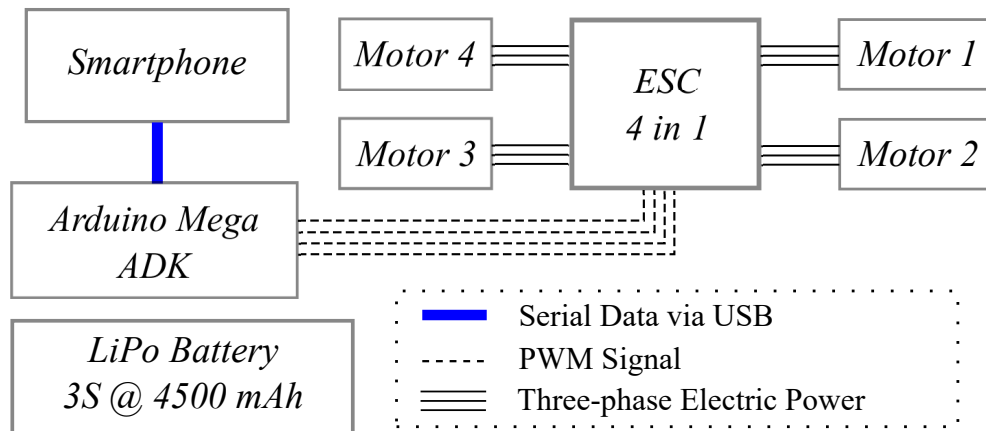


Figure 3.1: Quadrotor prototype's hardware overview

## 3.1 Quadrotor Components

The hardware used to build the quadrotor prototype is detailed in this section. The main goal of this research project is to control a quadrotor using just a smartphone on-board. This smartphone executes the state estimation algorithms and defines the controls signals that will command the actuators. The control signals are processed in the smartphone and then sent, through a gateway, to the Electronic Speed Controllers (ESCs) that will set the angular speed of the motors depending on the control signal they receive.

### 3.1.1 Frame

The quadrotor's frame is responsible for carrying all the other components needed in the system. Additionally, it must be able to support the weight of any possible payload that the quadrotor will carry. The multirotors frames are usually built using fiberglass or carbon fiber as main material, being the carbon fiber frames stiffer and lighter than equally built fiberglass frames.

For this project, the requirement to build a quadrotor between 0.20 and 0.30 *cm* in radius was defined. This requirement is based on the fact that the quadrotor must carry a smartphone and possibly some mission-related payloads, which weight can be greater than 100 *g*. Taking that requirement and the literature review into account, in addition to the weight and stiffness advantages of the carbon fiber, a LJI 500-X4 carbon fiber frame was selected.



Figure 3.2: LJI 500-X4 carbon fiber frame<sup>1</sup>

This frame (Fig. 3.2) has a weight of 431 *g* and a radius  $L$  of 0.244 *m* measured between the frame center and each of the four rotor axis holes. Its landing gear

---

<sup>1</sup>LJI 500-X4 frame image taken from <https://goo.gl/hHfHQR>

has a height of  $0.170\text{ m}$ , allowing the payload to be placed in the lower part of the quadrotor.

### 3.1.2 Smartphone

In this project, the smartphone takes the place of the quadrotor's flight controller. The basic instrumentation needed for a flight controller includes a triaxial accelerometer, a triaxial gyroscope, a triaxial magnetometer, a barometer and a GNSS receiver that can process signals from the GPS and GLONASS satellites constellations. On the other side, the processor of a flight controller must be powerful enough to execute the control and estimation algorithms within the sample time of the control system.

The LG Nexus 5X, shown in Fig. 3.3, is a smartphone developed by Google and assembled by LG, released in 2015 with the Android 6.0.1 operating system. This phone has a Hexa-core Qualcomm MSM8992 Snapdragon 808 CPU that includes four Cortex-A53 and two Cortex-A57 cores with 1.4 GHz and 1.8 GHz clock rate respectively and an Adreno 418 GPU. Its features also include 2 GB of RAM memory, 32 GB of Flash memory, total mass of 136 g and a 12.3 MP camera.



Figure 3.3: LG Nexus 5X, smartphone used as flight controller<sup>2</sup>

This smartphone features all the needed instrumentation for a flight controller, specified previously. The maximum sample rates of the instrumentation contained in the LG Nexus 5X are described in Table 3.1.

---

<sup>2</sup>LG Nexus 5X image taken from <https://goo.gl/RxyDJd>

Table 3.1: Sample Rates of the Sensors in the Smartphone

Sensor	Sample rate [Hz]
Triaxis accelerometer	400
Triaxis gyroscope	200
Triaxis magnetometer	50
Barometer	10
GNSS	1

The LG Nexus 5X smartphone was selected in this project mainly due to its computational and instrumentation capabilities in addition to its communication interfaces (Bluetooth 4.0, Wireless LAN, USB Type-C and GSM). Its powerful CPU handling a GPU enables the possibility of developments using the camera for visual odometry, and controllers whose execution represents a high computational load, which exceeds the limits of a standard microcontroller such as the ATmega 2560.

As the quadrotor's flight controller, the smartphone receives remote orders from the quadrotor's pilot using wireless communication, while executing the sensorial, estimation and control algorithms. After the control signals are calculated, they are sent to the actuators as a serial data frame using the USB interface between the smartphone and a gateway that converts the serial data into PWM signals.

### 3.1.3 Motors and Electronic Speed Controllers

The actuation system of the quadrotor is composed by R/C-type brushless motors, propellers and ESCs. The LJI 500-X4 frame manufacturer recommends using motors with a RPM constant of 810 *KV*, which means that these motors can rotate at a speed of 810 *RPM* for each Volt applied to it. This kind of motors are used from medium to big sized multirotors due to its thrust efficiency and thrust capacity.

Following this recommendation, the EMAX MT2216II motors were selected. These motors, shown in Fig. 3.4a, are labelled by its manufacturer as 810 *KV* motors with a maximum current consumption of 9.8 *A* and a maximum thrust of 6.6 *N*, when using a 10-inch propeller.

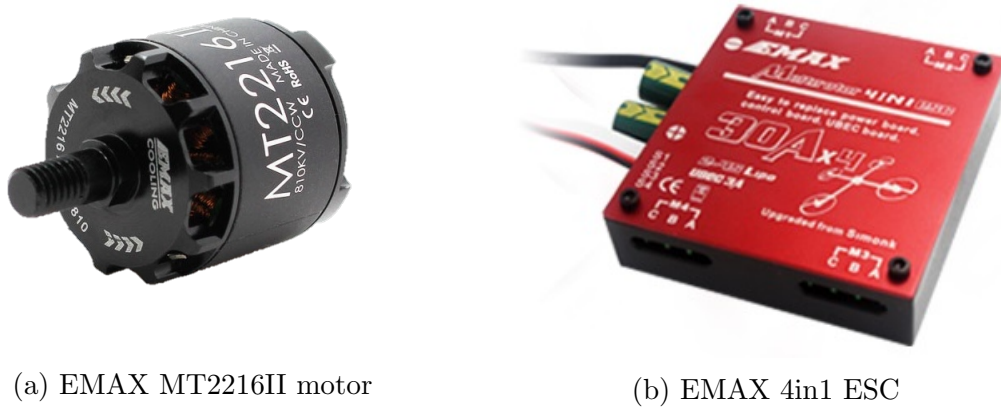


Figure 3.4: Motors and ESC used in the Quadrotor<sup>3</sup>

The quadrotor brushless motors are powered using a three-phase electric signal generated by the ESC. Each ESC sets one motor rotational velocity depending on a PWM signal input, and must be able to handle the maximum current consumption of the motor. Mainly due to the ease of handling and positioning within the frame, the EMAX 4in1 ESC was selected for this project (Fig. 3.4b). This 4in1 ESC contains four ESCs with a maximum current supply of 30 A each. It also has a DC-DC converter that outputs an isolated 5 V DC supply for any additional electronics. The power supply of the ESC is fully delivered by the quadrotor's battery.

### 3.1.4 Smartphone-to-ESC Gateway

As the smartphone can not generate any PWM signal and each ESC needs a PWM signal input to set the rotational velocity of a motor, a gateway between the smartphone and the ESCs must be used. In order to avoid interference in the electromagnetic spectrum and delays that could lead the control system to instability while using wireless communications, the smartphone wired serial bus (USB interface) is defined as the only channel of communication through which the control signals are sent to the gateway.

The Arduino Mega ADK, is shown in Fig. 3.5, is a development board based on the Atmel 8-bit AVR RISC-based ATmega2560 microcontroller. This board supports the Android Open Accessory (AOA) protocol, which allows external hardware to exchange data with Android devices.

---

<sup>3</sup>Taken from <https://goo.gl/6qD6Qg> and <https://goo.gl/fDHiUp>

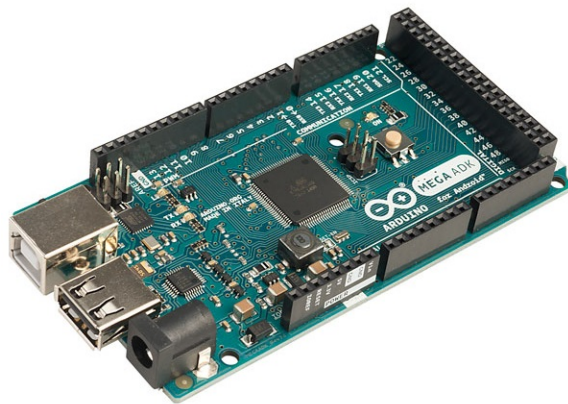


Figure 3.5: Arduino Mega ADK<sup>4</sup>

Although there are other boards that support the AOA protocol, as the IOIO board, the Arduino Mega ADK offers the possibility of executing tasks in the ATmega2560 microcontroller without any intervention of the Android device. This feature is very useful in case of future developments that include additional hardware to the smartphone-based quadrotor.

The Arduino Mega ADK is selected as the smartphone-to-ESC gateway. The workflow of this board is set as follows: the microcontroller receives a serial data frame from the smartphone through the USB port, each of the four PWM signal widths is extracted from the data frame, the PWM signals are sent to the ESCs, finally the cycle starts again. This workflow is executed each  $2\text{ ms}$  and if the gateway does not receive any updated data frame from the smartphone, it keeps the last PWM signals set.

### 3.1.5 Battery

The quadrotor's battery must supply power to all the active components in the quadrotor. The maximum power consumption of these components, based on the nominal voltage value of a 3-cells lithium-ion polymer (LiPo) battery ( $11.1\text{ V}$ ), is shown below.

The maximum current consumption in the quadrotor reaches  $42.08\text{ A}$ , so the battery must be able to deliver current amplitudes greater than that value. A Floureon 3-cells LiPo battery with a nominal capacity of  $4500\text{ mAh}$  and a nominal voltage of  $11.1\text{ V}$ , was selected for this prototype and is shown in Fig. 3.6. This battery can deliver up to 30 times its nominal current, this is  $135\text{ A}$ , continuously.

---

<sup>4</sup>Arduino Mega ADK image taken from <https://goo.gl/ejeQeX>

Table 3.2: Maximum Power Consumption of the Quadrotor's Components

Component	Voltage [V]	Max. Current [A]	Max. Power [W]
Smartphone	5	0.75	3.75
Arduino Mega ADK	11.1	0.75	8.33
4 x ESCs	11.1	1.38	15.32
4 x Motors	11.1	39.2	435.12

Figure 3.6: LiPo battery that powers the Quadrotor<sup>5</sup>

### 3.1.6 3D-printed Parts

The smartphone, the Arduino Mega ADK and the 4in1 ESC need to be easily placed and protected when installed on the frame. For that reason, multiple support components and one case were designed and 3D-printed using polylactic acid (PLA) filament. These 3D-printed objects are detailed below.

#### Smartphone Support

In order to place the smartphone near the *CoG* in the quadrotor and enable the possibility of capturing nadir photos or videos, the smartphone support is designed in such a way that it can be placed under the quadrotor's *CoG* but above the landing gear of the frame. Additionally, the support includes a free area that allows to use the complete field of view of the camera without being obstructed by it. The smartphone support is shown in Fig. 3.7.

#### Arduino Mega ADK and ESC supports

The Arduino Mega ADK and the Emax 4in1 ESC are placed on the frame, above the quadrotor's *CoG*. Given the limited space available to locate these components

---

<sup>5</sup>Floureon 3S LiPo battery image taken from <https://goo.gl/anC9M2>



Figure 3.7: Smartphone support

on the top of the frame, their supports are designed to be placed one on top of the other, as shown in Fig. 3.8.

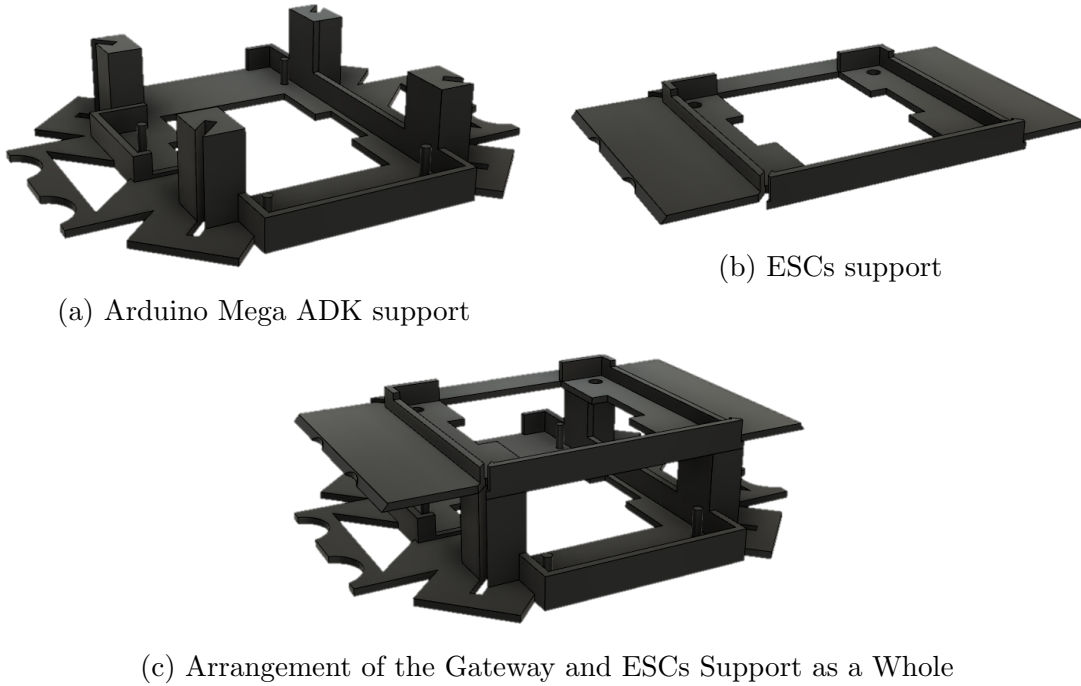


Figure 3.8: Arduino Mega ADK and EMAX 4in1 ESCs designed supports

## Dome

To protect the Arduino Mega ADK and the ESCs, a dome that covers and encloses them is designed. This dome, shown in Fig. 3.9, totally encloses the Mega ADK and

ESCs supports restricting their movement and protecting them in case of a shock or hit.

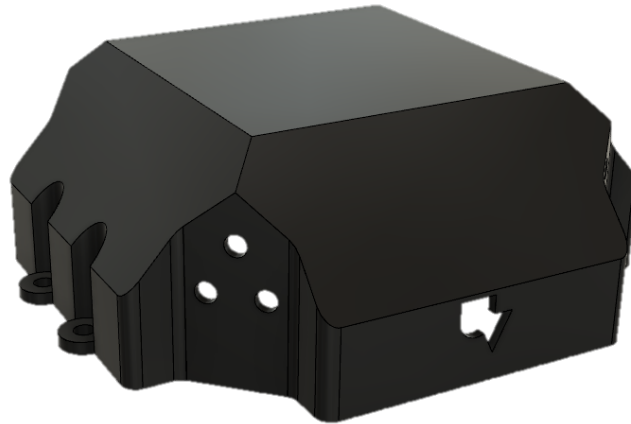


Figure 3.9: 3D Designed Dome

### 3.1.7 Assembled Smartphone-based Quadrotor

The smartphone-based quadrotor prototype is assembled using all the components exposed in this section, and is shown in Fig. 3.10.



Figure 3.10: Assembled Smartphone-based Quadrotor Prototype

## 3.2 Quadrotor Parameters

In this section, the quadrotor parameters are detailed. These parameters define the specific dynamic model for the smartphone-based quadrotor prototype and the conversion of control signals to correctly set the motors thrust.

### 3.2.1 Mass

The mass of each quadrotor's component is measured using a kitchen scale that has an uncertainty of  $\pm 1\text{ g}$ . The results are shown in Table 3.3.

The total mass of the quadrotor  $m$  is then calculated as the sum of the weight of each of the components in the quadrotor, being  $m = 1.568\text{ kg}$ .

Table 3.3: Mass values of all the Quadrotor's components

Component	Mass [kg]
Smartphone	0.136
Frame	0.431
Battery	0.351
ESC	0.110
Arduino Mega ADK	0.330
Motors (4)	0.140
Propellers (4)	0.380
Smartphone support	0.105
ADK support	0.590
ESC support	0.350
Dome	0.130
Total	1.568

### 3.2.2 Moments of Inertia

As exposed by [67], in a quadrotor, the moment of inertia matrix  $\mathbf{J}$  is set as

$$\mathbf{J} = \begin{bmatrix} J_{xx} & -J_{xy} & -J_{xz} \\ -J_{yx} & J_{yy} & -J_{yz} \\ -J_{zx} & -J_{zy} & J_{zz} \end{bmatrix}. \quad (3.1)$$

Taking into account that the symmetry of the quadrotor with respect to the  $x$  and  $y$  axes is assumed, the  $\mathbf{J}$  matrix can be approximated to

$$\mathbf{J} \approx \begin{bmatrix} J_{xx} & 0 & 0 \\ 0 & J_{yy} & 0 \\ 0 & 0 & J_{zz} \end{bmatrix}. \quad (3.2)$$

The  $J_{xx}$ ,  $J_{yy}$  and  $J_{zz}$  values can be obtained using multiple methods including: using a CAD model of the quadrotor and obtaining the inertia values from a 3D design software ([68]), approximating the shape of the quadrotor components to cylinders, cubes and other basic shapes to simplify the mathematical calculation of inertia ([69]), and developing the bifilar pendulum experiment on the quadrotor ([70]). For this project, it was decided to obtain the quadrotor parameters experimentally, so the bifilar pendulum experiment was developed.

In the bifilar pendulum experiment, an object is hung from two parallel ropes of length  $r$  and separated by a distance  $2l$ , being allowed to rotate freely around a the

axis that is parallel to the ropes. In Fig. 3.11, the geometry of the experiment to get  $J_{zz}$ , is shown. For the  $J_{xx}$  and  $J_{yy}$  inertias experiment, it is necessary to place the quadrotor hanging in such a way that the  $x$  and  $y$  axes are pointing parallel to the ropes, respectively.

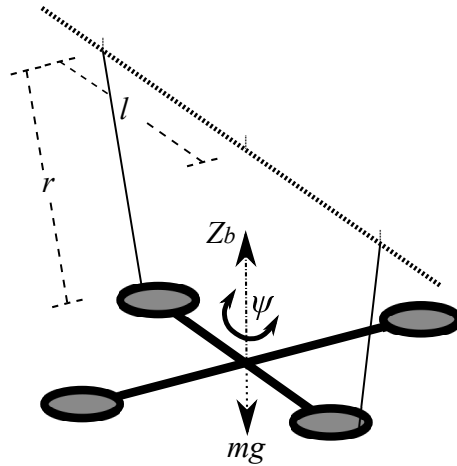


Figure 3.11: Bifilar pendulum experiment geometry for inertia identification

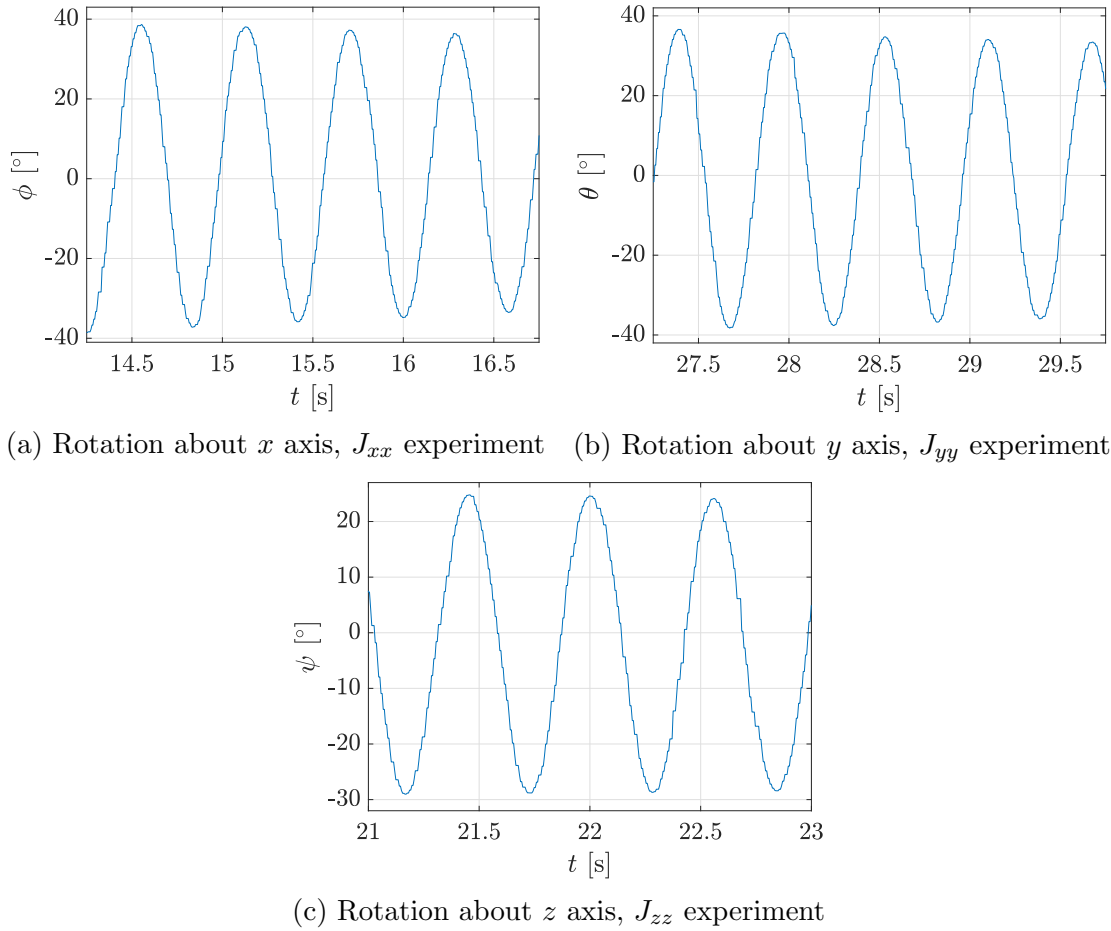
Once the quadrotor is hanging from the ropes, a small torque is applied manually to the quadrotor making it rotate about the vertical axis. The tension in the ropes makes the quadrotor swing, with a period of  $T_{osc}$  [s], about the rotation axis.

The moment of inertia is then calculated using the bifilar equation

$$J_{..} = \frac{mgT_{osc}^2l^2}{4\pi^2r} [kg \cdot m^2], \quad (3.3)$$

where  $m = 1.568 \text{ kg}$  is the quadrotor's total mass and  $g = 9.807 \text{ m/s}^2$  is the gravity acceleration magnitude ([71]).

In Fig. 3.12, it is shown the excursion of the rotation angles,  $\phi$ ,  $\theta$  and  $\psi$ , about the  $x$ ,  $y$  and  $z$  axes respectively, while performing the bifilar pendulum experiment separately.

Figure 3.12: Rotation about  $x$ ,  $y$  and  $z$  axes during the bifilar pendulum experiments

The resulting data got after the execution of the experiment around the three components of the quadrotor body frame, are shown in Table 3.4.

Table 3.4: Bifilar pendulum experiment results

Rotation Axis	$r$ [m]	$l$ [m]	$T_{osc}$ [s]	Inertia value [ $kg \cdot m^2$ ]
$x$	1.18	0.173	1.168	$J_{xx} = 0.0135$
$y$	1.10	0.173	1.080	$J_{yy} = 0.0124$
$z$	1.025	0.265	1.122	$J_{zz} = 0.0336$

### 3.2.3 Motors Thrust

As seen in Section 3.1, the motors rotational velocity  $\omega_i$  is set by the ESC, which receives a *PWM* signal input. However, the inputs of the quadrotor ( $T_u$ ,  $\tau_\psi$ ,  $\tau_\theta$ , and  $\tau_\phi$ ) depend on the thrust force  $F_{M_i}$  applied by each quadrotor motor, as exposed in Section 2.1.

In order to correctly set the desired force  $F_{M_i}$  in each motor during a flight, it is necessary to characterize the motor; and thus know how the force applied by the motor behaves with respect to the input *PWM* signal. This characterization is carried out by means of a thrust test.

In the thrust test, the motor and its corresponding propeller are fixed pointing up over a calibrated scale, as shown in Fig. 3.13, while connected to the ESC, and then the *PWM* signal is increased with steps of 10, with 0 being the minimum width of *PWM* signal and 255 the maximum, until reaching the maximum *PWM* width.

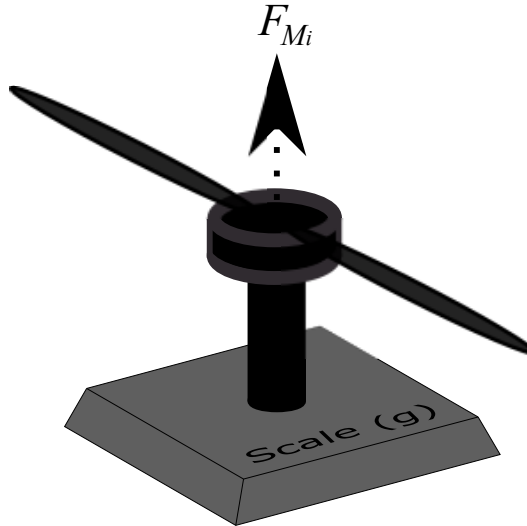


Figure 3.13: Thrust test configuration

With each *PWM* signal width increment, a scale reading is made. Since the readings  $m_s$  are obtained in units of mass ( $kg$ ), the  $F_{M_i}$  must be calculated as

$$F_{M_i} = m_s g \quad [N]. \quad (3.4)$$

This test was developed twice with each motor and its results are shown in Fig. 3.14a.

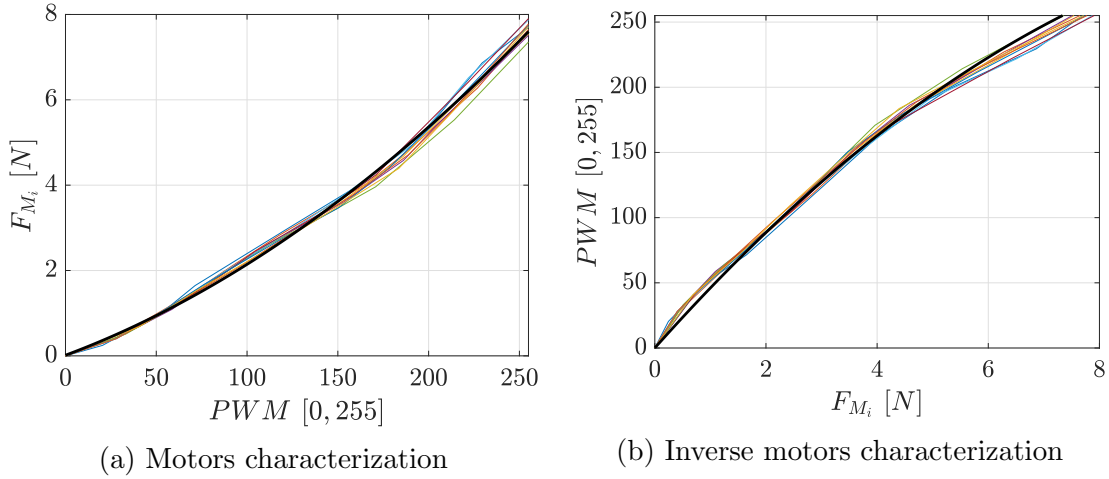


Figure 3.14: Motors thrust test results

In Fig. 3.14b, the inverse characterization is exposed. In this case, the  $PWM$  signal is defined as the dependent variable, and  $F_{M_i}$  as independent. This inverse characterization defines the  $PWM$  width setting that is sent from the smartphone to the Arduino Mega ADK.

The trend equations resulting from the thrust test are

$$F_{M_i} = (5.441 \times 10^{-5})(PWM)^2 + 0.01586(PWM) + 0.014808, \quad (3.5)$$

$$PWM = -1.983F_{M_i}^2 + 47.84F_{M_i} + 3.835, \quad (3.6)$$

where  $F_{M_i}$  is given in  $N$ , and  $PWM$  is a value between 0 and 255.

### 3.2.4 Motors Torque

The quadrotor suffers the application of a torque  $\tau_{M_i}$  around the  $z$  axis when a motor  $M_i$  rotates. This torque affects the  $\psi$  angle indirectly by adding to the  $\tau_\psi$  torque proportionally to the thrust force  $F_{M_i}$ , being  $\tau_{M_i} = K_M F_{M_i}$ , as shown in (2.3).

The torque  $\tau_{M_i}$  is generated due to the conservation of momentum, and its unbalance is used to rotate the quadrotor about the  $z$  axis in the opposite direction to the rotation of the motor that generates it as exposed in Section 2.1. In order to properly control the mentioned unbalance, it is necessary to find the value of the constant  $K_m$ .

The constant  $K_m$  can be found through a steady-state torque experiment, as stated by [72]. In this experiment, the  $z$  axis in the quadrotor is located parallel to the ground, leaving the rotation about this axis as the only unblocked *DoF*. Using the

geometry seen in Fig. 3.15, it is necessary to measure the force  $F_s$  that is generated when the motor  $M_i$  is rotating.

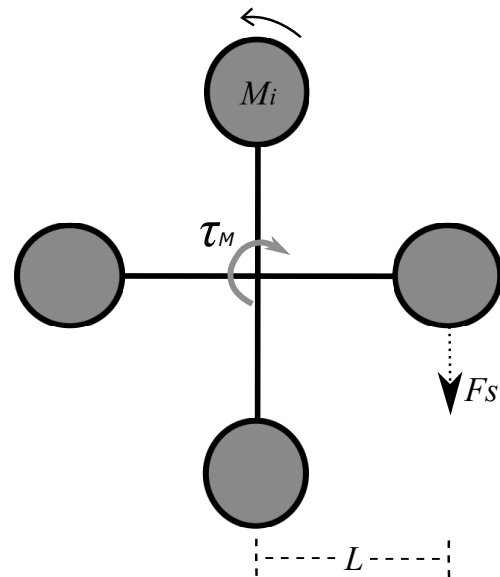


Figure 3.15: Motors torque experiment configuration

Taking into account that when the motor rotates clockwise, the quadrotor will tend to rotate counter-clockwise and vice versa, a scale is located to indirectly obtain the generated force  $F_s$ , using the reading of the weight  $m_s$  as  $F_s = m_s|\vec{g}|$  [N]. Using (3.5) and the PWM width steps used in the motors thrust experiment, multiple  $F_{M_i}$ -dependent  $F_s$  readings are obtained. The torques  $\tau_M$  are then calculated by

$$\tau_M = F_s L \text{ [N} \cdot \text{m}], \quad (3.7)$$

and their results are shown in Fig. 3.16.

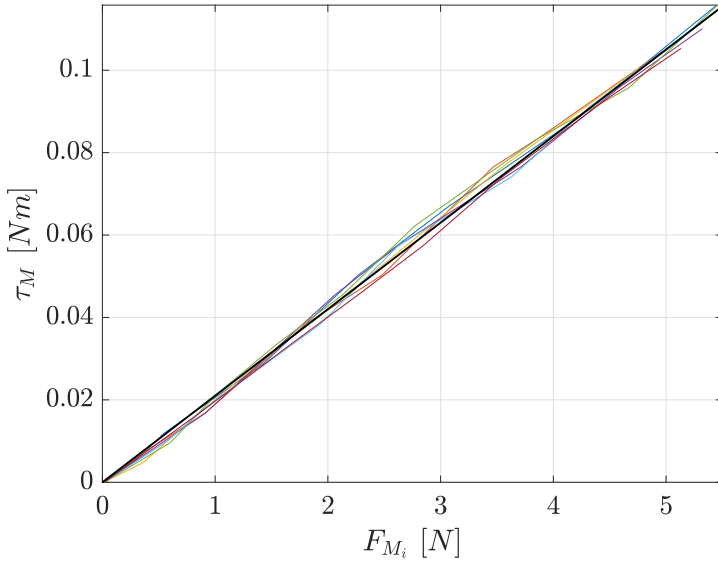


Figure 3.16: Motors torque experiment results

The relation between  $\tau_M$  and  $F_{M_i}$  is linear as expected, and its slope defines the variable  $K_m$  as

$$K_m = 0.021 \text{ [m].} \quad (3.8)$$

### 3.3 Conclusions

This chapter presented the physical composition and parametrization of the smartphone-based quadrotor prototype. In the first part, all the components of the quadrotor are detailed. A medium-size carbon fiber frame is used to support the complete quadrotor system. The LG Nexus 5X is selected as the smartphone where the control and estimation algorithms will be executed, which sends the control signals to an Arduino Mega ADK in order to generate *PWM* signals that set the motors rotational velocities through the ESC. These components are supported and protected by 3D-printed objects that are attached to the carbon fiber frame. On the other hand, the system is parameterized in its entirety using experimental methods. Here, the total mass and moments of inertia of the system are defined using a scale and the bifilar pendulum experiment respectively, while the motor's thrust and torque about the *z*-axis are found applying multiple *PWM* signals to the ESCs and obtaining the corresponding variable with the help of the scale.



# Chapter 4

## Control Strategies and State Estimation

This project seeks to evaluate control strategies designed for a quadrotor, test its performance in simulation, and then implement them in the smartphone-based quadrotor prototype. In this chapter, the design procedure of the control and estimation algorithms for the quadrotor is shown. These algorithms are based on the linearized model of the quadrotor, detailed in Section 2.3. Also, all the simulations carried out in MATLAB to verify the proper functioning of the designed algorithms are exposed.

The state-space representation of the system, and the concept of controllability and observability, are briefly introduced in Section 4.1. Then, Section 4.2 shows the theoretical basis required for the design of the controllers used in this project. These controllers are the Linear Quadratic Integral (LQI) controller and the  $H_\infty$  controller.

Section 4.3 presents the considerations made for the design of the two types of controllers according to the flight mode of the quadrotor. In addition, this section shows the simulated response of the quadrotor being controlled by both types of controllers in each flight mode. All the simulations are done using the non-linear dynamics model of the quadrotor.

Finally, the state estimation algorithm developed mainly for the case of the LQI controller, is detailed in Section 4.4.

## 4.1 Concept and Generalities

### 4.1.1 State Space Representation

Recalling from Section 2.3, the dynamic model of the quadrotor, based on its six *DoF*, is represented by the linear state-space model

$$\begin{aligned}\dot{\mathbf{x}}(t) &= A\mathbf{x}(t) + B\mathbf{u}(t), \\ \mathbf{y}(t) &= C\mathbf{x}(t) + D\mathbf{u}(t),\end{aligned}\tag{4.1}$$

where  $A$  is the system matrix;  $B$  is the input matrix;  $C$  is the output matrix;  $D$  is the feed-through matrix;  $\mathbf{x}$  is the states vector of size  $n_x$ ;  $\mathbf{u}$  is the inputs vector of size  $n_u$ ; and  $\mathbf{y}$  is the outputs vector of size  $n_y$ .

For simplicity, the state-space model representation shown in (4.3), can be represented by the quartet of matrices  $\mathcal{G}$  as

$$\mathcal{G} = \left[ \begin{array}{c|c} A & B \\ \hline C & D \end{array} \right],\tag{4.2}$$

For the design of each controller, only the dynamics that are required to control, according to the flight mode in which the quadrotor is set, are taken into account. Therefore, system  $\mathcal{G}$  will vary for each flight mode.

Since the control system is implemented in a smartphone, whose algorithms are executed with a sample time of  $t_k = 0.01$  s, the system  $\mathcal{G}$  is discretized. The discrete system  $\mathcal{G}_k$  is got using the Zero Order Hold (ZOH) equivalent method, and the sample time  $t_k = 0.01$  s. The discrete state-space model  $\mathcal{G}_k$  is represented by

$$\begin{aligned}\mathbf{x}(k+1) &= A_k\mathbf{x}(k) + B_k\mathbf{u}(k), \\ \mathbf{y}(k+1) &= C_k\mathbf{x}(k) + D_k\mathbf{u}(k).\end{aligned}\tag{4.3}$$

Thus,  $\mathcal{G}_k$  is represented by the quartet

$$\mathcal{G}_k = \left[ \begin{array}{c|c} A_k & B_k \\ \hline C_k & D_k \end{array} \right],\tag{4.4}$$

which is the system for which the controllers are developed.

### 4.1.2 Controllability and Observability

The concept of controllability is related to the question of whether or not there exists a sequence of  $\mathbf{u}$  capable of changing the states  $\mathbf{x}$  from an initial value  $\mathbf{x}_0$ , to

a desired final value  $\mathbf{x}_f$ , in a finite time. On the other hand, observability refers to the possibility of inferring, in finite time, the initial value of the states  $\mathbf{x}_0$  knowing just the system dynamics  $\mathcal{G}$  and its outputs  $\mathbf{y}$  [73].

Typically, the controllability and observability of a system are determined using the so-called controllability and observability matrices,  $\mathcal{C}_{\mathcal{G}}$  and  $\mathcal{O}_{\mathcal{G}}$  respectively. These matrices depend on the system matrices  $A$ ,  $B$  and  $C$ , and are set as

$$\begin{aligned}\mathcal{C}_{\mathcal{G}} &= [B \ AB \ \dots \ A^{k-1}B], \\ \mathcal{O}_{\mathcal{G}} &= \begin{bmatrix} C \\ CA \\ \vdots \\ CA^{k-1} \end{bmatrix}.\end{aligned}\tag{4.5}$$

Thus, the system  $\mathcal{G}$  is defined as controllable if  $\mathcal{C}_{\mathcal{G}}$  have  $n_x$  linear independent rows (or columns). This is, the rank of  $\mathcal{C}_{\mathcal{G}}$  is equal to  $n_x$ . Analogous to the controllability, the observability of  $\mathcal{G}$  is checked if the rank of the matrix  $\mathcal{O}_{\mathcal{G}}$  is equal to  $n_x$ .

One equivalent way to check the controllability and observability features of  $\mathcal{G}$  is using the controllability and observability Grammians  $\mathcal{W}_c$  and  $\mathcal{W}_o$  defined as the solutions to the Lyapunov equations

$$\begin{aligned}0 &= A\mathcal{W}_c + \mathcal{W}_cA^T + BB^T, \\ 0 &= A^T\mathcal{W}_o + \mathcal{W}_oA + C^TC,\end{aligned}\tag{4.6}$$

where

$$\begin{aligned}\mathcal{W}_c &= \int_0^\infty e^{At}BB^Te^{A^Tt}dt, \\ \mathcal{W}_o &= \int_0^\infty e^{A^Tt}C^TCe^{At}dt.\end{aligned}\tag{4.7}$$

In this case, if the matrices  $\mathcal{W}_c$  and  $\mathcal{W}_o$  are positive definite, the system is both controllable and observable [74].

## 4.2 Control Strategies

This section exposes the controllers design procedure. Here, the mathematical procedure to design a linear quadratic integral controller is described. It includes a regulator and an estimator, in addition to a gain compensator, allowing the system to track a trajectory. The design process of a  $H_\infty$  controller is shown, taking into account some weighting sensitivities.

### 4.2.1 Linear Quadratic Integral (LQI) Controller

#### Optimal Problem Solution

The design of optimal controllers seeks that a dynamic system can be controlled achieving a minimum cost. The cost function is determined by the control designer [75]. Designing an finite-time regulator, a linear quadratic regulator (LQR) is set while looking for the minimization of the cost function  $\mathcal{V}$  as

$$\mathcal{V} = \int_0^T \mathcal{L}(\mathbf{x}, \mathbf{u}, t) dt + \Psi(\mathbf{x}, \mathbf{u}, t), \quad (4.8)$$

where

$$\begin{aligned} \mathcal{L}(\mathbf{x}, \mathbf{u}, t) &= \mathbf{x}^T \mathcal{Q} \mathbf{x} + \mathbf{u}^T \mathcal{R} \mathbf{u}, \\ \Psi(\mathbf{x}, \mathbf{u}, t) &= \mathbf{x}^T(T) \mathcal{S} \mathbf{x}(T), \end{aligned} \quad (4.9)$$

$\mathcal{R}$  is a positive definite matrix; and  $\mathcal{Q}$  and  $\mathcal{S}$  are positive semi-definite matrices. These matrices penalize the inputs, states and the terminal cost, respectively. Thus, the optimal controller design problem turns into an optimization problem where it is necessary to find an input  $\mathbf{u}^*$  such that minimizes  $\mathcal{V}$  for a controllable system subject to

$$\begin{aligned} \dot{\mathbf{x}}(t) &= \mathbf{f}(\mathbf{x}, \mathbf{u}, t) \approx A\mathbf{x}(t) + B\mathbf{u}(t), \\ \mathbf{x}(0) &= \mathbf{x}_0, \quad t \in [0, T]. \end{aligned} \quad (4.10)$$

This minimization is achieved using the Pontryagin maximum principle [76], where

$$\mathcal{H}(\mathbf{x}, \mathbf{u}, \lambda_{\mathcal{P}}, t) = \mathcal{L}(\mathbf{x}, \mathbf{u}, t) + \lambda_{\mathcal{P}}^T \mathbf{f}(\mathbf{x}, \mathbf{u}, t) \quad (4.11)$$

is the Hamiltonian function, with  $\lambda_{\mathcal{P}}$  being the vector of co-state variables of size  $n_x$ , and

$$\begin{aligned} \dot{\mathbf{x}}(t) &= \left( \frac{\partial \mathcal{H}(\mathbf{x}, \mathbf{u}, \lambda_{\mathcal{P}}, t)}{\partial \lambda_{\mathcal{P}}} \right)^T = A\mathbf{x}(t) + B\mathbf{u}(t), \\ -\dot{\lambda}_{\mathcal{P}}(t) &= \left( \frac{\partial \mathcal{H}(\mathbf{x}, \mathbf{u}, \lambda_{\mathcal{P}}, t)}{\partial \mathbf{x}} \right)^T = \mathcal{Q}\mathbf{x}(t) + A^T \lambda_{\mathcal{P}}(t), \\ 0 &= \frac{\partial \mathcal{H}(\mathbf{x}, \mathbf{u}, \lambda_{\mathcal{P}}, t)}{\partial \mathbf{u}} = \mathcal{R}\mathbf{u}(t) + \lambda_{\mathcal{P}}^T(t)B. \end{aligned} \quad (4.12)$$

Thereby, from (4.12), the optimal solution to  $\mathbf{u}$  that minimizes  $\mathcal{H}(\mathbf{x}, \mathbf{u}, \lambda_{\mathcal{P}}, t)$ , and by Pontryagin maximum principle, the cost function  $\mathcal{V}$ , is

$$\mathbf{u}^*(t) = -\mathcal{R}^{-1} B^T \lambda_{\mathcal{P}}(t). \quad (4.13)$$

Assuming that  $\lambda_{\mathcal{P}}(t) = \mathcal{P}(t)\mathbf{x}(t)$ , the optimal input  $\mathbf{u}^*$  depends directly on a feedback vector, which is the state vector  $\mathbf{x}$ , such that

$$\begin{aligned}\mathbf{u}^*(t) &= \mathbf{K}_{\text{lqr}}(t)\mathbf{x}(t), \\ \mathbf{K}_{\text{lqr}}(t) &= -\mathcal{R}^{-1}B^T\mathcal{P}(t).\end{aligned}\tag{4.14}$$

Here, matrix  $\mathcal{P}(t)$  is a solution of the Riccati Equation [77]

$$-\dot{\mathcal{P}} = \mathcal{P}A + A^T\mathcal{P} + \mathcal{Q} - \mathcal{P}B\mathcal{R}^{-1}B^T\mathcal{P}.\tag{4.15}$$

When  $T \rightarrow \infty$ , an infinite-time regulator is designed. Here, aiming for a steady-state solution, the terminal cost  $\Psi(\mathbf{x}, \mathbf{u}, t)$  is eliminated, and the matrix  $\mathcal{P}$  is assumed to be constant. Thus,  $\mathcal{P}$  is a solution of the Algebraic Riccati Equation (ARE)

$$0 = \mathcal{P}A + A^T\mathcal{P} + \mathcal{Q} - \mathcal{P}B\mathcal{R}^{-1}B^T\mathcal{P}.\tag{4.16}$$

Consequently, in the infinite-time LQR, the optimal input  $\mathbf{u}^*$  is achieved by multiplying the state vector  $\mathbf{x}$  with the constant feedback gain matrix

$$\mathbf{K}_{\text{lqr}} = -\mathcal{R}^{-1}B^T\mathcal{P}.\tag{4.17}$$

As the feedback gain is not a dynamical system, but a static matrix, the order of the closed-loop dynamics is the same as the one of the system dynamics  $\mathcal{G}$ . The closed-loop dynamics are written as

$$\dot{\mathbf{x}} = (A + B\mathbf{K}_{\text{lqr}})\mathbf{x}.\tag{4.18}$$

When the desired state value  $\mathbf{x}_{\text{des}}$  is different from zero, this reference value is applied to the dynamics through the feedback gain matrix as

$$\dot{\mathbf{x}} = (A + B\mathbf{K}_{\text{lqr}})\mathbf{x} - B\mathbf{K}_{\text{lqr}}\mathbf{x}_{\text{des}},\tag{4.19}$$

due to the fact that the error  $\mathbf{e}_x = \mathbf{x} - \mathbf{x}_{\text{des}}$  is used as the feedback vector of the LQR.

## Reference Tracking

For the quadrotor position control, a controller capable of reference tracking is necessary. However, the LQR controller is not made for reference tracking, but just for regulation. This is overcome making use of a Linear Quadratic Integral (LQI) controller, which is a LQR with an additional integral feedback. The integral action ensures that a zero steady-state error is achieved.

The approach of using integral feedback with a LQR to provide tracking capabilities

to the control system, is based on the augmentation of the state vector  $\mathbf{x}$  with a vector

$$\mathbf{x}_i = \int \mathbf{e} dt, \quad \mathbf{x}_i(0) = \mathbf{0}, \quad \mathbf{x}_i \in \mathbb{R}^{n_y}, \quad (4.20)$$

containing the integral of the error signal  $\mathbf{e} = r - \mathbf{y}$ , where  $r$  is the reference signal of size  $n_y$ . The augmented state vector  $\mathbf{x}_{lqi}$  is defined as

$$\mathbf{x}_{lqi} = \begin{bmatrix} \mathbf{x} \\ \mathbf{x}_i \end{bmatrix}, \quad (4.21)$$

with which the augmented system to be controlled is obtained as

$$\begin{aligned} \dot{\mathbf{x}}_{lqi} &= \bar{A}\mathbf{x}_{lqi} + \bar{B}\mathbf{u} + B_ir, \\ \mathbf{y} &= \bar{C}\mathbf{x}_{lqi}, \end{aligned} \quad (4.22)$$

where

$$\begin{aligned} \bar{A} &= \begin{bmatrix} A & \mathbf{0}_{n_x \times n_y} \\ -C & \mathbf{0}_{n_y \times n_y} \end{bmatrix}, \\ \bar{B} &= \begin{bmatrix} B \\ \mathbf{0}_{n_y \times n_u} \end{bmatrix}, \\ B_r &= \begin{bmatrix} \mathbf{0}_{n_x \times n_y} \\ \mathcal{I}_{n_y \times n_y} \end{bmatrix}, \\ \bar{C} &= [C \quad \mathbf{0}_{n_y \times n_y}]. \end{aligned} \quad (4.23)$$

Given the augmented system in (4.22), the controller is designed using the Optimal Problem Solution detailed before, obtaining a control law of the form

$$\mathbf{u} = \mathbf{K}_{lqi}\mathbf{x}_{lqi} = [\mathbf{K}_{lqr} \quad \mathbf{K}_i] \begin{bmatrix} \mathbf{x} \\ \mathbf{x}_i \end{bmatrix}, \quad (4.24)$$

where  $\mathbf{K}_{lqr}$  and  $\mathbf{K}_i$  are submatrices which correspond to the feedback gain matrices that multiply  $\mathbf{x}$  and  $\mathbf{x}_i$  respectively, as shown in Fig. 4.1.

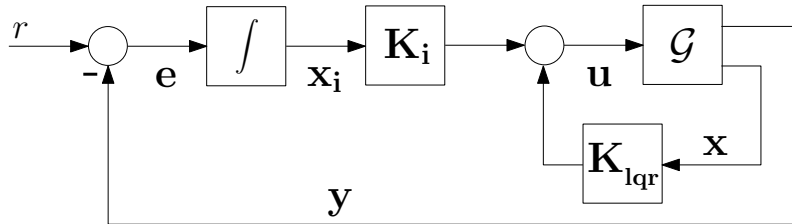


Figure 4.1: Closed-loop system with LQI controller for reference tracking

### 4.2.2 $H_\infty$ Controller

#### $H_\infty$ Synthesis for Controller Design

The design of the  $H_\infty$  controller is based on a representation of the closed-loop system including the generalized plant  $P_H$  and the controller  $K_H$ , shown in Fig. 4.2.

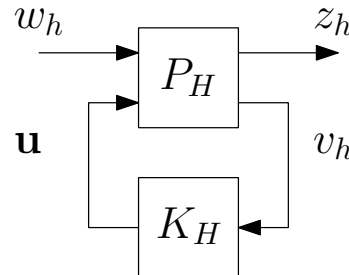


Figure 4.2: Control loop with generalized plant

The generalized plant  $P_H$  corresponds to the system

$$\begin{aligned} \dot{\mathbf{x}} &= A\mathbf{x} + B_w w_h + B\mathbf{u}, \\ z_h &= C_z \mathbf{x} + D_{zw} w_h + D_{zu} \mathbf{u}, \\ v_h &= -C \mathbf{x} + D_{vw} w_h + D_{vu} \mathbf{u}. \end{aligned} \quad (4.25)$$

where  $w_h$  are the external inputs, including command inputs, disturbances and noises;  $z_h$  is a fictitious output vector used to express design specifications; and  $v_h$  are the measured outputs of the system [74].

The  $H_\infty$  design procedure aims to synthesize a dynamic controller  $K_H$ , with input  $v_h = -\mathbf{y}$  and output  $\mathbf{u}$ , such that the closed-loop system is stabilized and the fictitious output  $z_h$  is minimized.

The system in Fig. 4.2, is rearranged for easy interpretation, in the way of Fig. 4.3.

In Fig. 4.3,  $\mathcal{G}$  represents the quadrotor dynamics;  $K_H$  the controller;  $r$  is the system reference;  $\mathbf{e}$  is the error;  $\mathbf{u}$  is the control input;  $z_h = [Z_s \ Z_k]$ ; and  $W_s$ ,  $W_k$  are weighting filters that must satisfy

$$\gamma = \left\| \begin{bmatrix} W_s S \\ W_k K_H S \end{bmatrix} \right\|_\infty < 1, \quad (4.26)$$

where  $S$  is the sensitivity function and  $K_H S$  is the control sensitivity defined as

$$S = (\mathcal{I} + \mathcal{G}K_H)^{-1}, \quad K_H S = K_H(\mathcal{I} + \mathcal{G}K_H)^{-1}. \quad (4.27)$$

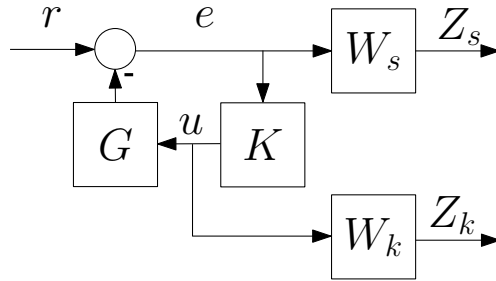


Figure 4.3: Generalized plant with the weighting filters  $W_s$  and  $W_k$ .

The  $H_\infty$  norm is defined only for proper and stable systems, so the weighting filters must satisfy that condition. The weighting filter  $W_s$  impose an upper bound on the sensitivity and is designed taking into account that it is desired to have integral action in the closed-loop. This ensures a zero steady-state error. On the other hand, the filter  $W_k$  impose an upper bound on the control sensitivity and must have a high-pass behaviour.

The weighting filters for the sensitivity and the control sensitivity are chosen as

$$\begin{aligned} W_s &= \frac{w_s/M_s}{s + w_s} * \mathcal{I}_{n_y \times n_y}, \\ W_k &= \frac{c_k}{M_k} \frac{s + w_k}{s + c_k w_k} * \mathcal{I}_{n_u \times n_u}, \end{aligned} \quad (4.28)$$

where  $M_s$  is small constant that sets an upper bound on the sensitivity at low frequencies; and  $w_s$  is a small constant that ensures that  $W_s$  does not have a pole at the origin;  $M_k$  is a constant that sets the upper bound on the control sensitivity at low frequencies;  $w_k$  is a small constant that place the zero of  $W_k$  near the origin; and  $c_k$  is a large constant that place the pole of  $W_k$  at a frequency above the bandwidth.

If the resulting value of  $\gamma$  is greater than one, the design procedure is iterated normalizing the weighting filters with  $\gamma$ .

In this project, the synthesized optimal  $H_\infty$  controllers  $K_H$  are computed using the Robust Control Toolbox of MATLAB.

### $H_\infty$ Controller Order Reduction

The designed  $H_\infty$  controller  $K_H$  is a dynamic model with  $n_u$  outputs,  $n_y$  inputs and order  $n_H = n_x + n_y + n_u$ . To reduce the computational load that the execution of a high-order dynamic system entails, it is necessary to find a reduced order controller that behaves similarly to the full order controller  $K_H$ .

In a dynamic system, the states with small singular value energy in  $\mathcal{W}_c$  show a weak response to a control input, while states with small singular value energy in  $\mathcal{W}_o$  have weak influence on the observed output. In order to check which states of  $K_H$  have little influence both in terms of controllability and observability, the singular values of the Hankel matrix

$$H_k = \mathcal{O}_{\mathcal{K}_H} \mathcal{C}_{\mathcal{K}_H}, \quad (4.29)$$

are analysed. The matrices  $\mathcal{C}_{\mathcal{K}_H}$  and  $\mathcal{O}_{\mathcal{K}_H}$  represent the controllability and observability matrices of the system  $K_H$ , respectively. A Hankel singular value (HSV) with small energy indicates that a state has little influence both in terms of controllability and observability.

If  $\hat{K}_H = (\hat{A}_H, \hat{B}_H, \hat{C}_H, \hat{D}_H)$  is the balanced realization of  $K_H$  with  $n_H$  state variables, and we have  $n_h$  significant states, so the last  $n_H - n_h$  HSVs are small enough to be neglected without modifying the system dynamics [78].

## 4.3 Controllers Design and Simulation

This section shows the specific design for the LQI and  $H_\infty$  controllers in each of the quadrotor flight modes. Based on what is described on Section 4.2, the dynamic model for each flight mode is set. Then, the controllers are designed and simulated in order to check their proper operation.

### 4.3.1 Stabilize Mode

In stabilize mode, the dynamics related to the position of the quadrotor are neglected. Thus, the only *DoF* that are automatically controlled are  $\psi$ ,  $\theta$ , and  $\phi$ .

#### Dynamic Model

The dynamic model exposed in 2.3, is reduced to a sixth order dynamic system ( $n_x = 6$ ) with three outputs ( $n_y = 3$ ), where

$$\begin{aligned} \mathbf{x} &= [\psi \quad \dot{\psi} \quad \theta \quad \dot{\theta} \quad \phi \quad \dot{\phi}]^T, \\ \mathbf{y} &= [\psi \quad \theta \quad \phi]^T. \end{aligned} \quad (4.30)$$

The linear state-space representation (4.3) for the dynamics related to the stabilize mode is defined by the matrices

$$\begin{aligned}
 A &= \begin{bmatrix} 0 & 1 & 0 & 0 & 0 & 0 \\ 0 & 0 & 0 & 0 & 0 & 0 \\ 0 & 0 & 0 & 1 & 0 & 0 \\ 0 & 0 & 0 & 0 & 0 & 0 \\ 0 & 0 & 0 & 0 & 0 & 1 \\ 0 & 0 & 0 & 0 & 0 & 0 \end{bmatrix}, \\
 B &= \begin{bmatrix} 0 & 0 & 0 & 0 & 0 & 0 \\ 0 & \frac{1}{J_{zz}} & 0 & 0 & 0 & 0 \\ 0 & 0 & 0 & \frac{1}{J_{yy}} & 0 & 0 \\ 0 & 0 & 0 & 0 & 0 & \frac{1}{J_{xx}} \end{bmatrix}^T, \\
 C &= \begin{bmatrix} 1 & 0 & 0 & 0 & 0 & 0 \\ 0 & 0 & 1 & 0 & 0 & 0 \\ 0 & 0 & 0 & 0 & 1 & 0 \end{bmatrix}, \\
 D &= \mathbf{0}_{3 \times 4}.
 \end{aligned} \tag{4.31}$$

Both the controllability matrix  $\mathcal{C}_G$  and observability matrix  $\mathcal{O}_G$ , have full rank ( $\text{rank}(\mathcal{C}_G) = \text{rank}(\mathcal{O}_G) = 6$ ), and therefore the system is controllable and observable.

### LQI Controller

The design of the LQI controller is done using the penalization matrices  $\mathcal{Q}$  and  $\mathcal{R}$ , that modify the cost function (4.8). Both matrices are set as diagonal matrices, so that there is only one parameter in the matrix affecting each state or input. The matrix  $\mathcal{Q}$  must be a  $9 \times 9$  matrix, since the size of  $\mathbf{x}_{\text{lqi}}$  is  $n_x + n_y$ . Similarly,  $\mathcal{R}$  must have four components in its diagonal, inasmuch as the number of inputs  $n_u$  remains four. In [52], the author suggests the matrices

$$\begin{aligned}
 \mathcal{Q} &= \mathcal{I}_{9 \times 9} [1 \ 0.1 \ 1 \ 0.1 \ 1 \ 0.1 \ 10 \ 40 \ 40]^T, \\
 \mathcal{R} &= \mathcal{I}_{4 \times 4} [3 \ 3 \ 3 \ 3]^T,
 \end{aligned} \tag{4.32}$$

where the system outputs  $\mathbf{y}$  have greater penalty than their derivatives  $(\dot{\psi}, \dot{\theta}, \dot{\phi})$ ;  $\mathbf{x}_{\text{lqi}}$  have greater penalties than  $\mathbf{x}$ ; and the input vector  $\mathbf{u}$  is slightly more penalized

than  $\mathbf{x}$ . If the penalty of  $\mathbf{x}_{\text{lqi}}$  is small, the response of the system will tend to be slow. On the other hand, if the penalty of  $\mathbf{x}_{\text{lqi}}$  is very high, the controller will over-compensate the system.

Based on the penalization matrices from (4.32), the feedback gain matrix  $\mathbf{K}_{\text{lqi}}$  is calculated. The closed-loop response of the system shown in Fig. 4.1 is simulated using MATLAB, and is shown in Fig. 4.4.

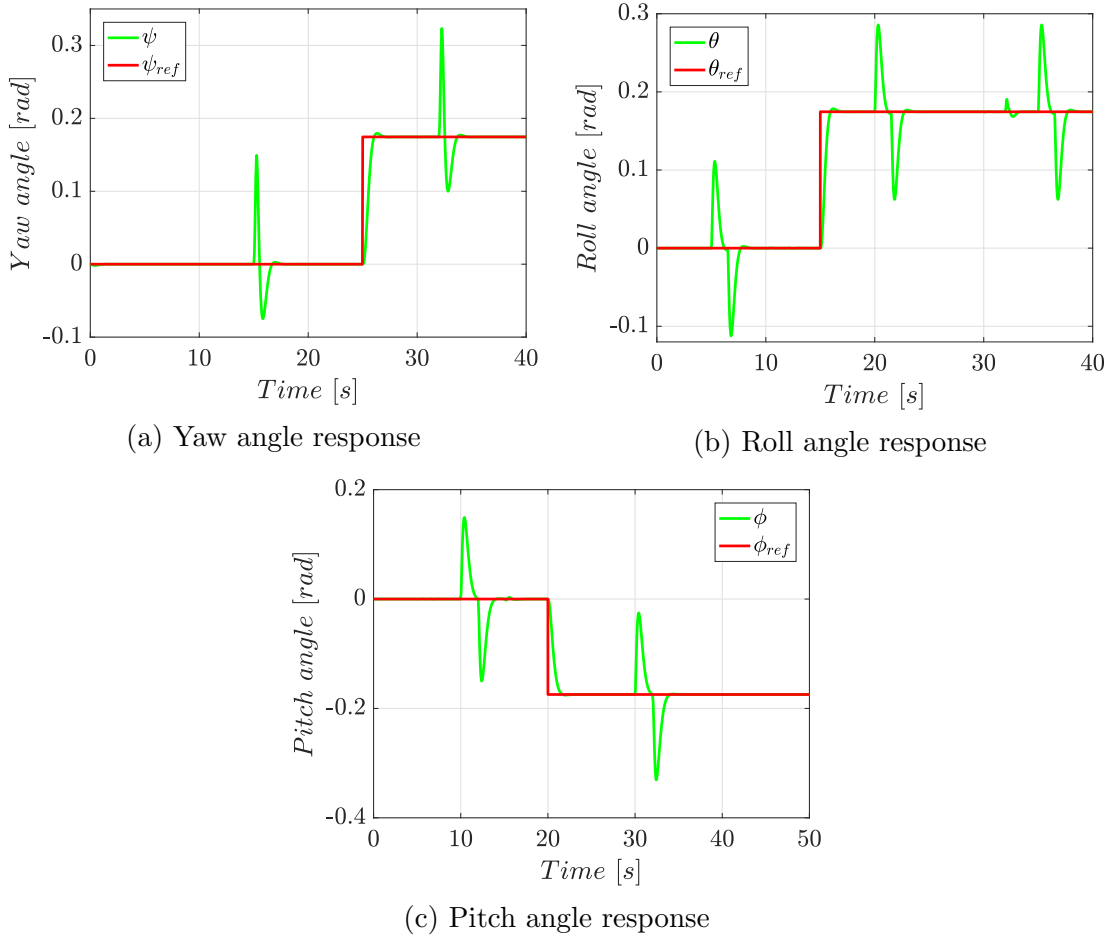


Figure 4.4: Closed-loop response of stabilize mode controlled by a LQI controller

Here, the system shows responses with a setting time of less than 1.5 s and overshoot of less than 5 %.

### $H_\infty$ Controller

The design of the  $H_\infty$  controller is based on the weighting filters  $W_s$  and  $W_k$ , which are set so that (4.26) is satisfied.

In the case of the stabilize mode, the filters are set as

$$\begin{aligned} W_s &= \frac{(22 \cdot 10^{-7})/(10^{-4})}{s + (22 \cdot 10^{-7})} * \mathcal{I}_{3 \times 3}, \\ W_k &= \frac{10^3}{20} \frac{s + 50}{s + (10^3 \cdot 50)} * \mathcal{I}_{4 \times 4}, \end{aligned} \quad (4.33)$$

with which  $\gamma = 0.0150$  was obtained. Since the  $\gamma$  value is very far from 1, the filters are normalized with  $\gamma$  as

$$\begin{aligned} W_s &= \frac{1}{\gamma} W_s, \\ W_k &= \frac{1}{\gamma} W_k, \end{aligned} \quad (4.34)$$

after which  $\gamma$  is recalculated, obtaining a value of  $\gamma = 0.8542$ . The filters  $W_s$  and  $W_k$  effectively set an upper bound for sensitivity  $S$  and the control sensitivity  $K_H S$ , as shown in Fig. 4.5.

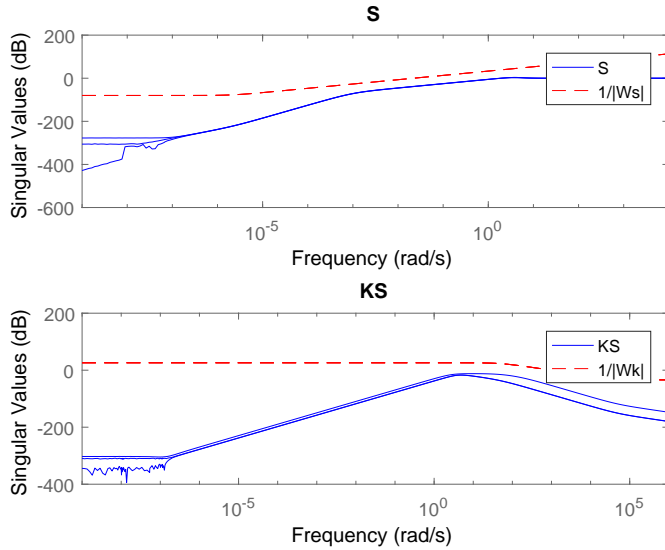


Figure 4.5: Upper bounded singular values of  $S$  and  $K_H S$  in stabilize mode

The computed dynamic controller  $K_H$  is a 13<sup>th</sup> order system. However, it is possible to find an equivalent system of lower order as seen in Section 4.2. The energy of the HSV of  $K_H$ , is shown in Fig. 4.6.

As shown in Fig. 4.6, the last ordered state of the balanced realization of  $K_H$ ,

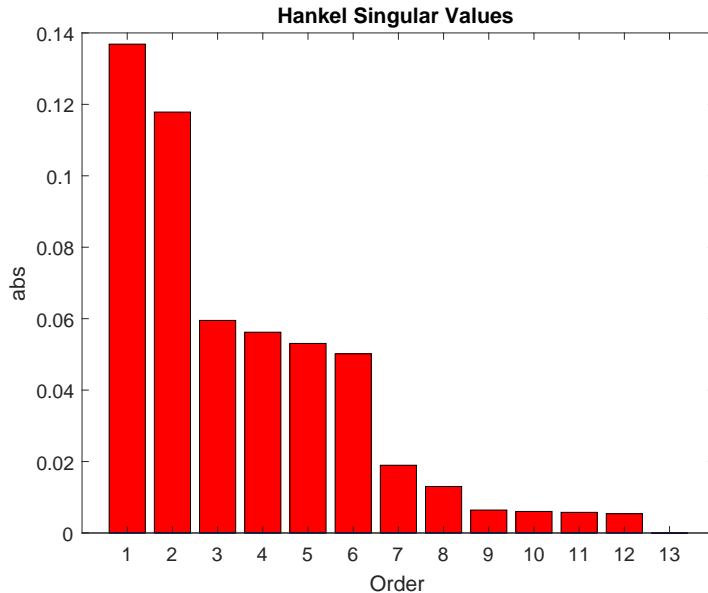


Figure 4.6: HSV energy histogram of  $K_H$  in stabilize mode

has unnoticeable energy when it is plotted; that means that this state can be truncated from the controller without modifying its dynamics. Thus, the reduced order controller  $K_H^*$  is a 12<sup>th</sup> order system.

Once, the optimal  $H_\infty$  controller  $K_H^*$  is synthesized using MATLAB, its performance is simulated. For the simulation, the system is subjected to the same disturbances and reference changes set in the LQI simulation. The simulation response is shown in Fig. 4.7.

For the  $H_\infty$  controller designed for the quadrotor stabilize mode, the closed-loop performance is improved when compared to the LQI controller. The designed  $K_H^*$  controller achieves to get responses with less than 1.1 s of setting time and 3 % overshoot.

### 4.3.2 Altitude Hold Mode

This mode adds the flight altitude of the quadrotor, represented by the variable  $z$ , to the quadrotor controlled *DoF*. Hence, it neglects the dynamics related to the  $x$  and  $y$  position.

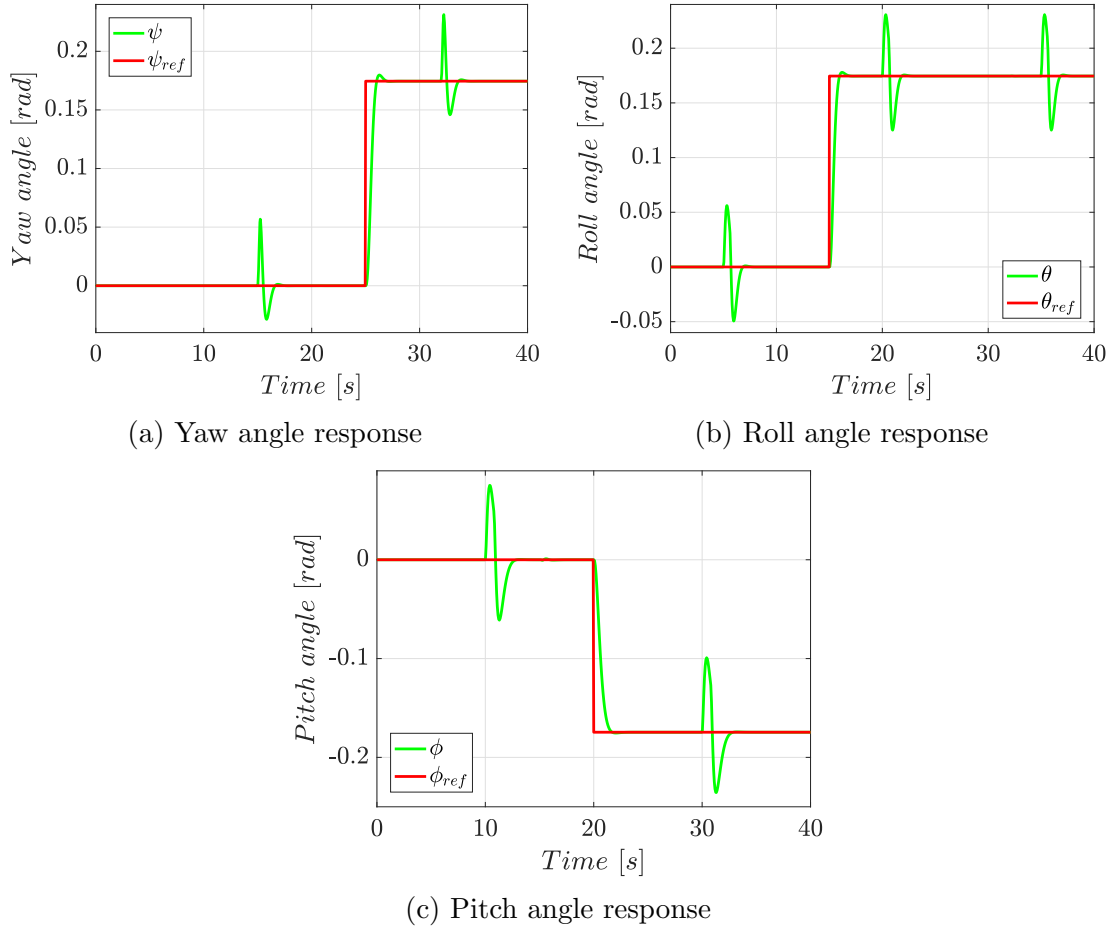


Figure 4.7: Closed-loop response of stabilize mode controlled by a  $H_\infty$  controller

## Dynamic Model

The altitude hold mode, is represented by a dynamic model of 8<sup>th</sup> order, which states and outputs vectors are

$$\mathbf{x} = [z \ \dot{z} \ \psi \ \dot{\psi} \ \theta \ \dot{\theta} \ \phi \ \dot{\phi}]^T, \quad (4.35)$$

$$\mathbf{y} = [z \ \psi \ \theta \ \phi]^T.$$

This dynamic system, is represented by the matrices

$$\begin{aligned}
 A &= \begin{bmatrix} 0 & 1 & 0 & 0 & 0 & 0 & 0 & 0 \\ 0 & 0 & 0 & 0 & 0 & 0 & 0 & 0 \\ 0 & 0 & 0 & 1 & 0 & 0 & 0 & 0 \\ 0 & 0 & 0 & 0 & 0 & 0 & 0 & 0 \\ 0 & 0 & 0 & 0 & 0 & 1 & 0 & 0 \\ 0 & 0 & 0 & 0 & 0 & 0 & 0 & 0 \\ 0 & 0 & 0 & 0 & 0 & 0 & 0 & 1 \\ 0 & 0 & 0 & 0 & 0 & 0 & 0 & 0 \end{bmatrix}, \\
 B &= \begin{bmatrix} 0 & \frac{1}{m} & 0 & 0 & 0 & 0 & 0 & 0 \\ 0 & 0 & 0 & \frac{1}{J_{zz}} & 0 & 0 & 0 & 0 \\ 0 & 0 & 0 & 0 & 0 & \frac{1}{J_{yy}} & 0 & 0 \\ 0 & 0 & 0 & 0 & 0 & 0 & 0 & \frac{1}{J_{xx}} \end{bmatrix}^T, \\
 C &= \begin{bmatrix} 1 & 0 & 0 & 0 & 0 & 0 & 0 & 0 \\ 0 & 0 & 1 & 0 & 0 & 0 & 0 & 0 \\ 0 & 0 & 0 & 0 & 1 & 0 & 0 & 0 \\ 0 & 0 & 0 & 0 & 0 & 0 & 1 & 0 \end{bmatrix}, \\
 D &= \mathbf{0}_{4 \times 4}.
 \end{aligned} \tag{4.36}$$

The controllability and observability features of the system are checked using the matrices  $\mathcal{C}_G$  and  $\mathcal{O}_G$ . In the altitude hold dynamic model, both matrices have a rank of 8, which means that the system is controllable and observable.

### LQI Controller

For the altitude hold mode, the penalization matrices  $\mathcal{Q}$  and  $\mathcal{R}$  are set as

$$\begin{aligned}
 \mathcal{Q} &= \mathcal{I}_{12 \times 12} [1 \ 0.1 \ 1 \ 0.1 \ 1 \ 0.1 \ 1 \ 0.1 \ 10 \ 10 \ 40 \ 40]^T, \\
 \mathcal{R} &= \mathcal{I}_{4 \times 4} [3 \ 3 \ 3 \ 3]^T,
 \end{aligned} \tag{4.37}$$

so that the state  $z$  has the same penalization as the other outputs, while the penalization of the unmeasured states remains being lower. The integral error of the quadrotor elevation is penalized the same way as the error of yaw, with a not so big penalization, as the pitch and roll dynamics must be prioritized.

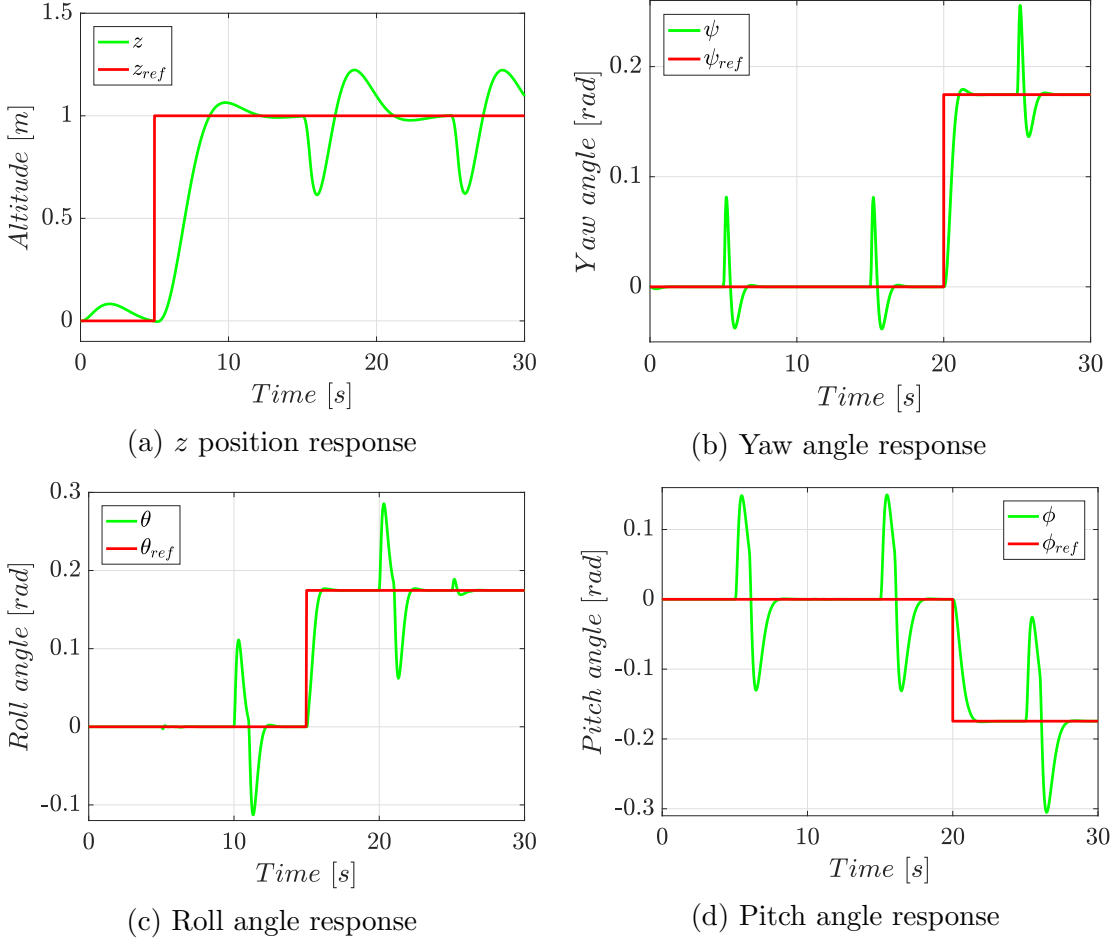


Figure 4.8: Closed-loop response of altitude hold mode controlled by a LQI controller

In Fig. 4.8, the closed-loop response of the system  $\mathcal{G}_k$  in altitude hold mode with LQI control, is shown. Here, the altitude has a response with a setting time of 11.5 s and an overshoot of 6 %. The attitude response remains the same as it is in the stabilize mode due to the use of the same penalties for the corresponding states and inputs.

### $H_\infty$ Controller

In altitude hold mode, the weighting filters which satisfy  $\gamma < 1$  are

$$\begin{aligned} W_s &= \frac{(10^{-4})/(10^{-4})}{s + (10^{-4})} * \mathcal{I}_{4 \times 4}, \\ W_k &= \frac{10^3}{20} \frac{s + 20}{s + (10^3 \cdot 20)} * \mathcal{I}_{4 \times 4}. \end{aligned} \quad (4.38)$$

In this case,  $\gamma = 0.5976$ , forcing to iterate after normalizing the filters. After one iteration, the value of  $\gamma$  is 0.9939. The bounding of the  $S$  and  $K_H S$  functions, is shown in Fig. 4.9

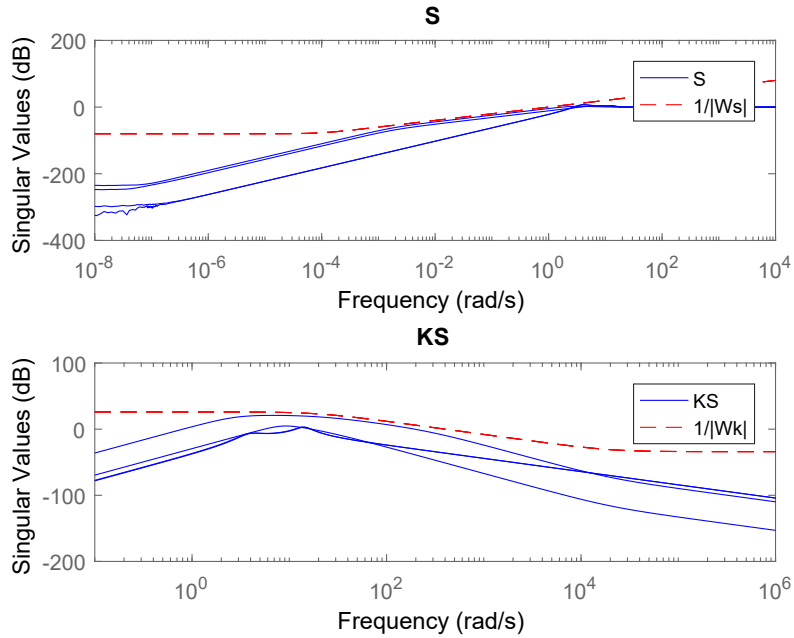


Figure 4.9: Upper bounded singular values of  $S$  and  $K_H S$  in altitude hold mode

As the dynamic model for altitude hold is a  $8^{th}$  order system with 4 inputs and 4 outputs, the resulting  $H_\infty$  controller is a  $16^{th}$  dynamic system.

The  $K_H$  HSV energy, exposed in Fig. 4.10, shows that there are 13 states of  $K_H$  which are influenced in terms of controllability and observability, and make up a minimal realization  $K_H^*$  of  $K_H$ .

The simulated response of the designed control system (Fig. 4.11), shows an improvement in setting time and overshoot when compared to the LQI controller response in the same mode. Using the  $H_\infty$  controller, the setting time for  $z$  is 10.7 s, while the overshoot is 4.5 %.

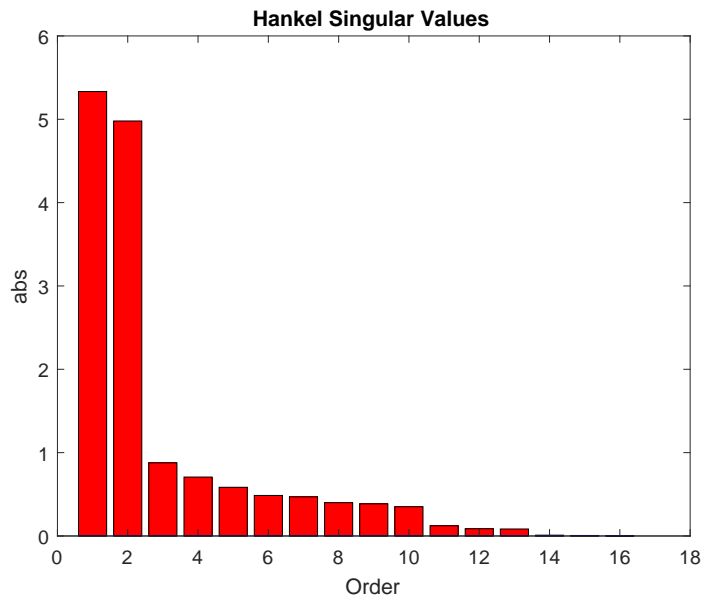


Figure 4.10: HSV energy histogram of  $K_H$  in altitude hold mode

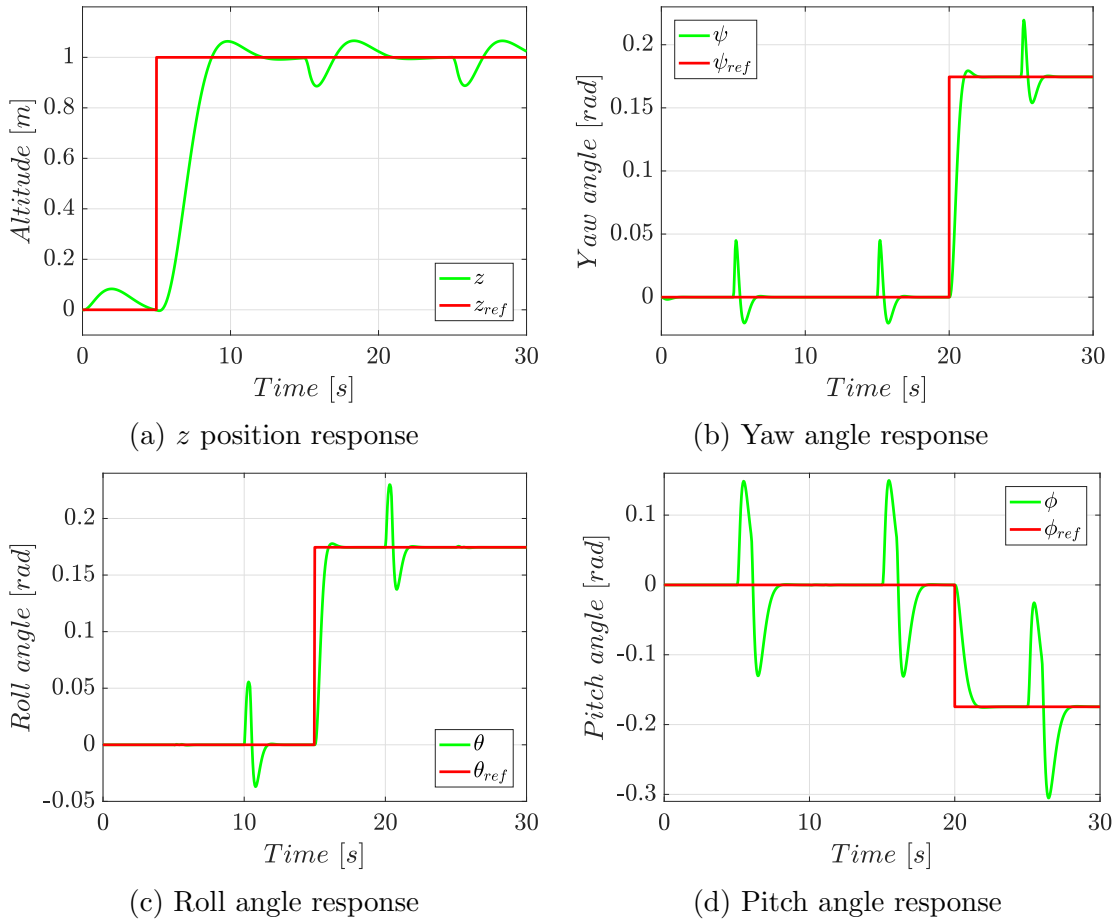


Figure 4.11: Closed-loop response of altitude hold mode controlled by a  $H_\infty$  controller

### 4.3.3 GNSS-Dependent Flight Modes

The GNSS-Dependent flight modes take into account the full states dynamics of the quadrotor. These modes include loiter, auto and RTL mode. The designed controllers can be used in any of the three mentioned modes.

## Dynamic Model

The dynamic model used for the design of controllers for the GNSS-Dependent flight modes, is the full 12<sup>th</sup> system introduced in Section 2.3 with all the measurable outputs available, where

$$\mathbf{x} = [x \ \dot{x} \ y \ \dot{y} \ z \ \dot{z} \ \psi \ \dot{\psi} \ \theta \ \dot{\theta} \ \phi \ \dot{\phi}]^T,$$

$$\mathbf{y} = [x \ y \ z \ \psi \ \theta \ \phi]^T,$$

$$B = \begin{bmatrix} 0 & 0 & 0 & 0 & 0 & \frac{1}{m} & 0 & 0 & 0 & 0 & 0 & 0 & 0 \\ 0 & 0 & 0 & 0 & 0 & 0 & 0 & \frac{1}{J_{zz}} & 0 & 0 & 0 & 0 & 0 \\ 0 & 0 & 0 & 0 & 0 & 0 & 0 & 0 & 0 & \frac{1}{J_{yy}} & 0 & 0 & 0 \\ 0 & 0 & 0 & 0 & 0 & 0 & 0 & 0 & 0 & 0 & 0 & \frac{1}{J_{xx}} & 0 \end{bmatrix}^T.$$

$$C = \begin{bmatrix} 1 & 0 & 0 & 0 & 0 & 0 & 0 & 0 & 0 & 0 & 0 & 0 \\ 0 & 0 & 1 & 0 & 0 & 0 & 0 & 0 & 0 & 0 & 0 & 0 \\ 0 & 0 & 0 & 0 & 1 & 0 & 0 & 0 & 0 & 0 & 0 & 0 \\ 0 & 0 & 0 & 0 & 0 & 0 & 1 & 0 & 0 & 0 & 0 & 0 \\ 0 & 0 & 0 & 0 & 0 & 0 & 0 & 0 & 1 & 0 & 0 & 0 \\ 0 & 0 & 0 & 0 & 0 & 0 & 0 & 0 & 0 & 0 & 1 & 0 \end{bmatrix}, \quad (4.40)$$

$$D = \mathbf{0}_{6 \times 4}.$$

Verifying the controllability and observability of the system using the matrices  $\mathcal{C}_G$  and  $\mathcal{O}_G$ , it is confirmed that these matrices have full-rank. Hence, the system is controllable and observable.

### LQI Controller

Similarly to the altitude hold mode, in the GNSS-Dependent modes, the penalization matrices are

$$\begin{aligned} \mathcal{Q} &= \mathcal{I}_{18 \times 18} [1 \ 0.1 \ 1 \ 0.1 \ 1 \ 0.1 \ 1 \ 0.1 \ 1 \ 0.1 \ 1 \ 0.1 \ 10 \ 10 \ 10 \ 10 \ 40 \ 40]^T, \\ \mathcal{R} &= \mathcal{I}_{4 \times 4} [3 \ 3 \ 3 \ 3]^T, \end{aligned} \quad (4.41)$$

where  $x$  and  $y$  have the same penalty as  $z$ , and analogously happens with  $\dot{x}$ ,  $\dot{y}$  and  $\dot{z}$ .

Using MATLAB, the quadrotor controlled by the designed LQI controller, is simulated. In this simulation, the quadrotor is commanded automatically through some waypoints, which describe a square figure with constant flight altitude.

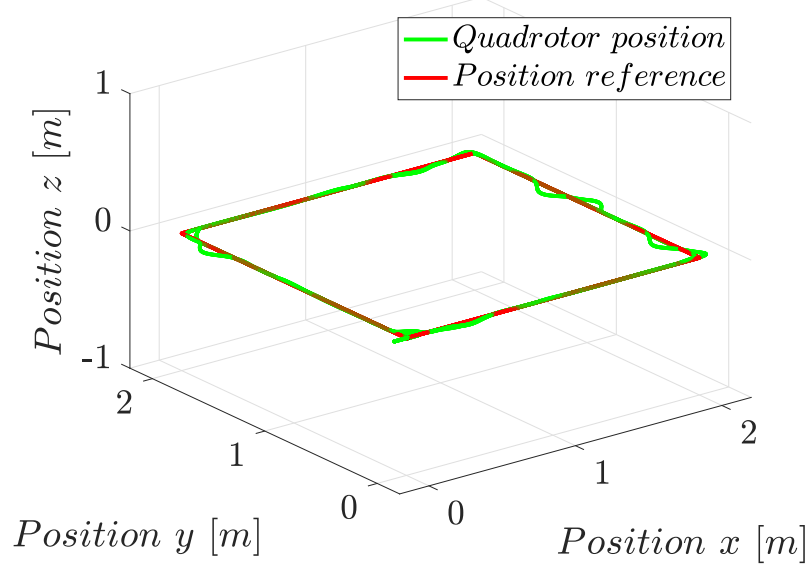


Figure 4.12: Position response of the GNSS-Dependent modes with a LQI controller

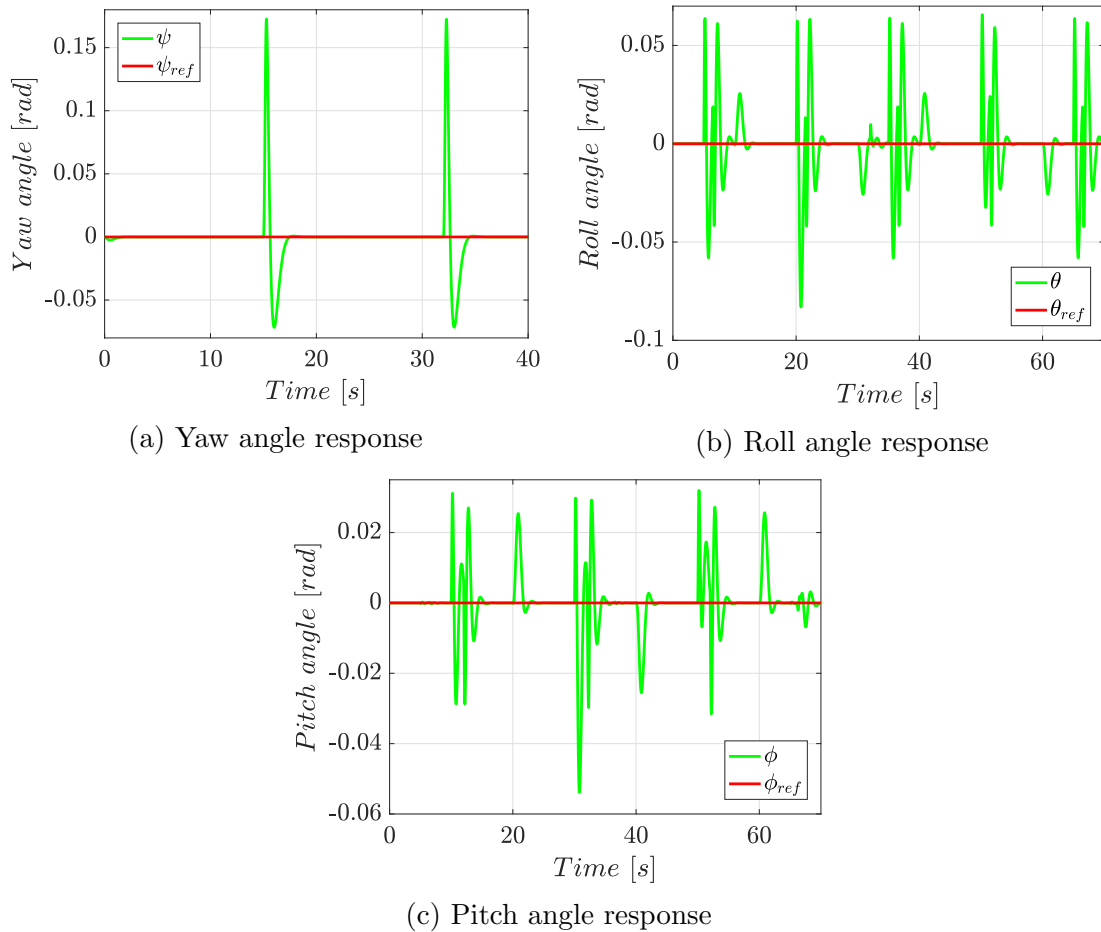


Figure 4.13: Attitude response of the GNSS-Dependent modes with a LQI controller

As can be seen in Fig. 4.12, the quadrotor is capable of following the desired trajectory while being controlled by the LQI controller in a GNSS-Dependent mode. In addition, the quadrotor manages to recover its track in less than 3.5 s, after suffer the actions of disturbances that periodically simulate the force of the wind.

### $H_\infty$ Controller

For the GNSS-Dependent flight modes, the weighting filter  $W_s$  is now a  $6 \times 6$ -matrix due to the existence of six output signals in  $\mathbf{y}$ . Thus, the weighting filters are set as

$$\begin{aligned} W_s &= \frac{(10^{-4})/(10^{-4})}{s + (10^{-4})} * \mathcal{I}_{6 \times 6}, \\ W_k &= \frac{10^4}{20} \frac{s + 30}{s + (10^4 \cdot 30)} * \mathcal{I}_{4 \times 4}. \end{aligned} \quad (4.42)$$

With these weighting filters,  $\gamma = 0.5976$ . After one iteration, with normalized weighting filters, the  $\gamma$  value becomes equal to 0.999. Thus, the sensitivity and control sensitivity functions are closely upper bounded by the weighting filters, as shown in Fig. 4.14.

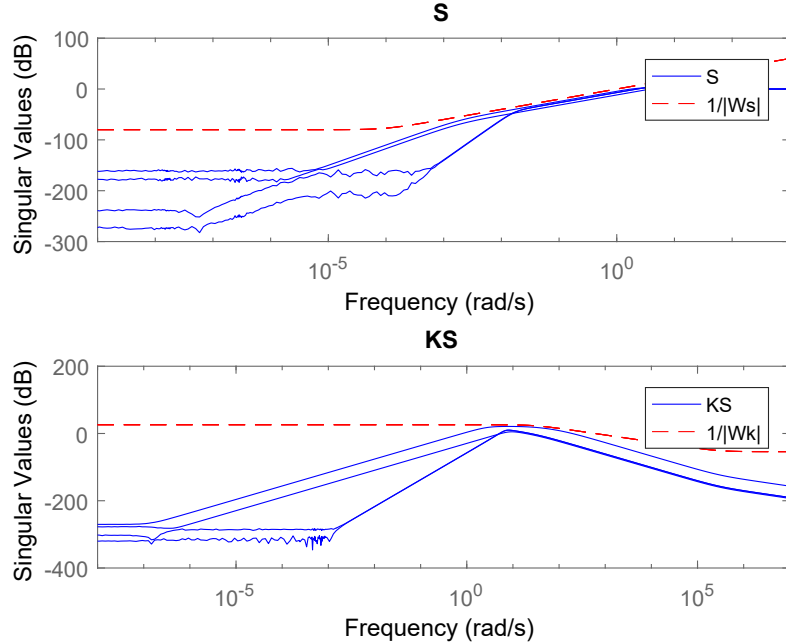


Figure 4.14: Upper bounded singular values of  $S$  and  $K_H S$  in GNSS-Dependent modes

The synthesized  $H_\infty$  controller  $K_H$  for the GNSS-Dependent modes has 20 states.

An equivalent controller  $K_H^*$  of lower order is found, using the HSV energy shown in Fig. 5.2.

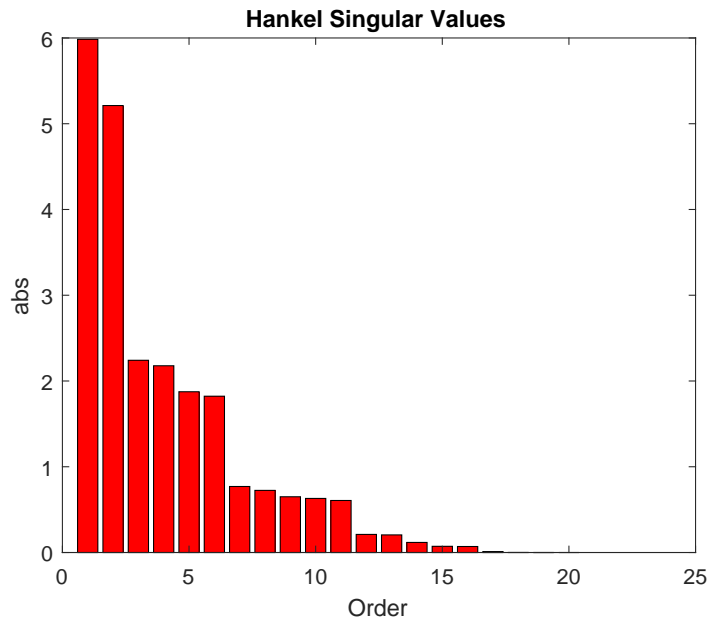


Figure 4.15: HSV energy histogram of  $K_H$  in GNSS-Dependent modes

The system  $K_H$  has four unnoticeable states in terms of controllability and observability, as seen in Fig. 5.2. Therefore, the reduced order controller  $K_H^*$  is the subsystem of  $K_H$  which includes just the 16 noticeable states.

The simulation of the designed  $H_\infty$  controller with the quadrotor non-linear dynamics, is also developed using a reference of waypoints describing a square with sides of 2 m, and a constant elevation.

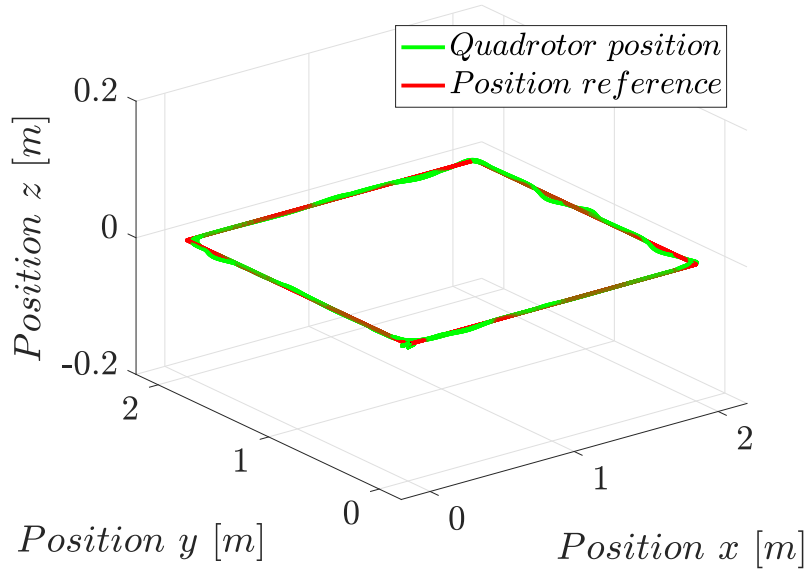


Figure 4.16: Position response of the GNSS-Dependent modes with a  $H_\infty$  controller

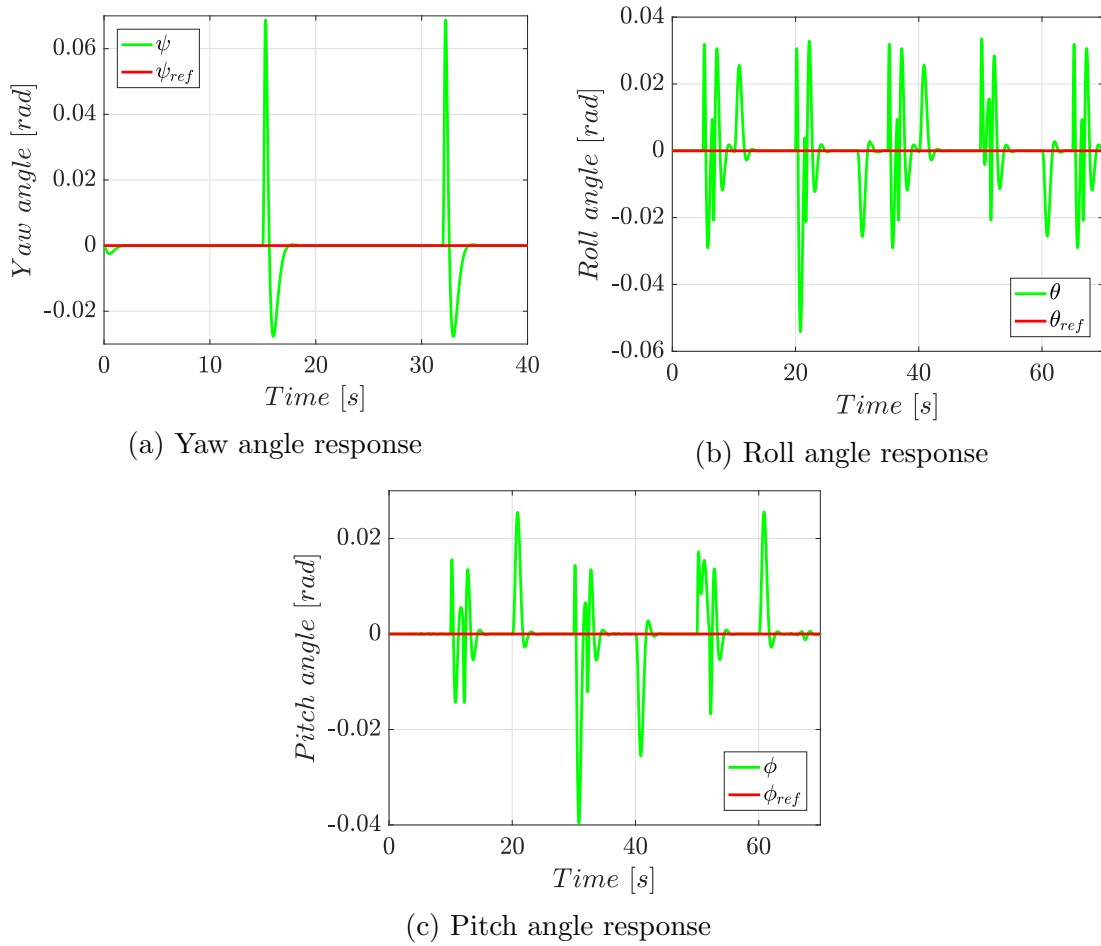


Figure 4.17: Attitude response of the GNSS-Dependent modes with a  $H_\infty$  controller

The simulated control system manages to follow the position reference, despite being affected by disturbances, as seen in Fig. 4.16. For disturbances, it shows a setting time of 2.8 s.

## 4.4 State Estimation Through Kalman Filter

The quadrotor dynamics are sensed exclusively using the on-board smartphone sensors. These sensors have different sample frequencies and poor accuracy. On the other hand, the LQI controller needs a full-state feedback, but it is not possible to get reliable measurements of all the components in  $\mathbf{x}$  in a smartphone. Hence, it is necessary to use estimation algorithms, as a Kalman filter. The principle of separation allows the design of controllers and state estimators independently.

### 4.4.1 Attitude Estimation

The Android API implements a Kalman filter for attitude estimation using the raw data delivered by the smartphone accelerometer, gyroscope and magnetometer, as exposed in [79]. Using the quaternion  $Q_s$  delivered by the Rotation virtual sensor included in the Android SDK, it is obtained an absolute orientation representation with respect to the Earth frame [80], with

$$Q_s = e^{(\alpha/2)(u\vec{i} + v\vec{j} + w\vec{k})} \\ = \begin{bmatrix} \kappa_0 \sin(\alpha/2) \\ \kappa_1 \sin(\alpha/2) \\ \kappa_2 \sin(\alpha/2) \\ \cos(\alpha/2) \end{bmatrix} = \begin{bmatrix} q_0 \\ q_1 \\ q_2 \\ q_3 \end{bmatrix} \quad (4.43)$$

where  $\alpha$  is the amount of degrees the quaternion is rotated around the axis  $\kappa_0 \vec{i} + \kappa_1 \vec{j} + \kappa_2 \vec{k}$ . The rotation matrix  $\mathbf{R}_b^w$  can be defined using  $Q_s$  as

$$\mathbf{R}_b^w = \begin{bmatrix} 1 - 2(q_2^2 + q_3^2) & 2(q_1q_2 - q_0q_3) & 2(q_0q_2 + q_1q_3) \\ 2(q_1q_2 - q_0q_3) & 1 - 2(q_1^2 + q_3^2) & 2(q_2q_3 + q_0q_1) \\ 2(q_1q_3 + q_0q_2) & 2(q_0q_1 + q_2q_3) & 1 - 2(q_1^2 + q_2^2) \end{bmatrix}. \quad (4.44)$$

Comparing (2.19) and (4.44), the Euler angles  $(\psi_m, \theta_m, \phi_m)$  are then obtained from the quaternion  $Q_s$  as

$$\begin{bmatrix} \psi_m \\ \theta_m \\ \phi_m \end{bmatrix} = \begin{bmatrix} \text{atan2}(2(q_3q_2 + q_0q_1), 1 - 2(q_1^2 + q_2^2)) \\ \arcsin(2(q_3q_1 - q_2q_0)) \\ \text{atan2}(2(q_3q_0 + q_1q_2), 1 - 2(q_0^2 + q_1^2)) \end{bmatrix}. \quad (4.45)$$

#### 4.4.2 Position Measurement

The smartphone used in this project, can measure its position with respect to the Earth-frame. For this task, it counts with a GNSS receiver and a barometer. The  $x_m$  and  $y_m$  position measurements, with respect to the  $X_W$  and  $Y_W$  axes, are acquired using the GNSS receiver.

Each coordinates sample is initially set in an ellipsoidal representation of decimal degrees, following the WGS84 coordinate system. Then, the coordinates are converted to a bi-dimensional representation in meter units using the cartographic projection Magna-Sirgas (projection EPSG:3115).

The altitude measurements  $z_m$  are acquired using the barometric pressure sensor which delivers the pressure value  $p_k$  in hPa units. This signal is converted to meters as

$$z_m = 44330 \left( 1 - \frac{p_k}{p_0}^{1/5.255} \right) [m], \quad (4.46)$$

where  $p_0$  is the atmospheric pressure at sea level [81].

The smartphone GNSS receiver and barometer were tested statically, leaving the phone in a stable position for 100 minutes, with an ambient temperature of 22 °C and a UV index of 3. The results of the test are shown in Fig. 4.18

As seen in Fig. 4.18a, even though the phone was kept in a static position, the  $x_m$  and  $y_m$  position signal received from the GNSS receiver shows a change of about 6 m in both the  $X_W$  and  $Y_W$  directions, after just 60 s. The  $z_m$  position, however, has sudden changes in short periods of time, but without reaching errors greater than 2.5 m. The attitude results, Fig. 4.18b, show stable signals for the three Euler angles. The  $\psi_m$  and  $\theta_m$  angles suffer from a drift of about 0.04 and  $-0.02 \text{ rad}$  respectively, while the initial drift suffered by  $\phi_m$  is just  $-0.01 \text{ rad}$ .

Despite being under a clear sky, where the smartphone could have visibility of more than six satellites of the GPS and GLONASS constellations, the GNSS accuracy value, delivered by the receiver in the smartphone, is always more than 9 m as seen in Fig. 4.18c.

#### 4.4.3 States Estimation

In order to estimate all the components of the state vector  $\mathbf{x}$ , a Kalman filter is designed. The Kalman filter is an iterative algorithm that estimates the observable

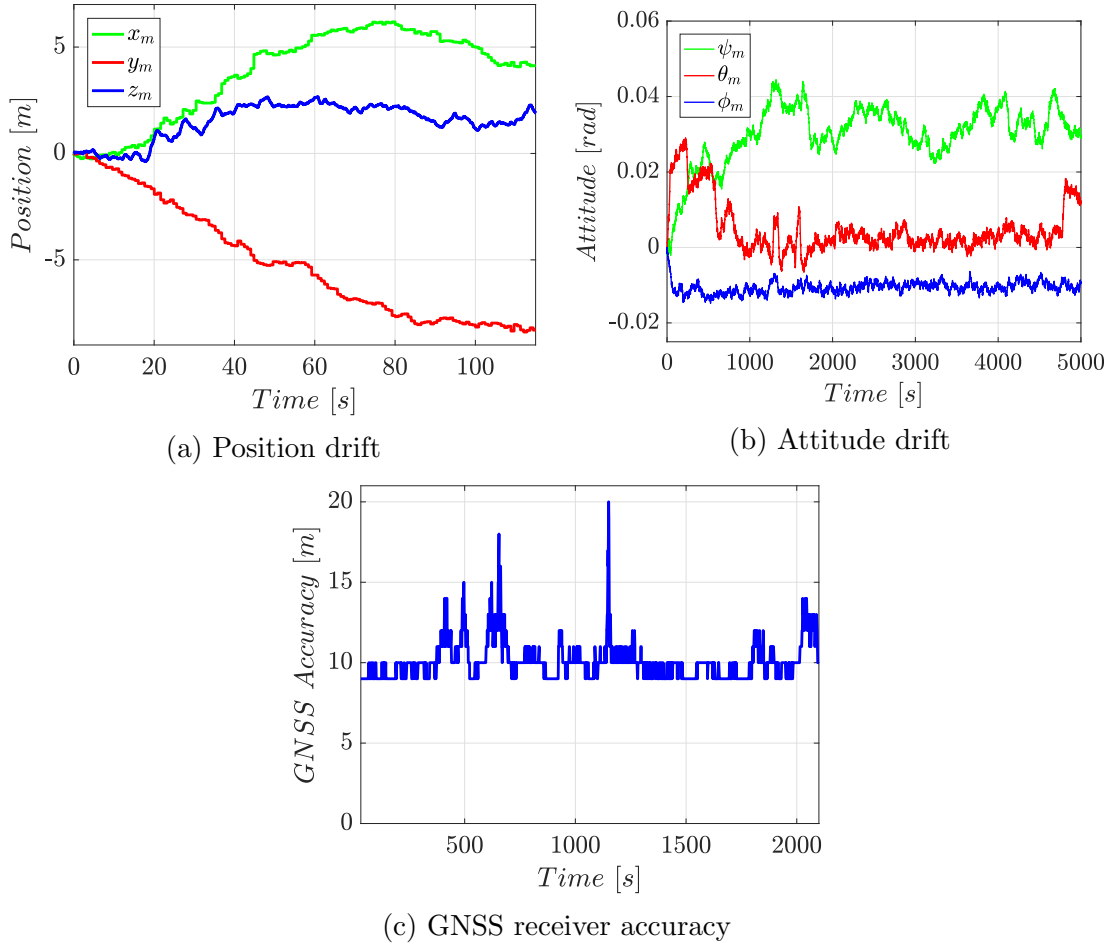


Figure 4.18: Static test of the smartphone GNSS receiver and barometer

(and not measurable) states of a system, using the measurable variables, the inputs and the variances of the noises that affect the system.

This filter is designed using the linearized dynamic model of the quadrotor from Section 2.3, where  $\mathbf{x} = [x \ \dot{x} \ y \ \dot{y} \ z \ \dot{z} \ \psi \ \dot{\psi} \ \theta \ \dot{\theta} \ \phi \ \dot{\phi}]^T$ , and using the discretized representation  $\mathcal{G}_k$ .

The algorithm starts calculating a prediction of the state  $\hat{\mathbf{x}}_k^-$  and its covariance  $P_k^-$  as

$$\hat{\mathbf{x}}_k^- = A_k \hat{\mathbf{x}}_{k-1} + B_k \mathbf{u}, \quad (4.47)$$

$$P_k^- = A_k P_{k-1} A_k^T + Q_k, \quad (4.48)$$

where  $\hat{\mathbf{x}}_{k-1} = \hat{\mathbf{x}}(k-1)$  is the previous estimated state,  $P_{k-1}$  the previous error covariance matrix and  $Q_k$  the process variance. The state prediction is then corrected

using the Kalman gain vector

$$K_k = P_k^- H^T (H P_k^- H^T + R_k)^{-1}, \quad (4.49)$$

and updating the state estimation  $\hat{\mathbf{x}}_k$  and its covariance  $P_k$ , based on the measurements  $\vartheta_k$  as

$$\begin{aligned} \hat{\mathbf{x}}_k &= \hat{\mathbf{x}}_k^- + K_k (\vartheta_k - H \hat{\mathbf{x}}_k^-), \\ P_k &= (\mathcal{I} - K_k H) P_k^-, \end{aligned} \quad (4.50)$$

where  $R_k$  is the measurement covariance matrix,  $\mathcal{I}$  is the identity matrix and  $H$  is the matrix that satisfies

$$\vartheta_k = H \mathbf{x}_k. \quad (4.51)$$

The measurements vector  $\vartheta_k$  is set as

$$\vartheta_k = [x_m \ y_m \ z_m \ \psi_m \ \theta_m \ \phi_m]^T, \quad (4.52)$$

so matrix  $H$  is defined as

$$H = \begin{bmatrix} 1 & 0 & 0 & 0 & 0 & 0 & 0 & 0 & 0 & 0 & 0 & 0 \\ 0 & 0 & 1 & 0 & 0 & 0 & 0 & 0 & 0 & 0 & 0 & 0 \\ 0 & 0 & 0 & 0 & 1 & 0 & 0 & 0 & 0 & 0 & 0 & 0 \\ 0 & 0 & 0 & 0 & 0 & 0 & 1 & 0 & 0 & 0 & 0 & 0 \\ 0 & 0 & 0 & 0 & 0 & 0 & 0 & 0 & 1 & 0 & 0 & 0 \\ 0 & 0 & 0 & 0 & 0 & 0 & 0 & 0 & 0 & 0 & 1 & 0 \end{bmatrix}. \quad (4.53)$$

This algorithm is executed once every sampling period, after which, the controller can use the vector of estimated states  $\hat{\mathbf{x}}_k$  as feedback.

## 4.5 Conclusions

The control and state estimation algorithms design procedure is presented in this chapter. The concepts of representation of a system as a state space model, controllability and observability, were introduced in the first part. Given the need to achieve trajectory tracking with the quadrotor, a LQR controller with integral feedback LQI is designed. This controller ensures zero steady-state error. Also, it is designed a controller based on the  $H_\infty$  synthesis. The performance of these controllers acting with the non-linear dynamic model of the quadrotor, is simulated. In simulations, the  $H_\infty$  controller showed a better performance when subjected to exactly the same disturbances and reference changes as the LQI controller. Finally, due to the principle of separation, a state estimator based on a Kalman filter is designed taking into account the accuracy of the smartphone measurements.

# Chapter 5

## Implementation and Results

rgrtgrtgrgtrgrrg

### 5.1 Android Application

sdfdsfdsfds

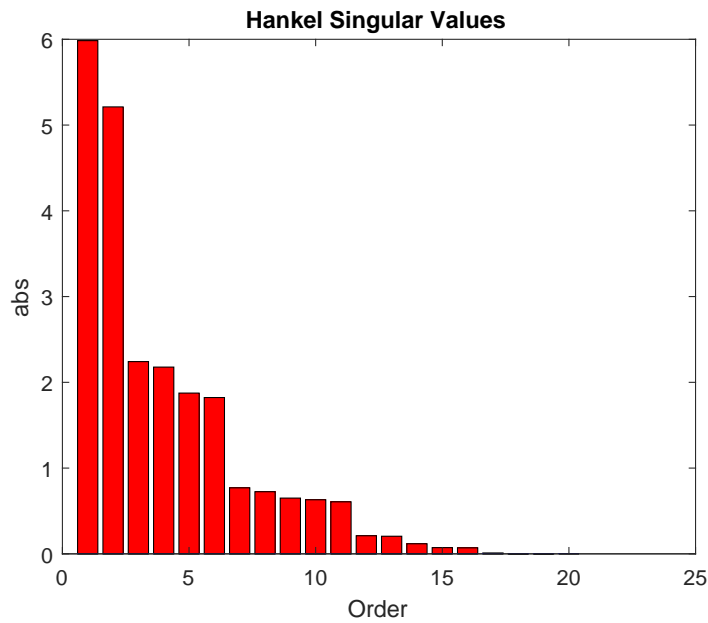


Figure 5.1: HSV energy histogram of  $K_H$  in GNSS-Dependent modes

## 5.2 Ground Control Station

sdfsdfdsd

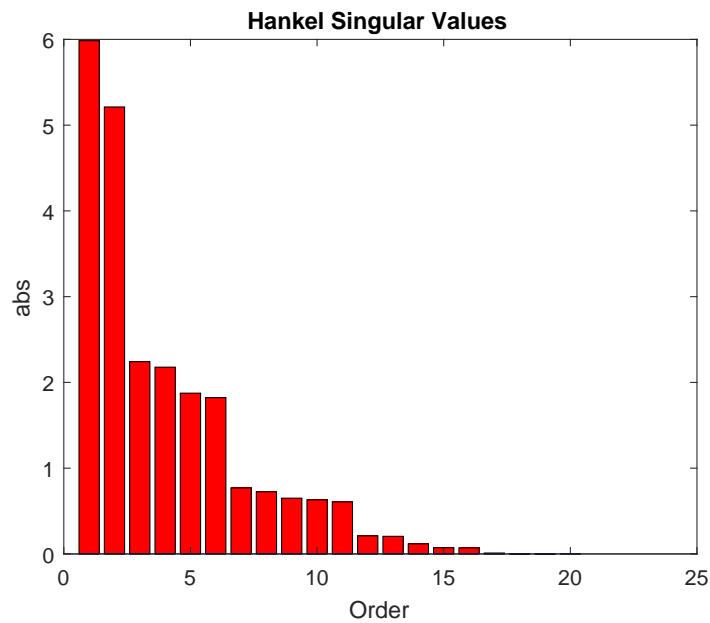


Figure 5.2: HSV energy histogram of  $K_H$  in GNSS-Dependent modes

## 5.3 Flight Tests

### 5.3.1 Stabilize Mode

LQI Controller

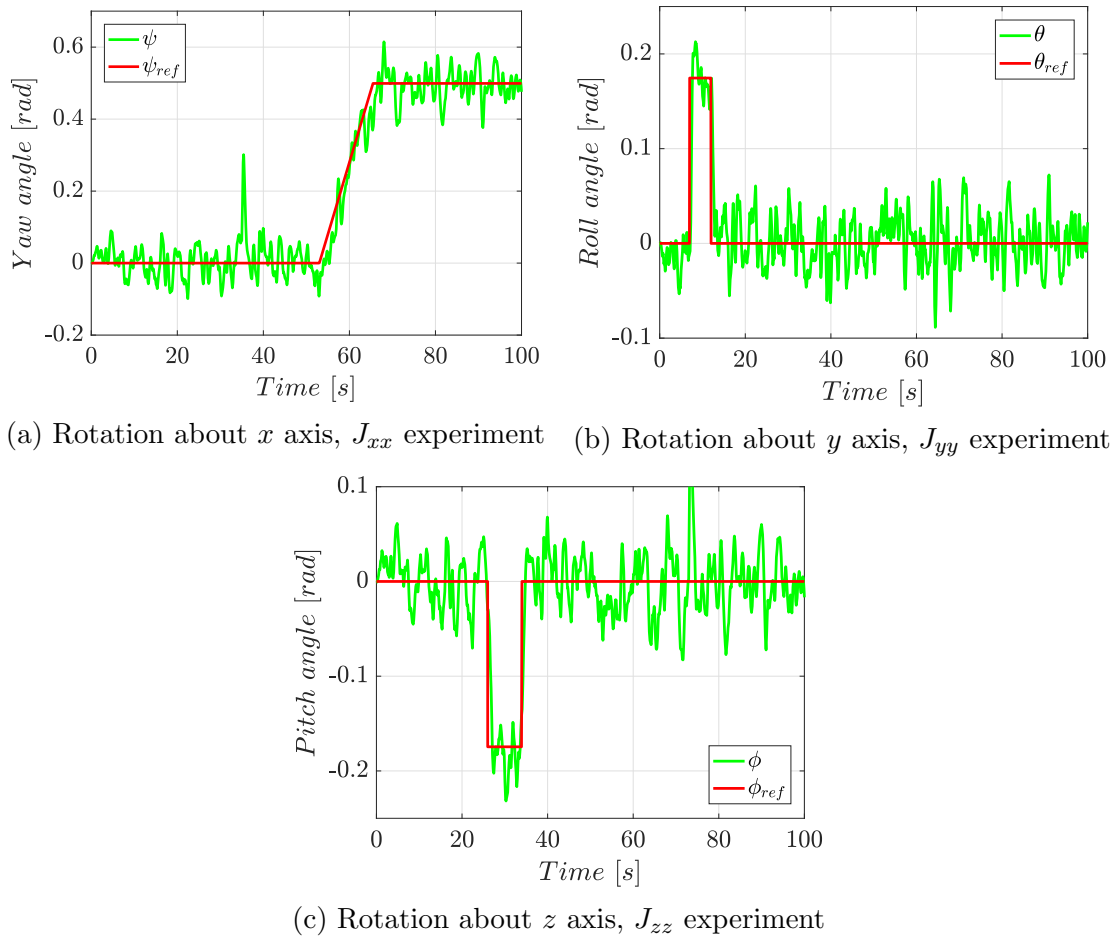


Figure 5.3: Rotation about  $x$ ,  $y$  and  $z$  axes during the bifilar pendulum experiments

### $H_\infty$ Controller

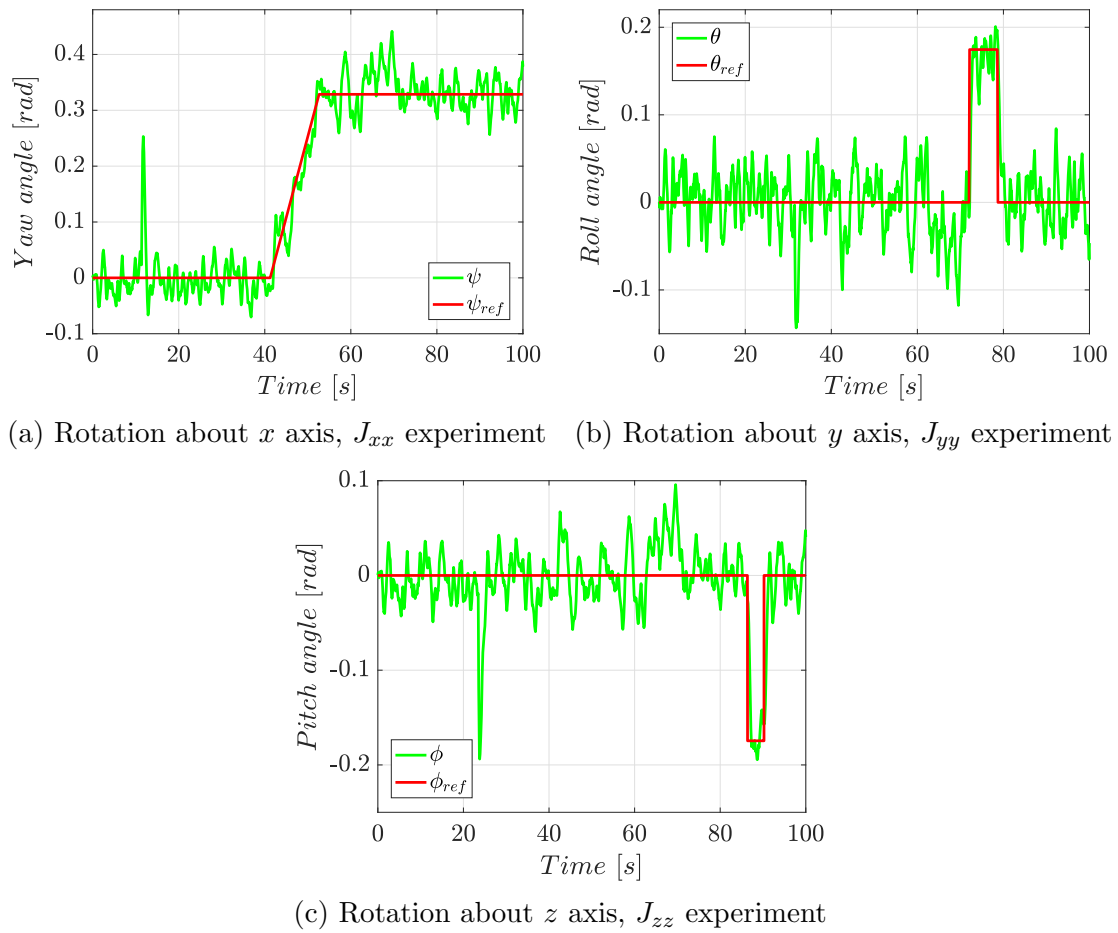


Figure 5.4: Rotation about  $x$ ,  $y$  and  $z$  axes during the bifilar pendulum experiments

### 5.3.2 Altitude Hold Mode

#### LQI Controller

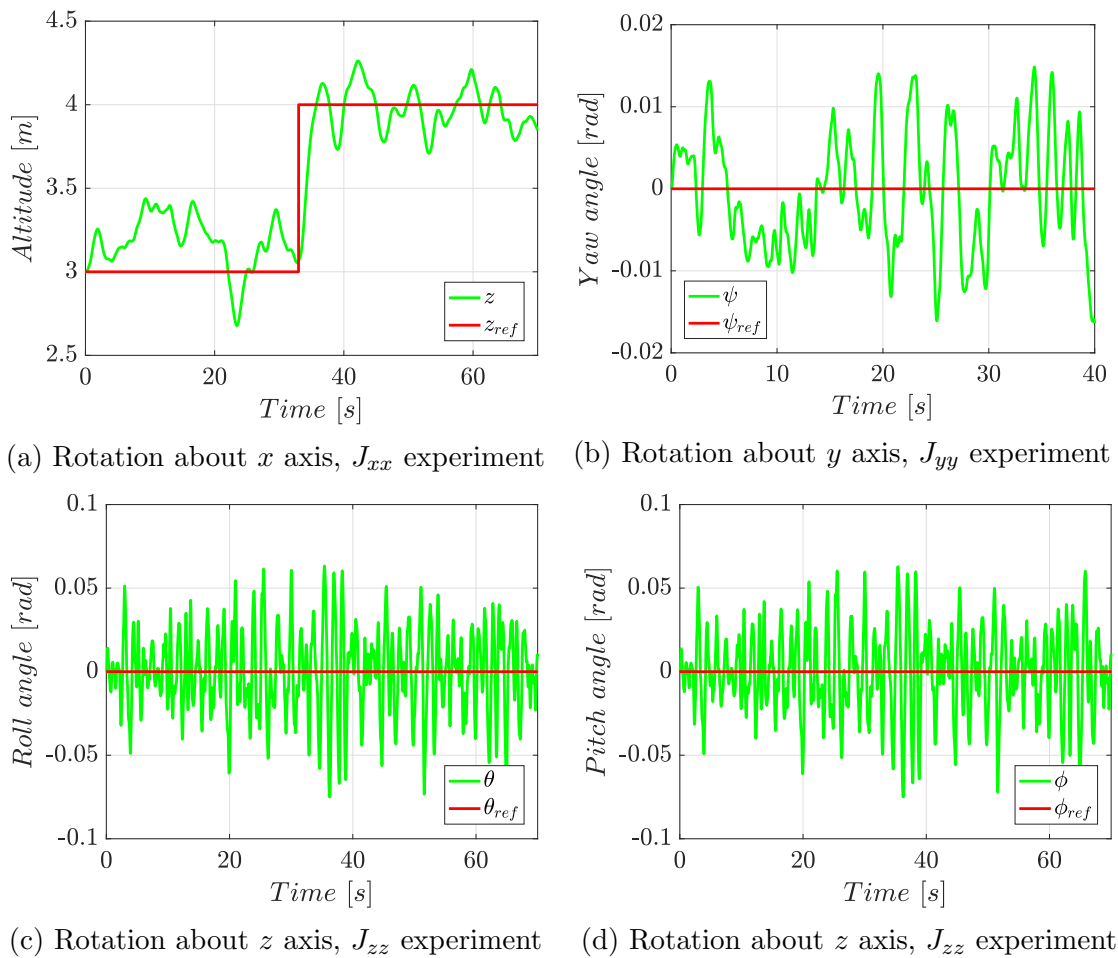


Figure 5.5: Rotation about  $x$ ,  $y$  and  $z$  axes during the bifilar pendulum experiments

### $H_\infty$ Controller

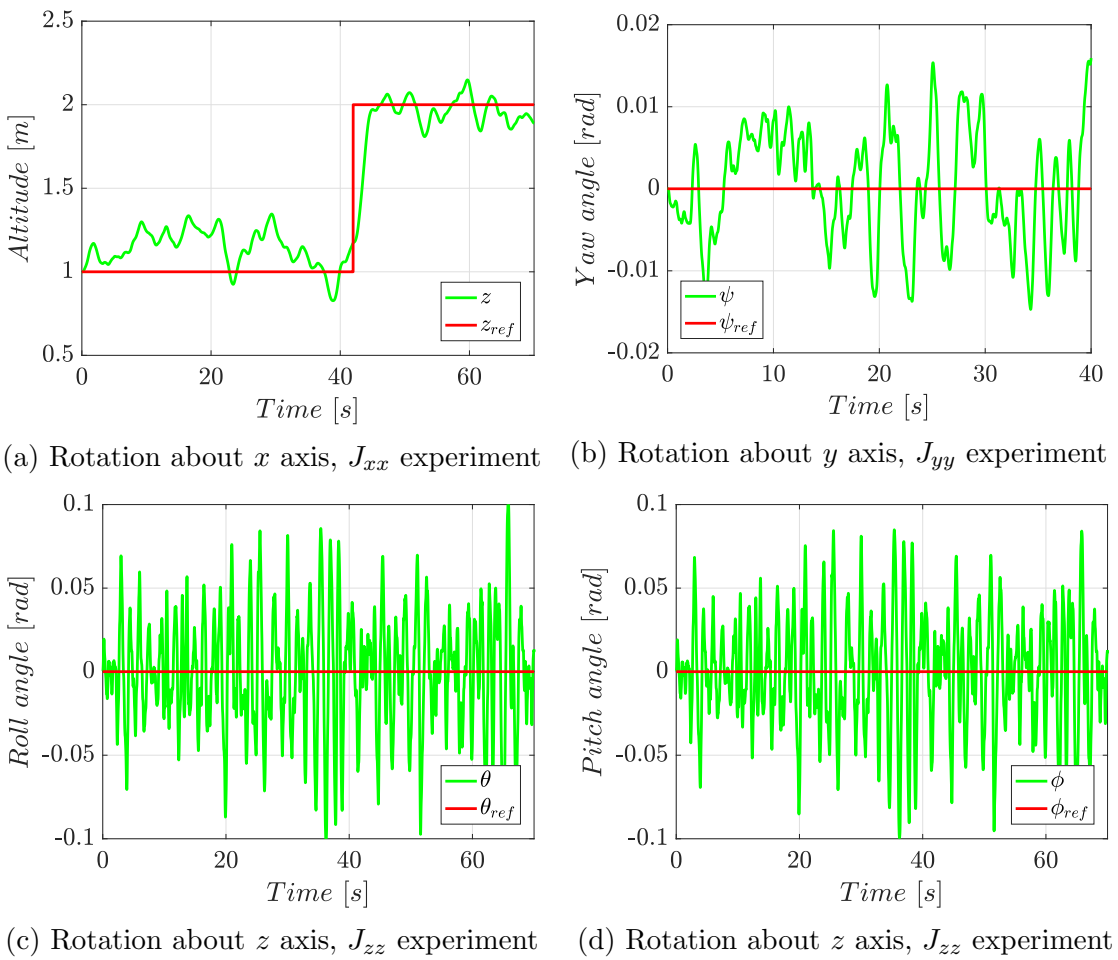


Figure 5.6: Rotation about  $x$ ,  $y$  and  $z$  axes during the bifilar pendulum experiments

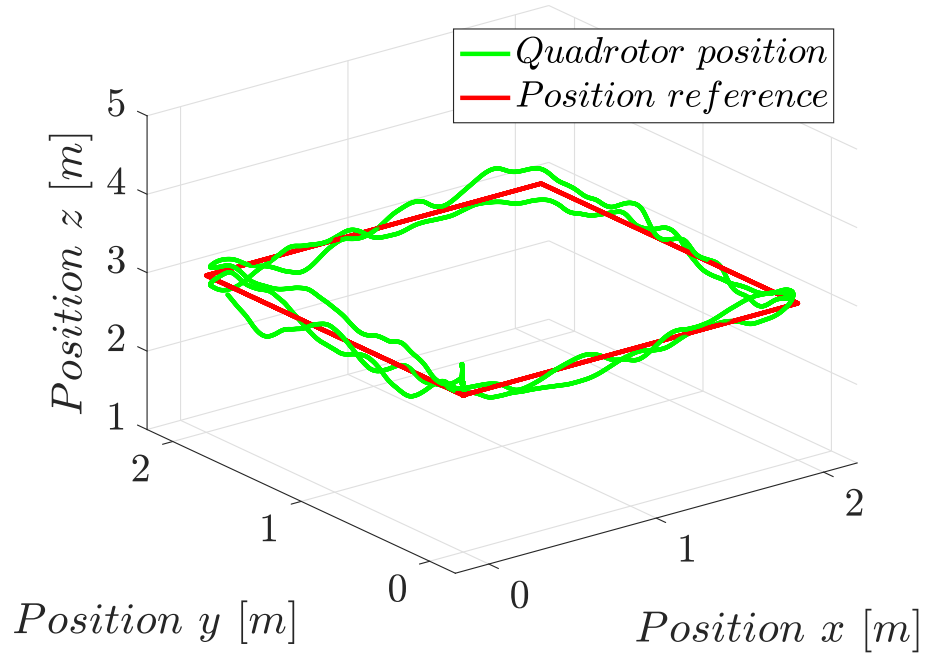


Figure 5.7: Closed-loop of the controlled system with an  $H_\infty$  controller.

### 5.3.3 GNSS-Dependent Mode

#### LQI Controller

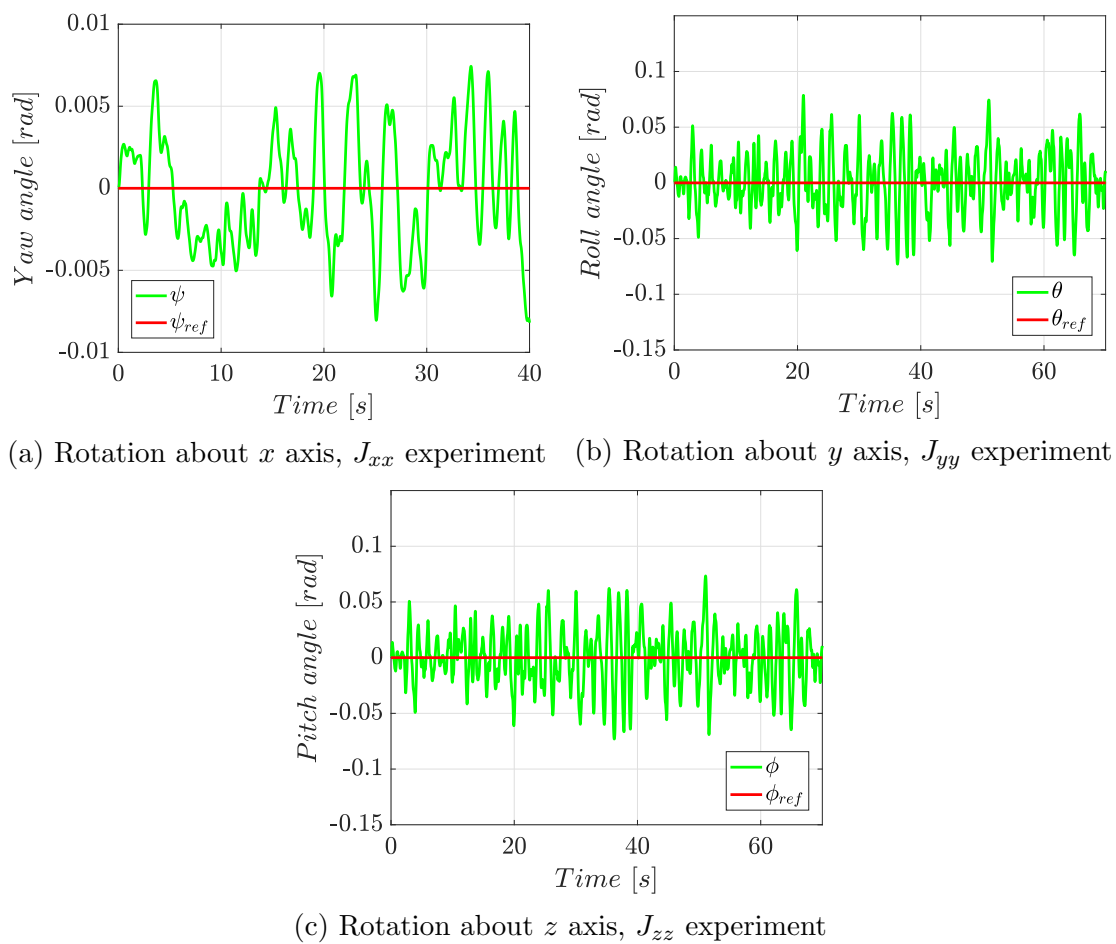


Figure 5.8: Rotation about  $x$ ,  $y$  and  $z$  axes during the bifilar pendulum experiments

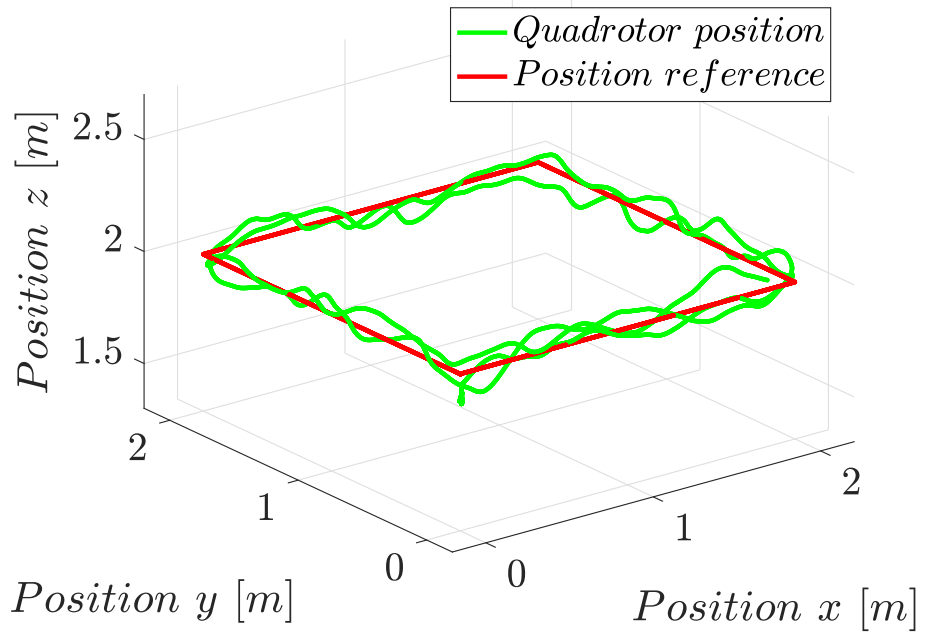
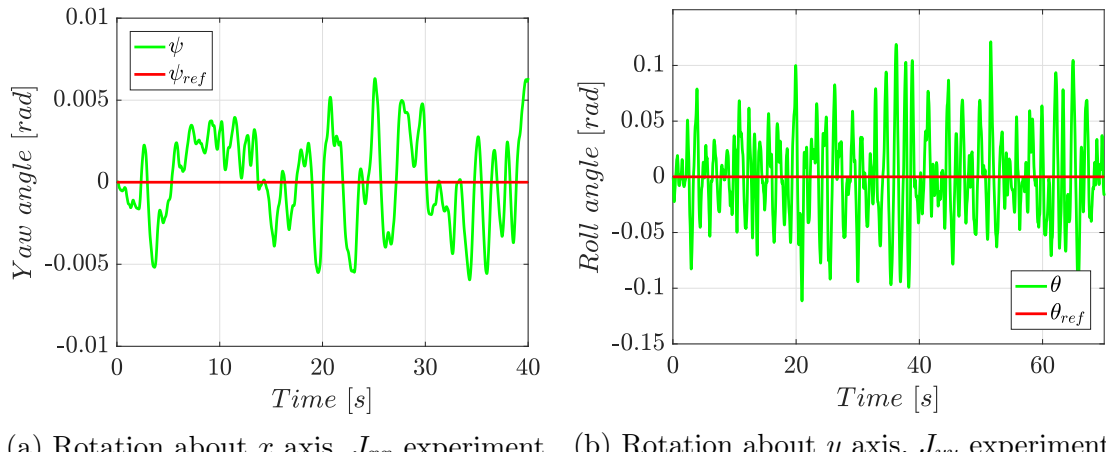
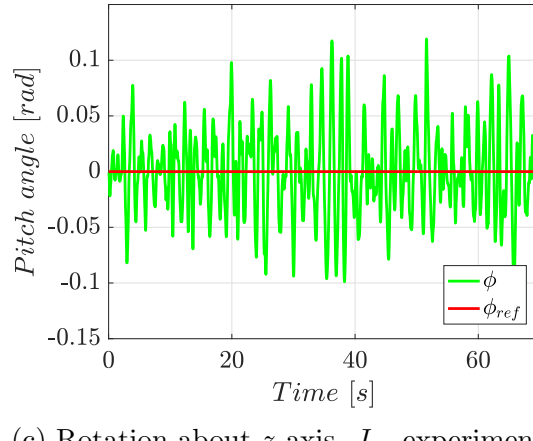


Figure 5.9: Closed-loop of the controlled system with an  $H_\infty$  controller.

### $H_\infty$ Controller



(a) Rotation about  $x$  axis,  $J_{xx}$  experiment   (b) Rotation about  $y$  axis,  $J_{yy}$  experiment



(c) Rotation about  $z$  axis,  $J_{zz}$  experiment

Figure 5.10: Rotation about  $x$ ,  $y$  and  $z$  axes during the bifilar pendulum experiments

## 5.4 Conclusions

rgrgrgtrgrtgr

# **Chapter 6**

## **Conclusions and Outlook**

In this thesis distributed algorithms



# Appendix A

## Publications

A. Astudillo, P. Muñoz, F. Alvarez and E. Rosero, “Altitude and attitude cascade controller for a smartphone-based quadcopter,” in *2017 International Conference on Unmanned Aircraft Systems (ICUAS)*. IEEE, jun 2017, pp. 1447–1454. [Online]. Available: <http://ieeexplore.ieee.org/document/7991400/>

A. Astudillo, B. Bacca and E. Rosero, “Optimal and robust controllers design for a smartphone-based quadrotor,” in *2017 IEEE 3rd Colombian Conference on Automatic Control (CCAC)*

**(Paper Submitted to Journal)** A. Astudillo, P. Muñoz and E. Rosero, “Cascade Controller for Autonomous Flight of a Smartphone-based Quadrotor,” in *Journal of Intelligent & Robotic Systems, SI: UAS-2017*.



# **Appendix B**

## **Supplementary Material**

All supplementary material including the Android app code, GCS code, Arduino code, 3D objects, etc., is hosted in: <https://goo.gl/U43bB6>



## **Appendix C**

### **Control Signals in Flight Tests**

Some text

## Stabilize Mode

### LQI Controller

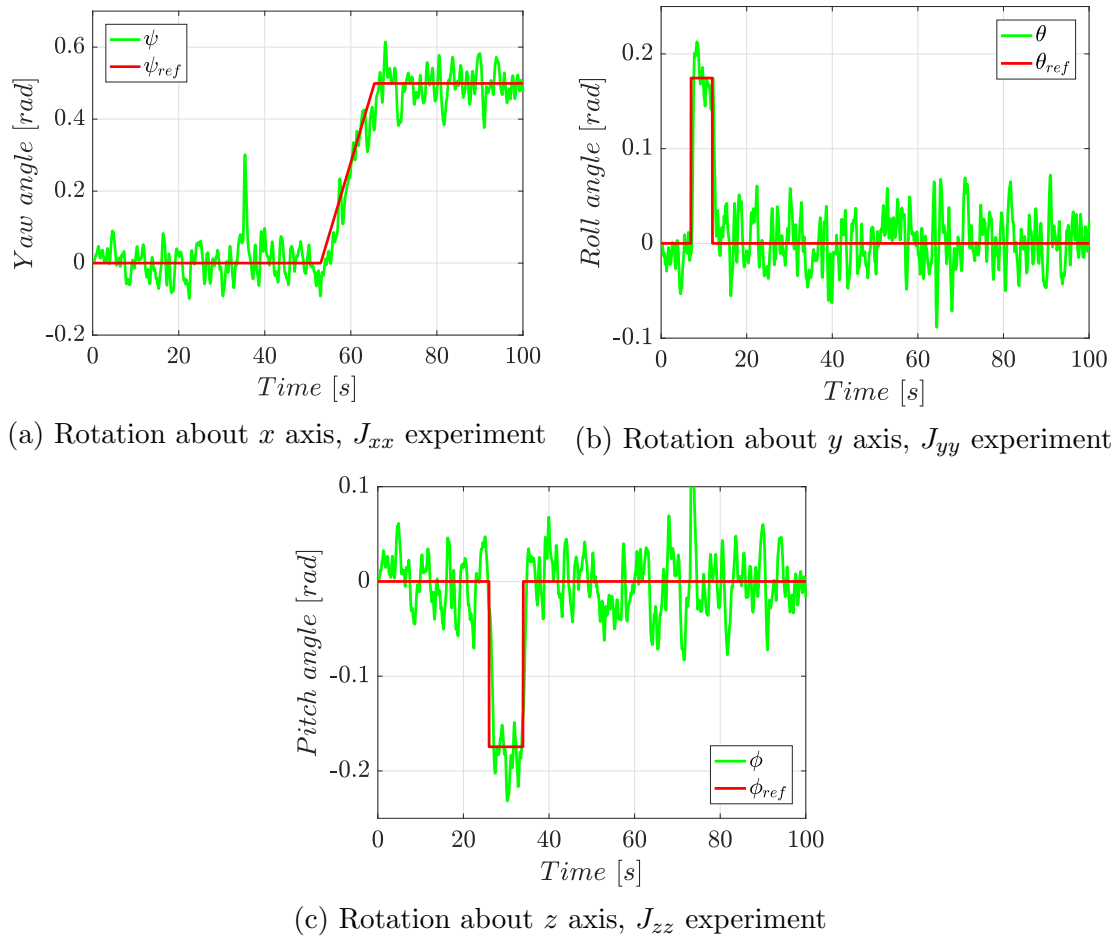


Figure C.1: Rotation about  $x$ ,  $y$  and  $z$  axes during the bifilar pendulum experiments

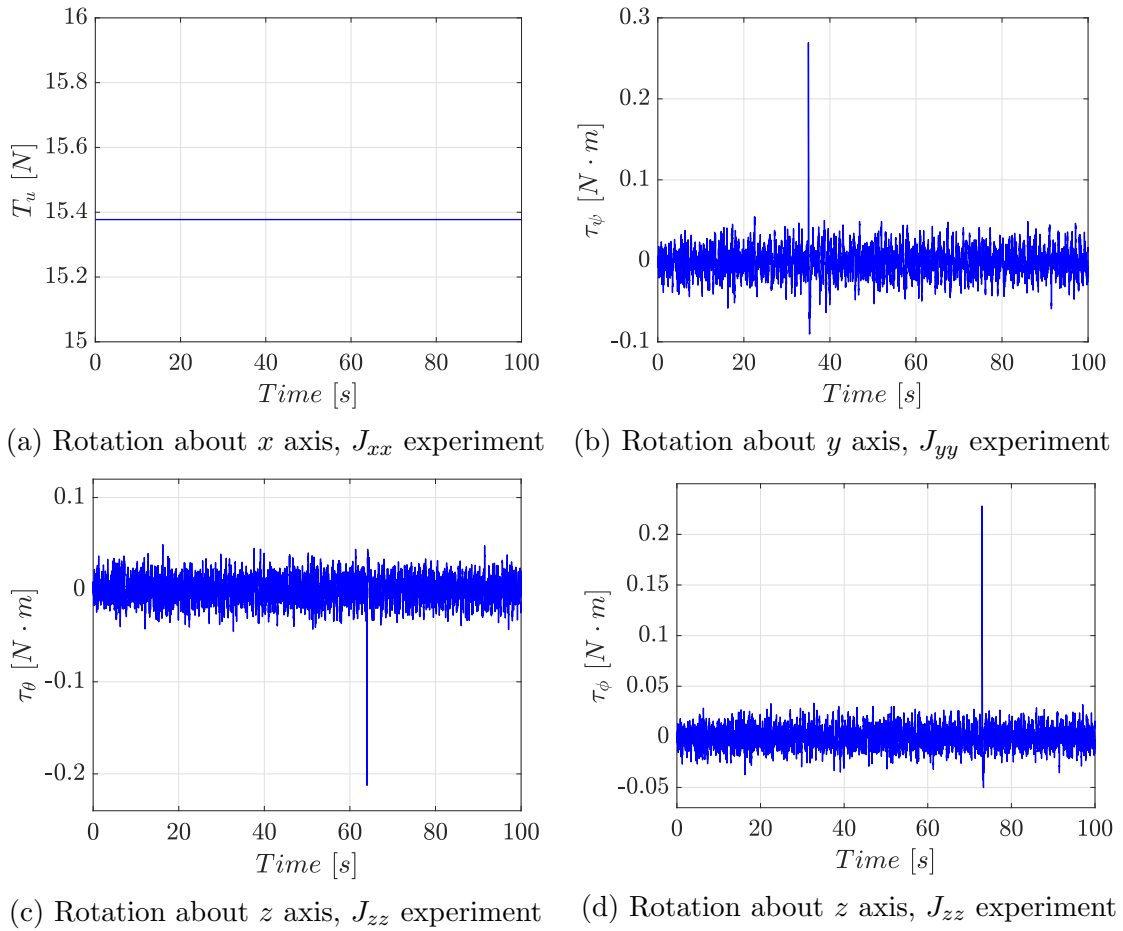


Figure C.2: Rotation about  $x$ ,  $y$  and  $z$  axes during the bifilar pendulum experiments

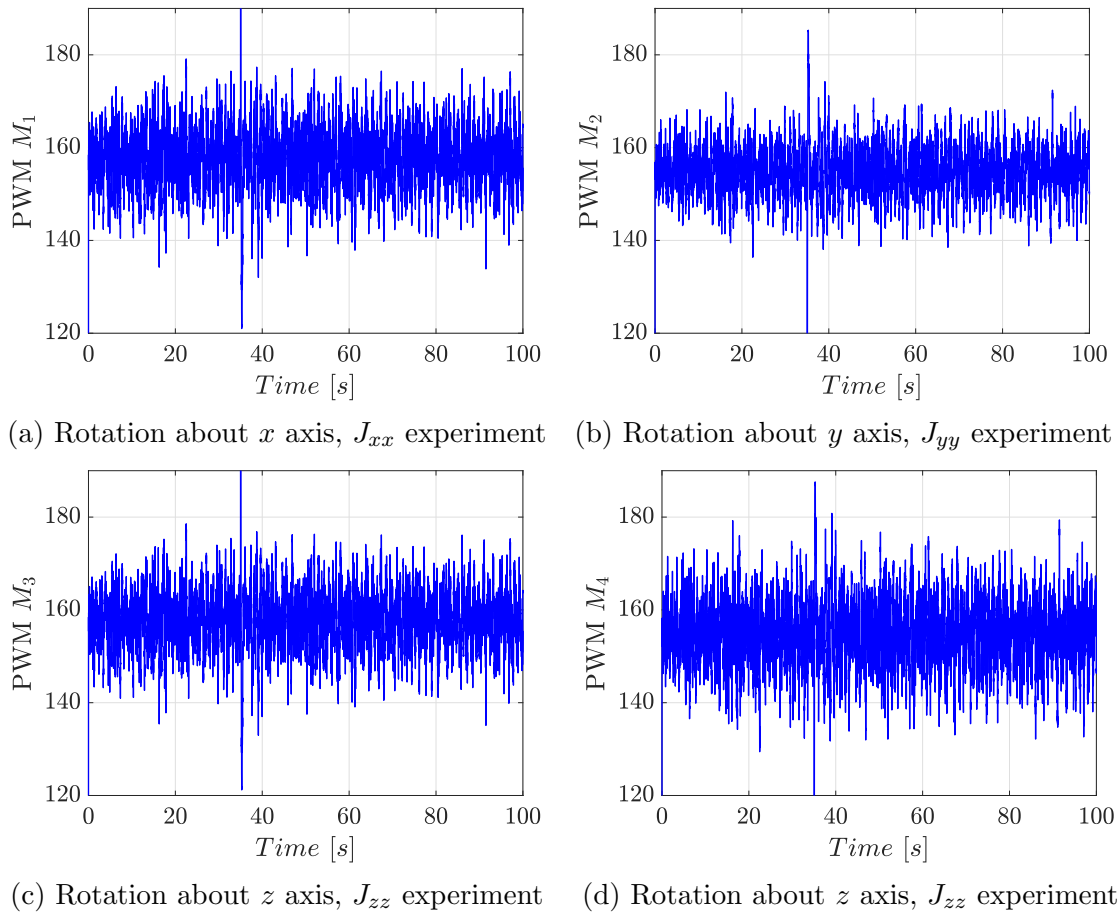


Figure C.3: Rotation about  $x$ ,  $y$  and  $z$  axes during the bifilar pendulum experiments

## $H_\infty$ Controller

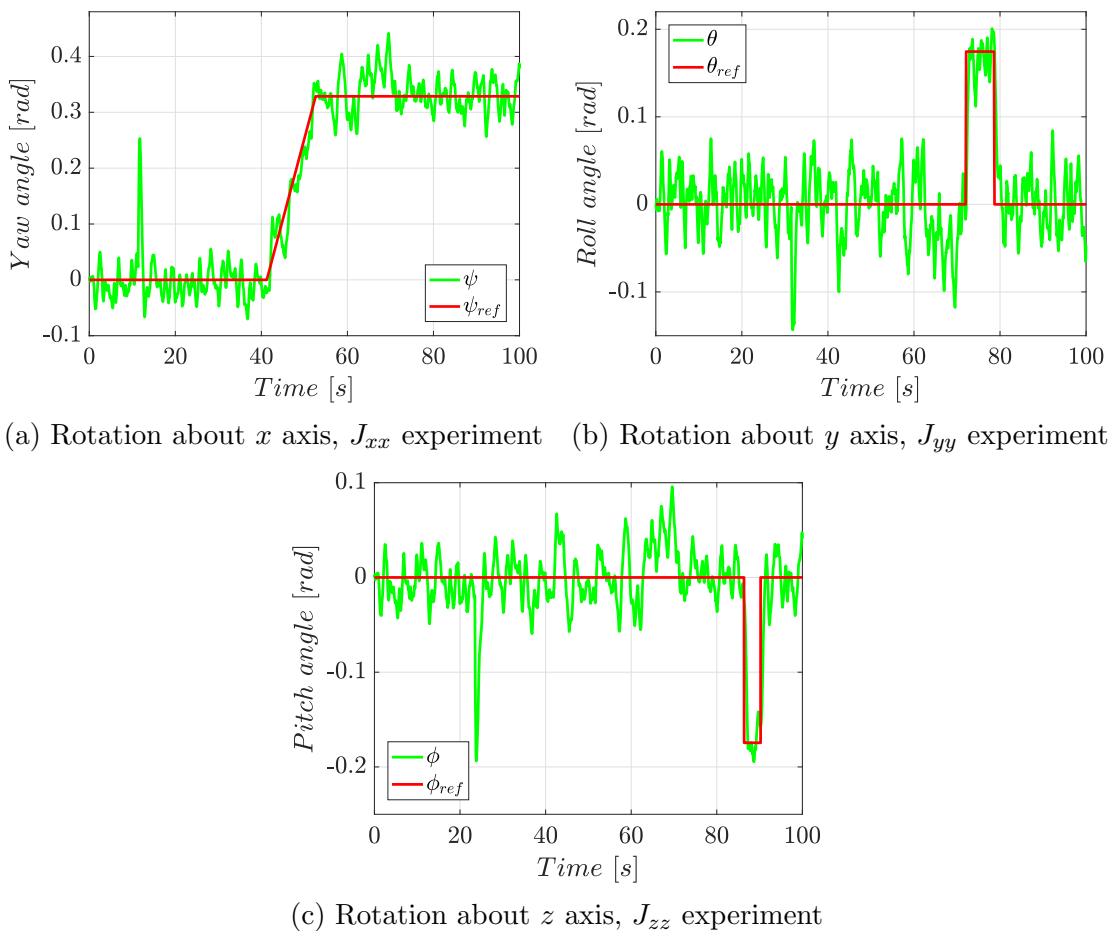


Figure C.4: Rotation about  $x$ ,  $y$  and  $z$  axes during the bifilar pendulum experiments

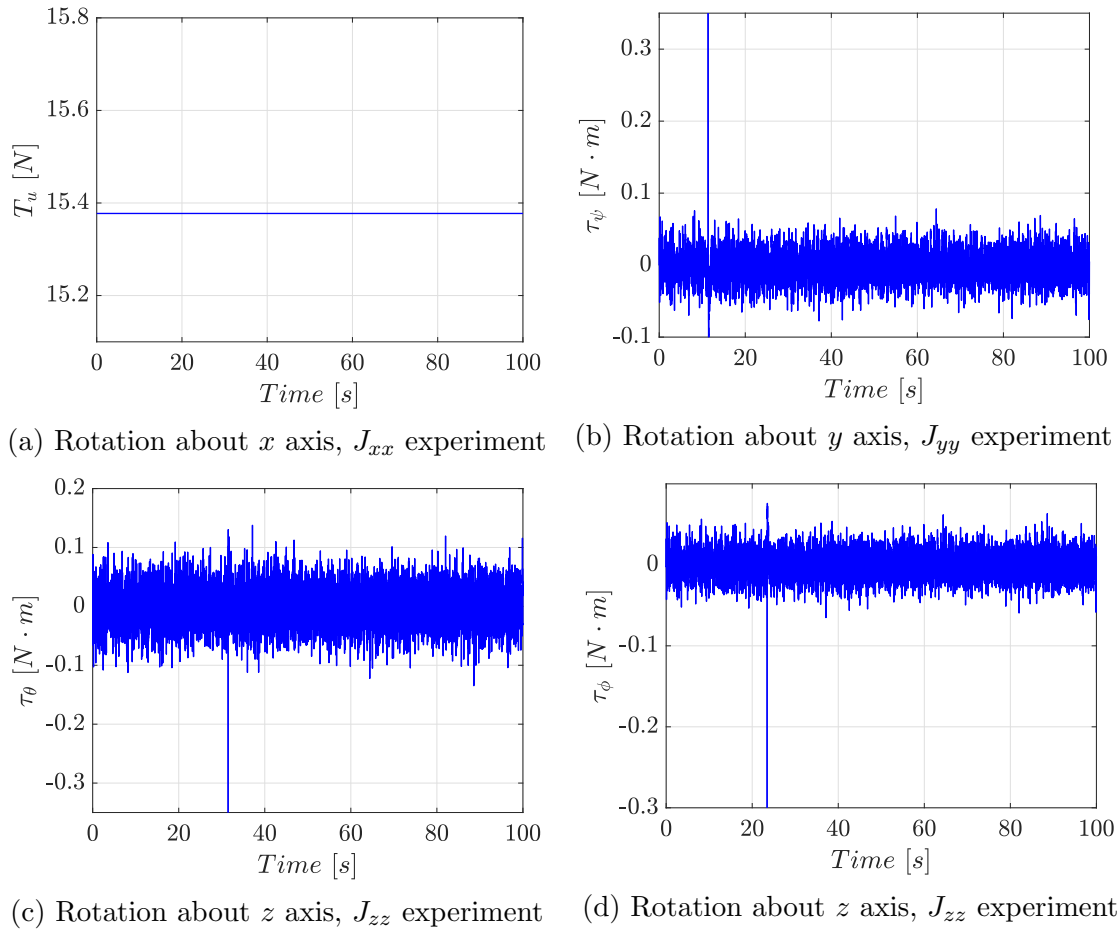


Figure C.5: Rotation about  $x$ ,  $y$  and  $z$  axes during the bifilar pendulum experiments

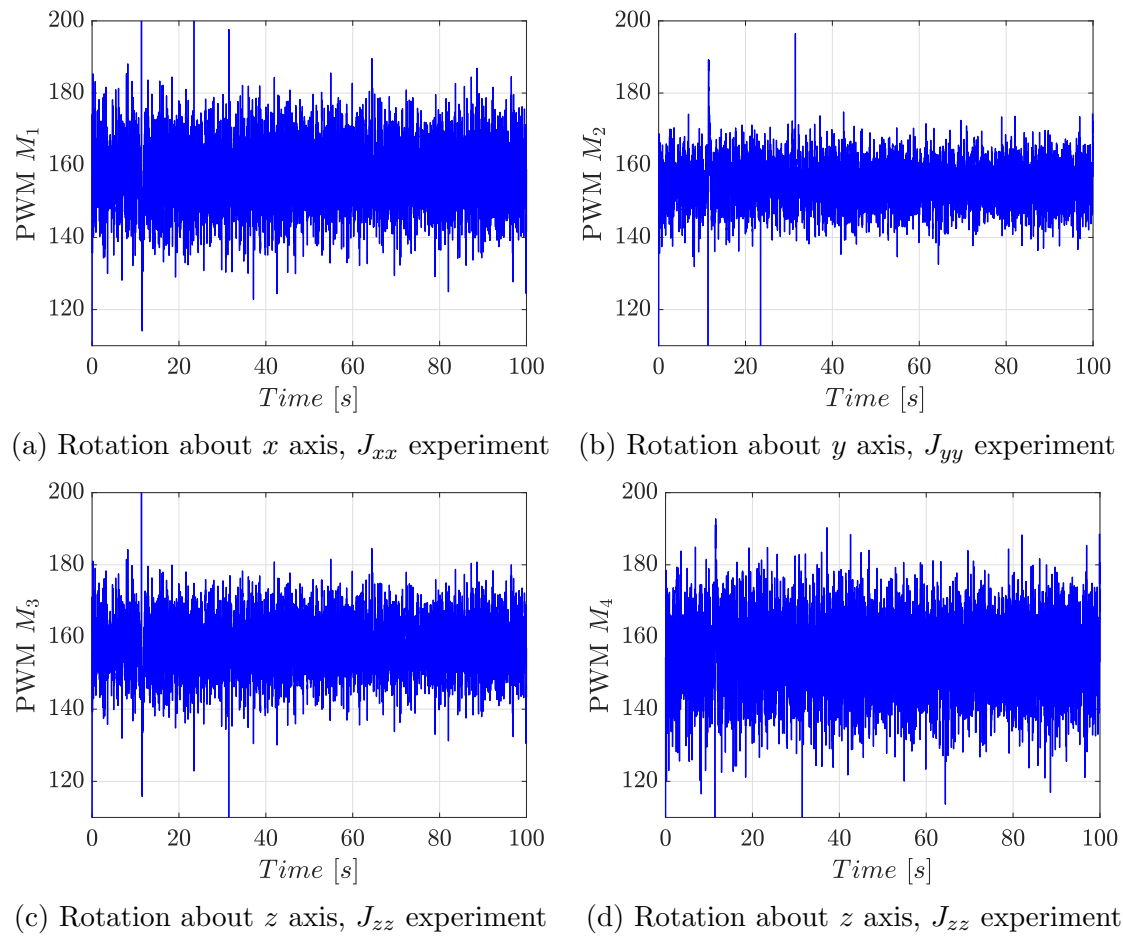


Figure C.6: Rotation about  $x$ ,  $y$  and  $z$  axes during the bifilar pendulum experiments

## Altitude Hold Mode

### LQI Controller

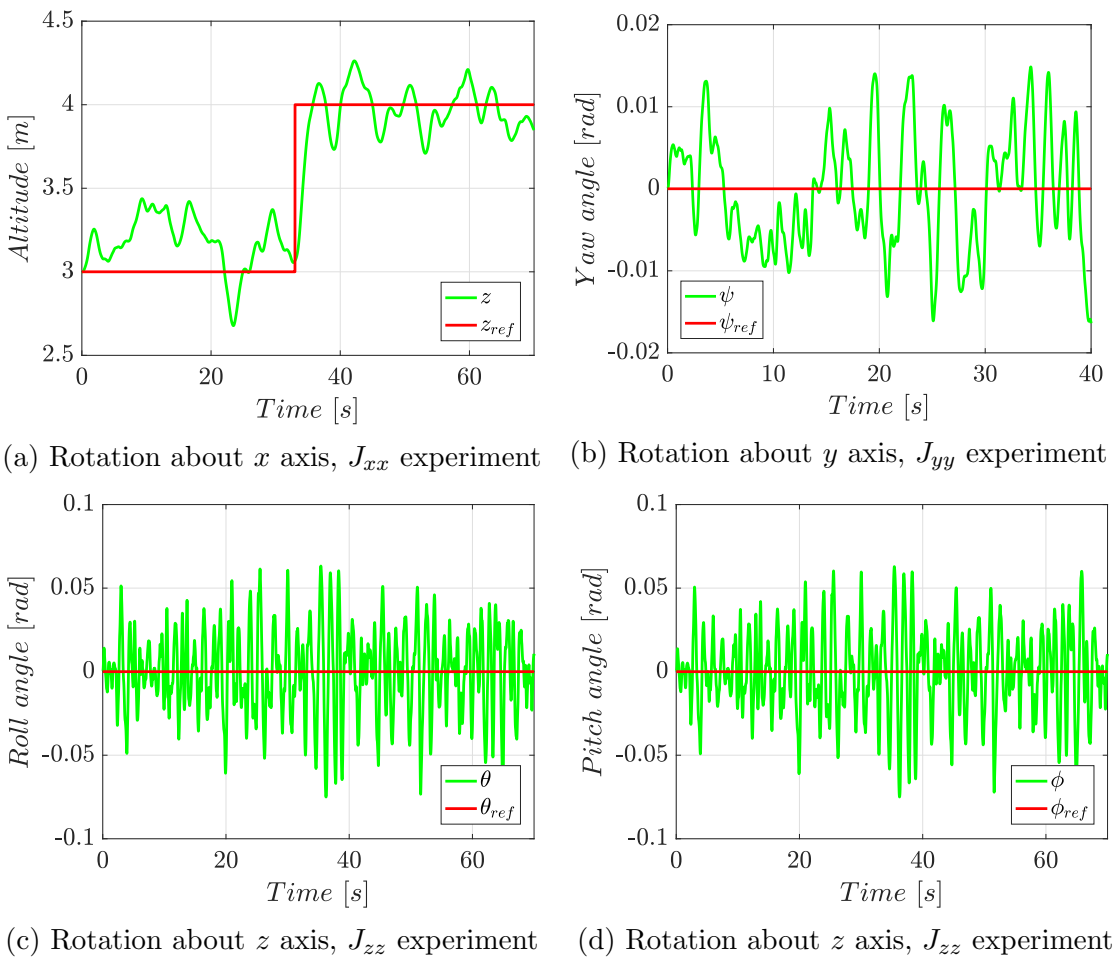


Figure C.7: Rotation about  $x$ ,  $y$  and  $z$  axes during the bifilar pendulum experiments

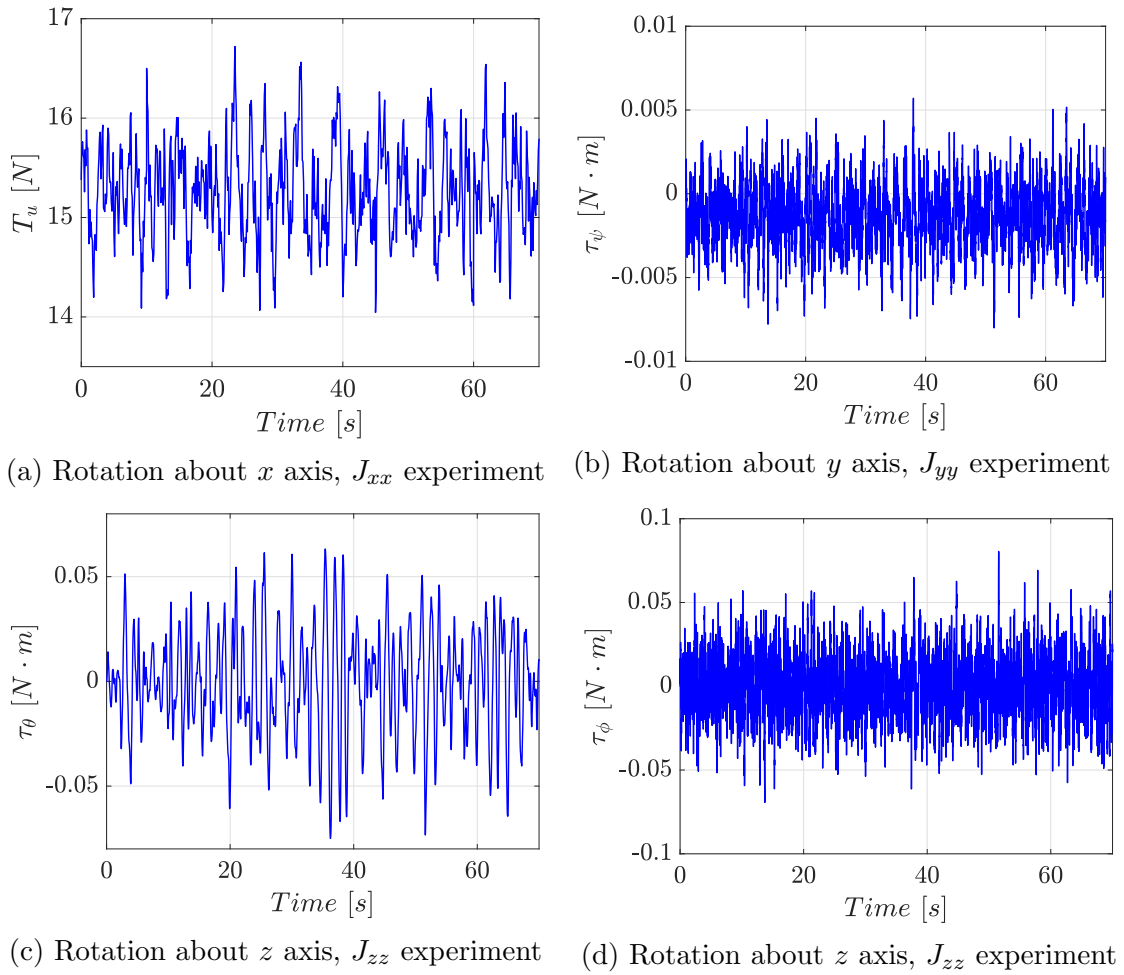


Figure C.8: Rotation about  $x$ ,  $y$  and  $z$  axes during the bifilar pendulum experiments

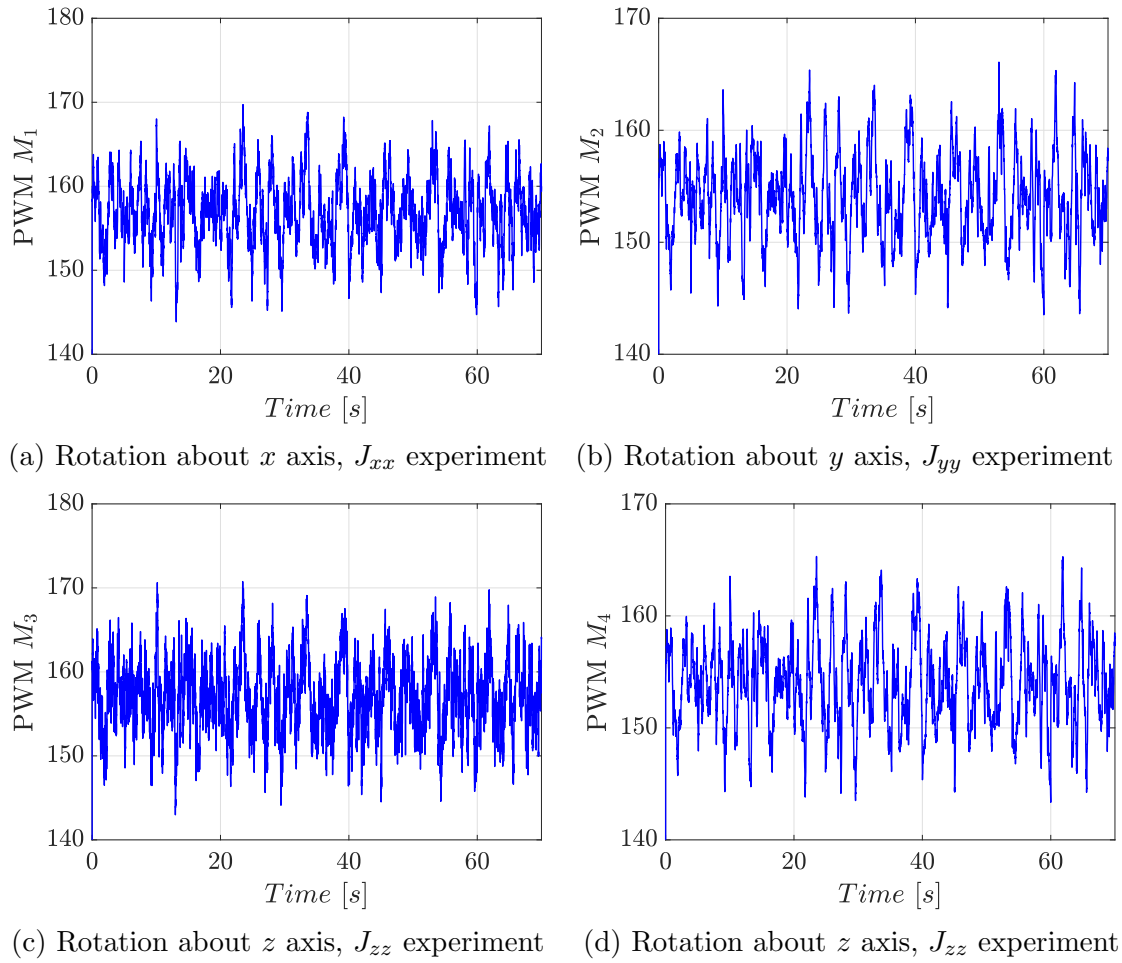


Figure C.9: Rotation about  $x$ ,  $y$  and  $z$  axes during the bifilar pendulum experiments

## $H_\infty$ Controller

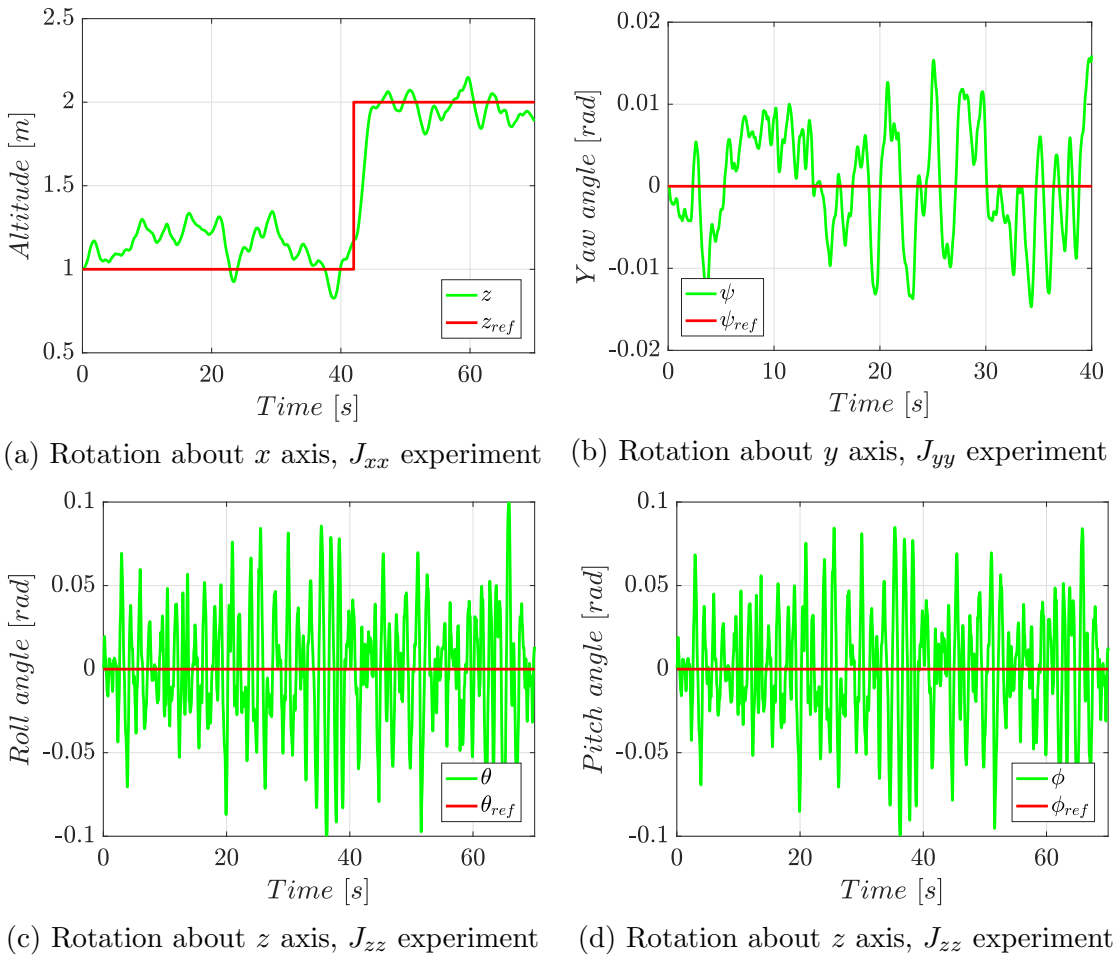


Figure C.10: Rotation about  $x$ ,  $y$  and  $z$  axes during the bifilar pendulum experiments

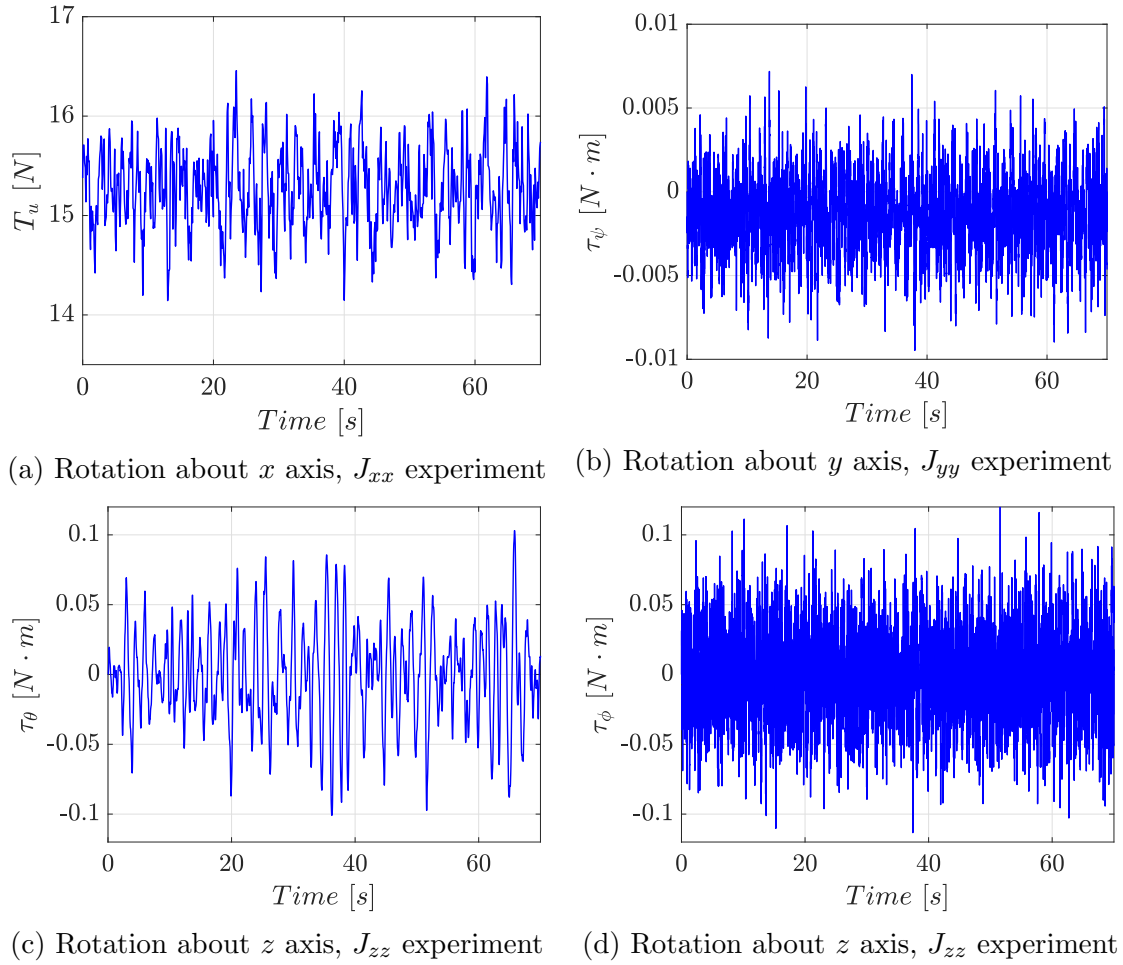


Figure C.11: Rotation about  $x$ ,  $y$  and  $z$  axes during the bifilar pendulum experiments

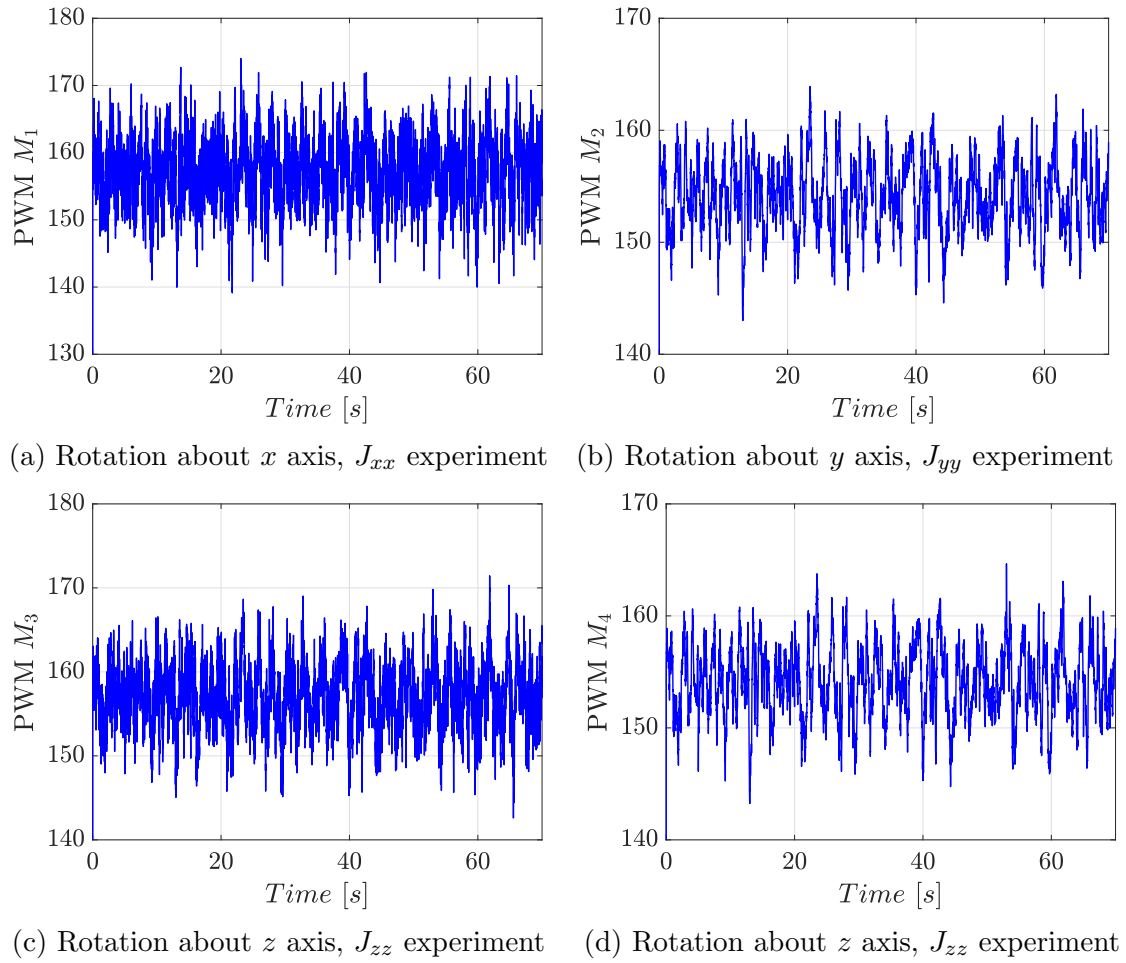


Figure C.12: Rotation about  $x$ ,  $y$  and  $z$  axes during the bifilar pendulum experiments

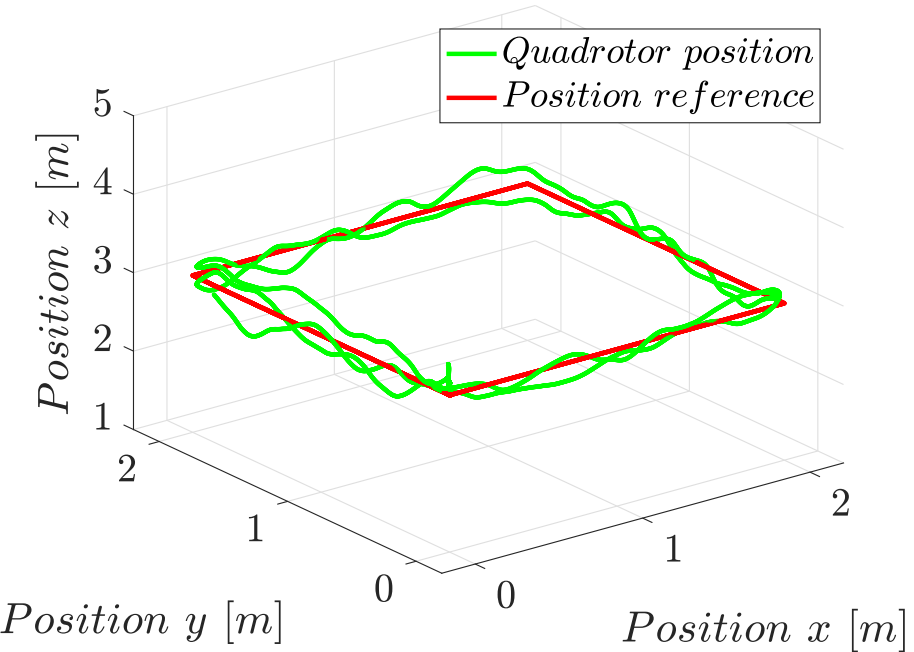
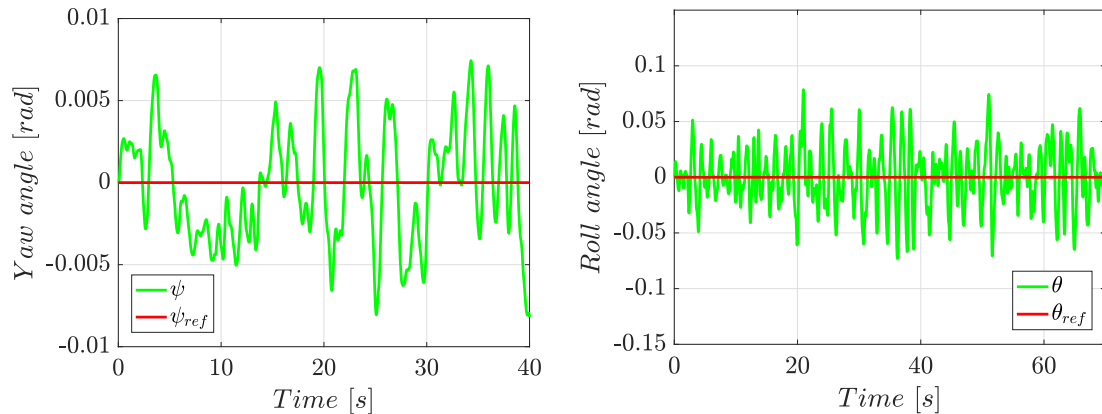


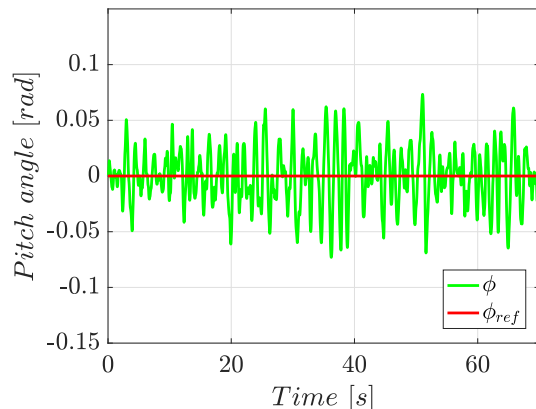
Figure C.13: Closed-loop of the controlled system with an  $H_\infty$  controller.

## GNSS-Dependent Mode

### LQI Controller



(a) Rotation about  $x$  axis,  $J_{xx}$  experiment    (b) Rotation about  $y$  axis,  $J_{yy}$  experiment



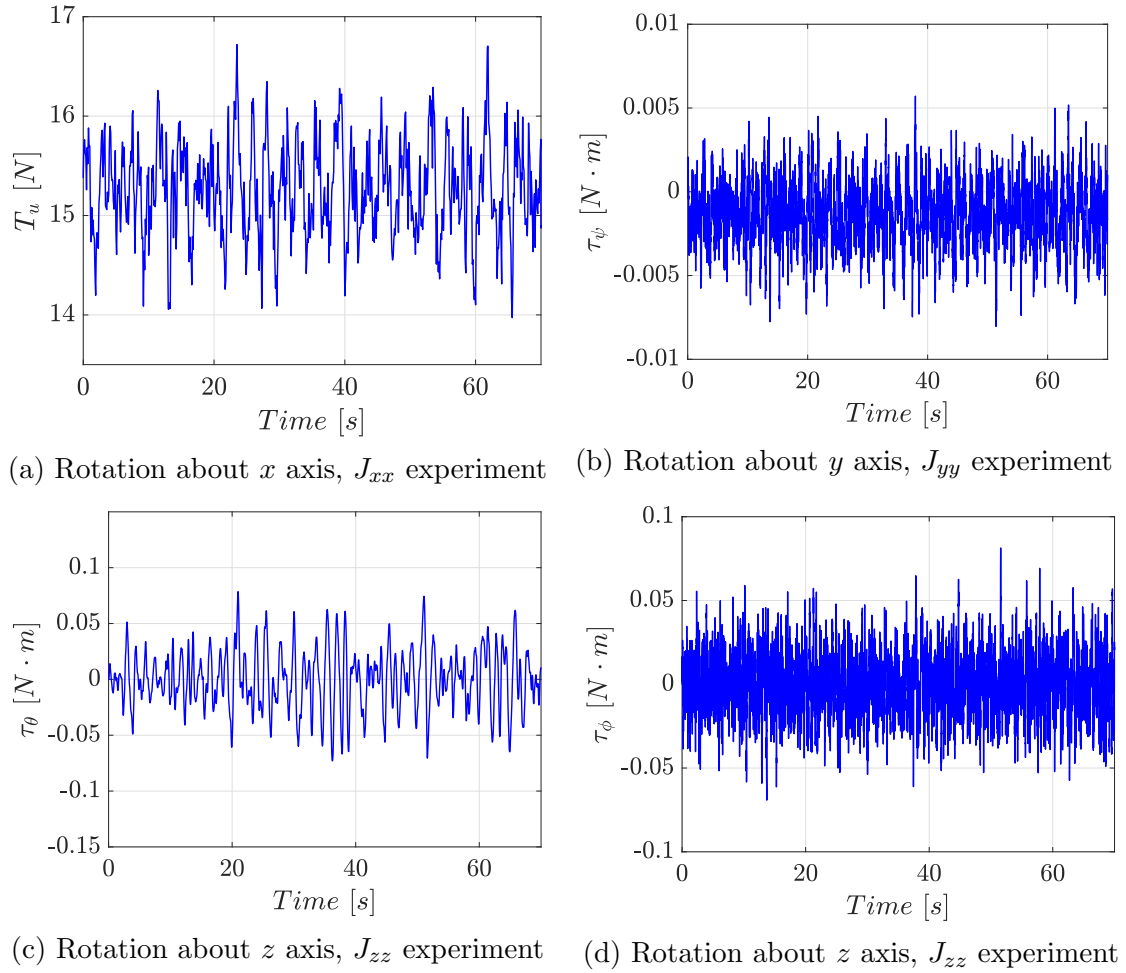


Figure C.15: Rotation about  $x$ ,  $y$  and  $z$  axes during the bifilar pendulum experiments

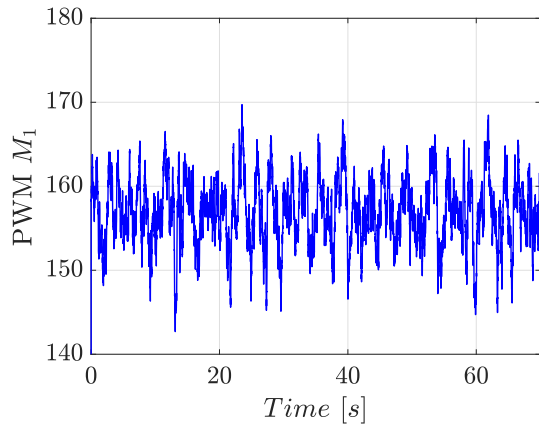
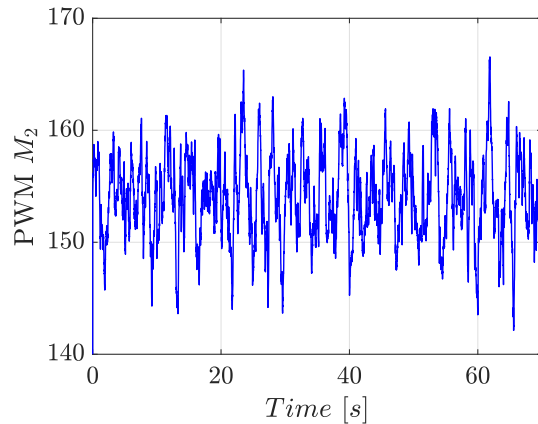
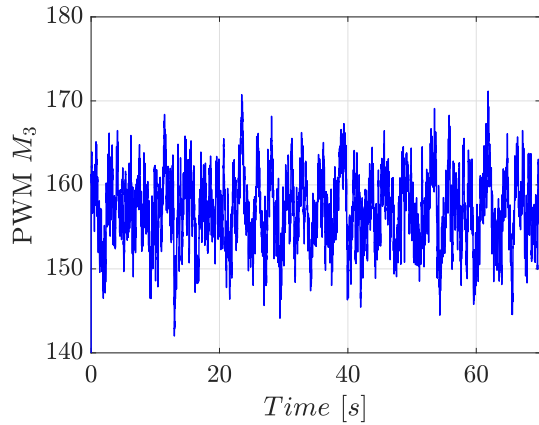
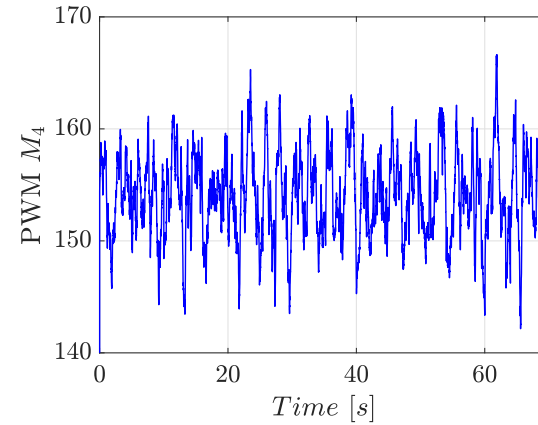
(a) Rotation about  $x$  axis,  $J_{xx}$  experiment(b) Rotation about  $y$  axis,  $J_{yy}$  experiment(c) Rotation about  $z$  axis,  $J_{zz}$  experiment(d) Rotation about  $z$  axis,  $J_{zz}$  experiment

Figure C.16: Rotation about  $x$ ,  $y$  and  $z$  axes during the bifilar pendulum experiments

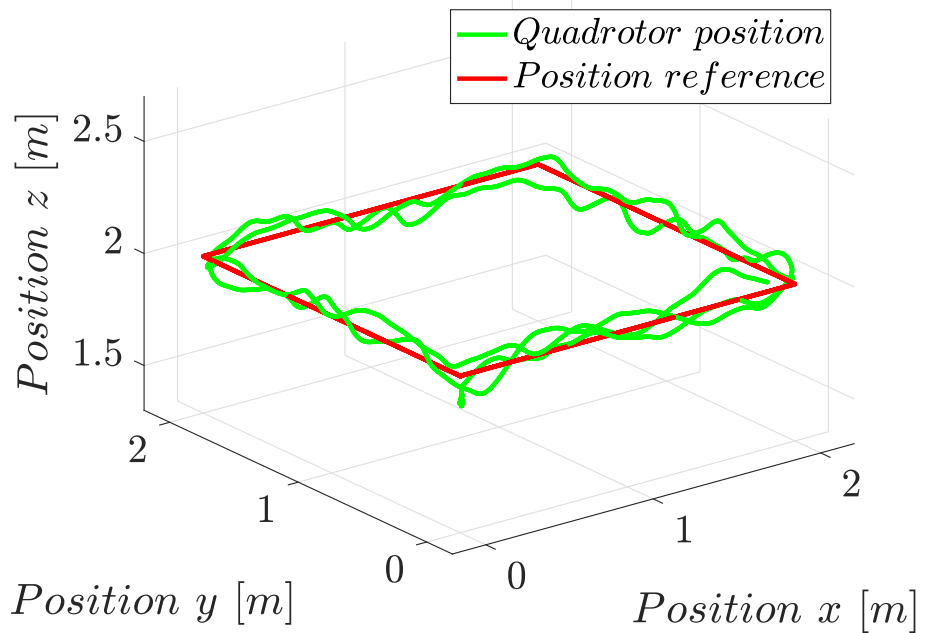


Figure C.17: Closed-loop of the controlled system with an  $H_\infty$  controller.

### $H_\infty$ Controller

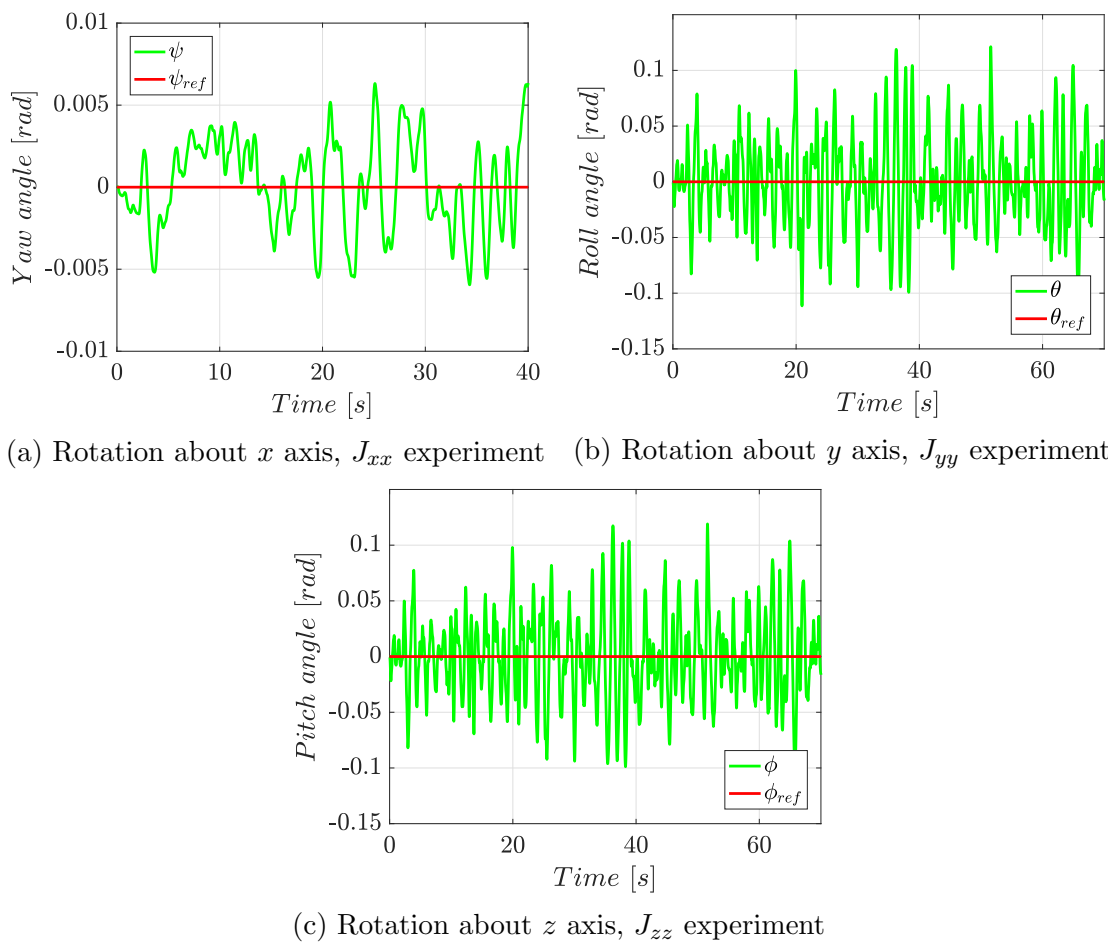


Figure C.18: Rotation about  $x$ ,  $y$  and  $z$  axes during the bifilar pendulum experi-

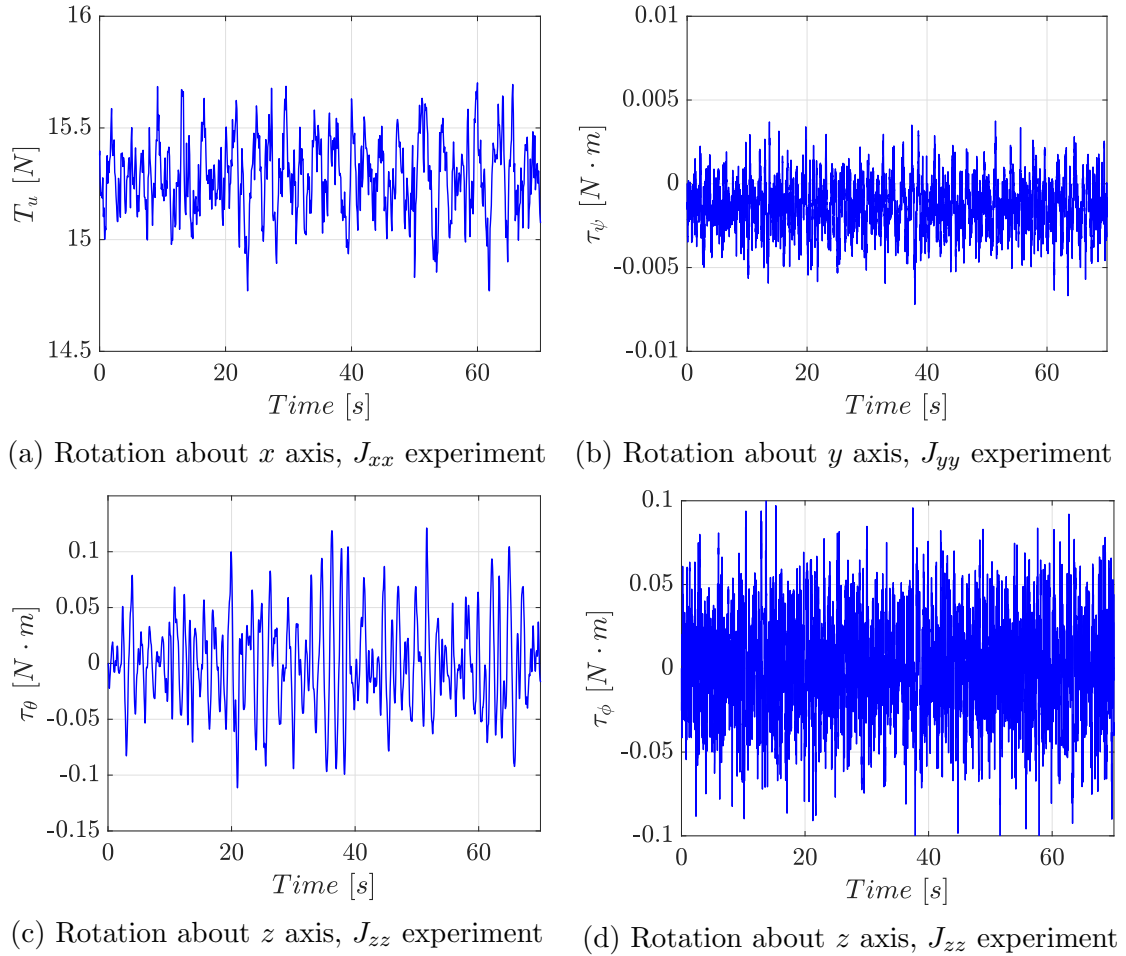


Figure C.19: Rotation about  $x$ ,  $y$  and  $z$  axes during the bifilar pendulum experiments

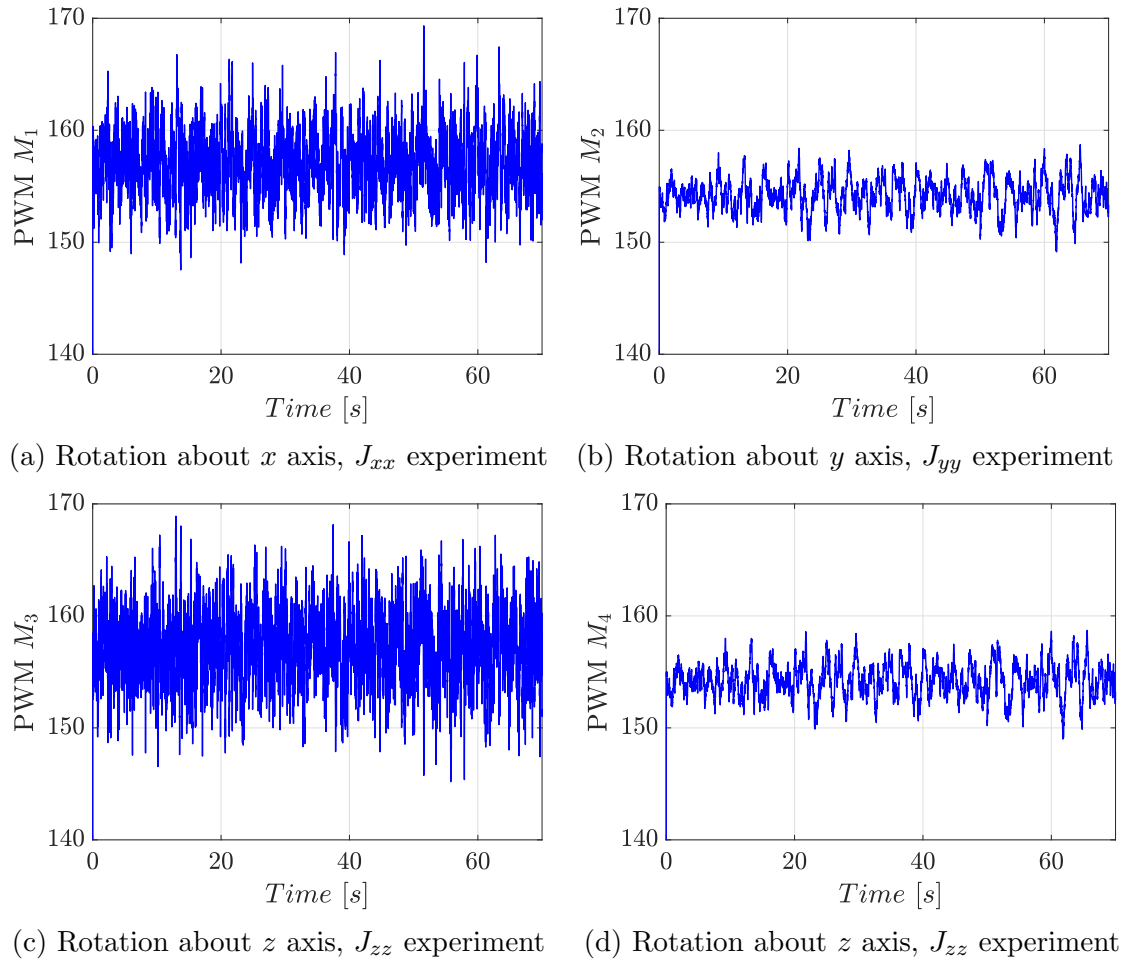


Figure C.20: Rotation about  $x$ ,  $y$  and  $z$  axes during the bifilar pendulum experiments



# Bibliography

- [1] S. Bouabdallah, “Design and Control of Quadrotors With Application To Autonomous Flying,” Ph.D. dissertation, École Polytechnique Fédérale de Lausanne, 2007.
- [2] M. Rahman, A. Ani, S. Yahaya, Z. Hussain, R. Boudville, and A. Ahmad, “Implementation of quadcopter as a teaching tool to enhance engineering courses,” in *2016 IEEE 8th International Conference on Engineering Education (ICEED)*. IEEE, dec 2016, pp. 32–37.
- [3] C. E. García and F. A. Herrera, “Percepción remota en cultivos de caña de azúcar usando una cámara multiespectral en vehículos aéreos no tripulados,” *Anais XVII Simpósio Brasileiro de Sensoriamento Remoto - SBSR*, pp. 4450 – 4457, 2015.
- [4] S. S. Kumar and A. S. Sundar, “The Rescue Mission with SQUADCOPTER by Real time GPS 3D surveillance,” *Journal of Basic and Applied Engineering Research*, vol. 1, no. 5, pp. pp. 60–63, 2014.
- [5] V. Gatteschi, F. Lamberti, G. Paravati, A. Sanna, C. Demartini, A. Lisanti, and G. Venezia, “New Frontiers of Delivery Services Using Drones: A Prototype System Exploiting a Quadcopter for Autonomous Drug Shipments,” in *2015 IEEE 39th Annual Computer Software and Applications Conference*, vol. 2. IEEE, jul 2015, pp. 920–927.
- [6] L. F. Gonzalez, M. P. G. Castro, and F. Tamagnone, “Multidisciplinary Design and Flight Testing of a Remote Gas/Particle Airborne Sensor System,” *28th International Congress of the Aeronautical Sciences*, pp. 1–13, 2012.
- [7] L. M. Argentim, W. C. Rezende, P. E. Santos, and R. A. Aguiar, “PID, LQR and LQR-PID on a quadcopter platform,” in *2013 International Conference on Informatics, Electronics and Vision (ICIEV)*. IEEE, may 2013, pp. 1–6.
- [8] M. F. Silva, A. C. Ribeiro, M. F. Santos, M. J. Carmo, L. M. Honório, E. J. Oliveira, and V. F. Vidal, “Design of angular PID controllers for quadcopters built with low cost equipment,” *2016 20th International Conference on System*

- Theory, Control and Computing, ICSTCC 2016 - Joint Conference of SINTES 20, SACCS 16, SIMSIS 20 - Proceedings*, pp. 216–221, 2016.
- [9] C. Liu, J. Pan, and Y. Chang, “PID and LQR trajectory tracking control for an unmanned quadrotor helicopter: Experimental studies,” in *2016 35th Chinese Control Conference (CCC)*. IEEE, jul 2016, pp. 10845–10850.
  - [10] E. Reyes-Valeria, R. Enriquez-Caldera, S. Camacho-Lara, and J. Guichard, “LQR control for a quadrotor using unit quaternions: Modeling and simulation,” in *CONIELECOMP 2013, 23rd International Conference on Electronics, Communications and Computing*. IEEE, mar 2013, pp. 172–178.
  - [11] Y. Dong, J. Fu, B. Yu, Y. Zhang, and J. Ai, “Position and heading angle control of an unmanned quadrotor helicopter using LQR method,” *Chinese Control Conference, CCC*, vol. 2015-Septe, pp. 5566–5571, 2015.
  - [12] B. Fan, J. Sun, and Y. Yu, “A LQR controller for a quadrotor: Design and experiment,” *Proceedings - 2016 31st Youth Academic Annual Conference of Chinese Association of Automation, YAC 2016*, pp. 81–86, 2017.
  - [13] K. Zhang, J. Chen, Y. Chang, and Y. Shi, “EKF-based LQR tracking control of a quadrotor helicopter subject to uncertainties,” *IECON Proceedings (Industrial Electronics Conference)*, pp. 5426–5431, 2016.
  - [14] G. Ganga and M. M. Dharmana, “MPC controller for trajectory tracking control of quadcopter,” in *2017 International Conference on Circuit ,Power and Computing Technologies (ICCPCT)*. IEEE, apr 2017, pp. 1–6.
  - [15] A. Castillo, R. Sanz, P. García, and P. Albertos, “A quaternion-based and active disturbance rejection attitude control for quadrotor,” *2016 IEEE International Conference on Information and Automation, IEEE ICIA 2016*, no. August, pp. 240–245, 2016.
  - [16] Y. Ameho, F. Niel, F. Defay, J.-M. Biannic, and C. Berard, “Adaptive control for quadrotors,” in *2013 IEEE International Conference on Robotics and Automation*. IEEE, may 2013, pp. 5396–5401.
  - [17] H. Gao, C. Liu, D. Guo, and J. Liu, “Fuzzy adaptive PD control for quadrotor helicopter,” in *2015 IEEE International Conference on Cyber Technology in Automation, Control, and Intelligent Systems (CYBER)*, no. JUNE. IEEE, jun 2015, pp. 281–286.
  - [18] B. Wang, L. Mu, and Y. Zhang, “Adaptive robust control of quadrotor helicopter towards payload transportation applications,” in *2017 36th Chinese Control Conference (CCC)*. IEEE, jul 2017, pp. 4774–4779.

- [19] B. J. Emran, J. Dias, L. Seneviratne, and G. Cai, “Robust adaptive control design for quadcopter payload add and drop applications,” *Chinese Control Conference, CCC*, vol. 2015-Septe, pp. 3252–3257, 2015.
- [20] B. Wang, L. Mu, and Y. Zhang, “Adaptive robust tracking control of quadrotor helicopter with parametric uncertainty and external disturbance,” in *2017 International Conference on Unmanned Aircraft Systems (ICUAS)*. IEEE, jun 2017, pp. 402–407.
- [21] A. Prayitno, V. Indrawati, and C. Arron, “H-Infinity Control for Pitch-Roll AR.Drone,” *TELKOMNIKA (Telecommunication Computing Electronics and Control)*, vol. 14, no. 3, p. 963, 2016.
- [22] J. P. Ortiz, L. I. Minchala, and M. J. Reinoso, “Nonlinear Robust H-Infinity PID Controller for the Multivariable System Quadrotor,” *IEEE Latin America Transactions*, vol. 14, no. 3, pp. 1176–1183, mar 2016.
- [23] P. Muñoz, “Control de Elevación Para Cuadricóptero Usando Un Celular Inteligente,” Bachelor Thesis, Universidad del Valle, Cali, 2017.
- [24] M. Moghadam and F. Caliskan, “Actuator and Sensor Fault Detection and Diagnosis of Quadrotor Based on Two-Stage Kalman Filter,” *2015 5th Australian Control Conference (AUCC)*, vol. 4, no. 1, pp. 2–7, 2015.
- [25] F. A. Goodarzi and T. Lee, “Extended Kalman filter on SE(3) for geometric control of a quadrotor UAV,” in *2016 International Conference on Unmanned Aircraft Systems (ICUAS)*, no. 3. IEEE, jun 2016, pp. 1371–1380.
- [26] K.-H. Oh and H.-S. Ahn, “Extended Kalman filter with multi-frequency reference data for quadrotor navigation,” in *2015 15th International Conference on Control, Automation and Systems (ICCAS)*, no. Iccas. IEEE, oct 2015, pp. 201–206.
- [27] K. D. Sebesta and N. Boizot, “A real-time adaptive high-gain EKF, applied to a quadcopter inertial navigation system,” *IEEE Transactions on Industrial Electronics*, vol. 61, no. 1, pp. 495–503, 2014.
- [28] J. Goslinski, W. Giernacki, and S. Gardecki, “Unscented Kalman Filter for an orientation module of a quadrotor mathematical model,” in *2013 9th Asian Control Conference (ASCC)*. IEEE, jun 2013, pp. 1–6.
- [29] Y. Al Younes, H. Noura, M. Muflehi, A. Rabhi, and A. El Hajjaji, “Model-free observer for state estimation applied to a quadrotor,” *2015 International Conference on Unmanned Aircraft Systems, ICUAS 2015*, pp. 1378–1384, 2015.

- [30] N. Xie, X. Lin, and Y. Yu, "Position estimation and control for quadrotor using optical flow and GPS sensors," in *2016 31st Youth Academic Annual Conference of Chinese Association of Automation (YAC)*. IEEE, nov 2016, pp. 181–186.
- [31] Q. Yu, F. He, Y. Zhang, and J. Ma, "Stereo-vision based obstacle motion information acquisition algorithm for quadrotors," in *2017 36th Chinese Control Conference (CCC)*. IEEE, jul 2017, pp. 5590–5595.
- [32] Y. Liu and M. Z. Q. Chen, "A novel three-axis visual attitude estimation algorithm with application to quadrotors," in *2017 29th Chinese Control And Decision Conference (CCDC)*. IEEE, may 2017, pp. 5436–5441.
- [33] ArduPilot Dev Team, "Copter - Flight Modes," 2016. [Online]. Available: <http://ardupilot.org/copter/docs/flight-modes.html>
- [34] N. Oros and J. L. Krichmar, "Smartphone Based Robotics: Powerful, Flexible and Inexpensive Robots for Hobbyists, Educators, Students and Researchers," 2013.
- [35] J. P. de A. Barbosa, F. do P. de C. Lima, L. dos S. Coutinho, J. P. R. Rodrigues Leite, J. Barbosa Machado, C. Henrique Valerio, and G. Sousa Bastos, "ROS, Android and cloud robotics: How to make a powerful low cost robot," in *2015 International Conference on Advanced Robotics (ICAR)*. IEEE, jul 2015, pp. 158–163.
- [36] M. A. Gunawan, F. Sulaiman, T. A. Putra, C. Daniel Hasudungan, and R. F. Sari, "Object-following robot using adaptive cruise control algorithm with IOIO," in *2014 International Conference on Intelligent Green Building and Smart Grid (IGBSG)*. IEEE, apr 2014, pp. 1–5.
- [37] T. Tetzlaff, R. Zandian, L. Drüppel, and U. Witkowski, *Robot Intelligence Technology and Applications 2012*, ser. Advances in Intelligent Systems and Computing, J.-H. Kim, E. T. Matson, H. Myung, and P. Xu, Eds. Berlin, Heidelberg: Springer Berlin Heidelberg, 2013, vol. 208.
- [38] A. Drumea, "Control of Industrial Systems Using Android-Based Devices," *36th Int. Spring Seminar on Electronics Technology*, pp. 405–408, 2013.
- [39] K.-w. Lin, Z.-h. Wu, and Y.-l. Lin, "Applications of Temperature Control Based on Android Platform," *Proceedings of the International MultiConference of Engineers and Computer Scientists*, vol. II, 2014.
- [40] N.-V. Truong and D.-L. Vu, "Remote monitoring and control of industrial process via wireless network and Android platform," *2012 International Conference on Control, Automation and Information Sciences (ICCAIS)*, no. 1, pp. 340–343, 2012.

- [41] Z. Lu, F. Nagata, K. Watanabe, and M. K. Habib, “iOS application for quadrotor remote control,” *Artificial Life and Robotics*, vol. 22, no. 3, pp. 374–379, sep 2017.
- [42] L. F. Aristizabal, D. F. Almario, and J. A. Lopez, “Development of an Android App as a learning tool of dynamic systems and automatic control,” in *2014 III International Congress of Engineering Mechatronics and Automation (CIIMA)*. IEEE, oct 2014, pp. 1–5.
- [43] S. Wu Wu, “Sintonización de controladores PI/PID mediante el desarrollo de una aplicación en Android,” Ph.D. dissertation, Universidad de Costa Rica, 2013.
- [44] J. García Téllez and D. F. Ochoa Calambás, “Desarrollo de una plataforma de monitorización, control y comunicación con teléfonos inteligentes, para laboratorios portátiles de soporte al área de señales y sistemas,” Bachelor Thesis, Universidad del Valle, Cali, 2015.
- [45] V. A. Isuru, M. A. I. M. Dharmadasa, D. V. B. C. Jayasinghe, and C. I. Keppitiyagama, “Reusing discarded-smartphone capabilities on quadcopters: The rationale, benefits and issues,” in *2016 Sixteenth International Conference on Advances in ICT for Emerging Regions (ICTer)*. IEEE, sep 2016, pp. 229–236.
- [46] C. Pearce, M. Guckenber, B. Holden, A. Leach, R. Hughes, C. Xie, M. Hassett, A. Adderley, L. E. Barnes, M. Sherriff, and G. C. Lewin, “Designing a spatially aware, automated quadcopter using an Android control system,” in *2014 Systems and Information Engineering Design Symposium (SIEDS)*, vol. 00, no. c. IEEE, apr 2014, pp. 23–28.
- [47] A. Bjälemark and H. Bergkvist, “Quadcopter control using Android based sensing,” *Advances in Electrical and Computer Engineering*, pp. 15–21, 2014.
- [48] G. Loianno, G. Cross, C. Qu, Y. Mulgaonkar, J. A. Hesch, and V. Kumar, “Flying Smartphones: Automated Flight Enabled by Consumer Electronics,” *IEEE Robotics & Automation Magazine*, vol. 22, no. 2, pp. 24–32, jun 2015.
- [49] G. Loianno, Y. Mulgaonkar, C. Brunner, D. Ahuja, A. Ramanandan, M. Chari, S. Diaz, and V. Kumar, “Smartphones power flying robots,” in *2015 IEEE/RSJ International Conference on Intelligent Robots and Systems (IROS)*. IEEE, sep 2015, pp. 1256–1263.
- [50] M. A. Alsharif and M. S. Holzel, “Estimation of a drone’s rotational dynamics with piloted Android flight data,” in *2016 IEEE 55th Conference on Decision and Control (CDC)*, no. Cdc. IEEE, dec 2016, pp. 1199–1204.

- [51] M. A. Alsharif, Y. E. Arslantas, and M. S. Holzel, "Advanced PID attitude control of a quadcopter using asynchronous android flight data," in *2017 International Conference on Unmanned Aircraft Systems (ICUAS)*. IEEE, jun 2017, pp. 1602–1607.
- [52] ——, "A comparison between advanced model-free PID and model-based LQI attitude control of a quadcopter using asynchronous android flight data," in *2017 25th Mediterranean Conference on Control and Automation (MED)*. IEEE, jul 2017, pp. 1023–1028.
- [53] L. Aldrovandi, M. Hayajneh, M. Melega, M. Furci, R. Naldi, and L. Marconi, "A smartphone based quadrotor: Attitude and position estimation," in *2015 International Conference on Unmanned Aircraft Systems (ICUAS)*. IEEE, jun 2015, pp. 1251–1259.
- [54] P. Bryant, G. Gradwell, and D. Claveau, "Autonomous UAS controlled by onboard smartphone," in *2015 International Conference on Unmanned Aircraft Systems (ICUAS)*. IEEE, jun 2015, pp. 451–454.
- [55] H. Liu and X. Wang, "Quaternion-based robust attitude control for quadrotors," in *2015 International Conference on Unmanned Aircraft Systems (ICUAS)*. IEEE, jun 2015, pp. 920–925.
- [56] R. Lopez, I. Gonzalez-Hernandez, S. Salazar, A. E. Rodriguez, J. J. Ordaz, and A. Osorio, "Disturbance rejection for a Quadrotor aircraft through a robust control," in *2015 International Conference on Unmanned Aircraft Systems (ICUAS)*. IEEE, jun 2015, pp. 409–415.
- [57] J. Jung, Y. Jung, D. You, and D. H. Shim, "A flight control system design for highly unstable unmanned combat aerial vehicles," in *2014 International Conference on Unmanned Aircraft Systems (ICUAS)*. IEEE, may 2014, pp. 1117–1125.
- [58] S. Kohno and K. Uchiyama, "Design of robust controller of fixed-wing UAV for transition flight," in *2014 International Conference on Unmanned Aircraft Systems (ICUAS)*. IEEE, may 2014, pp. 1111–1116.
- [59] B. Shang, J. Liu, T. Zhao, and Y. Chen, "Fractional order robust visual servoing control of a quadrotor UAV with larger sampling period," in *2016 International Conference on Unmanned Aircraft Systems (ICUAS)*, vol. 1, no. 209. IEEE, jun 2016, pp. 1228–1234.
- [60] S. Salazar, I. Gonzalez-Hernandez, R. Lopez, and R. Lozano, "Simulation and robust trajectory-tracking for a Quadrotor UAV," in *2014 International Conference on Unmanned Aircraft Systems (ICUAS)*. IEEE, may 2014, pp. 1167–1174.

- [61] T. Bresciani, "Modelling, Identification and Control of a Quadrotor Helicopter," Master's thesis, Lund University, 2008.
- [62] M. Faessler, D. Falanga, and D. Scaramuzza, "Thrust Mixing, Saturation, and Body-Rate Control for Accurate Aggressive Quadrotor Flight," *IEEE Robotics and Automation Letters*, vol. PP, no. 99, pp. 1–7, 2016.
- [63] M. Emam and A. Fakharian, "Attitude tracking of quadrotor UAV via mixed H<sub>2</sub>/H<sub>∞</sub> controller: An LMI based approach," in *2016 24th Mediterranean Conference on Control and Automation (MED)*. IEEE, jun 2016, pp. 390–395.
- [64] S. Badr, O. Mehrez, and A. E. Kabeel, "A novel modification for a quadrotor design," in *2016 International Conference on Unmanned Aircraft Systems (ICUAS)*. IEEE, jun 2016, pp. 702–710.
- [65] F. Sabatino, *Quadrotor control : modeling, nonlinear control design, and simulation*. Stockholm, Sweden: KTH Royal Institute of Technology in Stockholm, 2015, no. June.
- [66] R. Vepa, *Nonlinear Control of Robots and Unmanned Aerial Vehicles: An Integrated Approach*, 1st ed. London: CRC Press, 2016.
- [67] K. U. Lee, Y. H. Yun, W. Chang, J. B. Park, and Y. H. Choi, "Modeling and Altitude Control of Quad-rotor UAV," in *Proceedings of International Conference on Control, Automation and Systems*, 2011, pp. 1897–1902.
- [68] M. A. Khodja, M. Tadjine, M. S. Boucherit, and M. Benzaoui, "Experimental dynamics identification and control of a quadcopter," in *2017 6th International Conference on Systems and Control (ICSC)*. IEEE, may 2017, pp. 498–502.
- [69] T. Jiřinec, *Stabilization and control of unmanned quadcopter*. Prague, Czech Republic: Czech Technical University in Prague, 2011.
- [70] G. A. Garcia, A. R. Kim, E. Jackson, S. S. Kashmiri, and D. Shukla, "Modeling and flight control of a commercial nano quadrotor," in *2017 International Conference on Unmanned Aircraft Systems (ICUAS)*. IEEE, jun 2017, pp. 524–532.
- [71] Z. Mustapa, S. Saat, A. M. Darsono, and H. H. Yusof, "Experimental Validation of an Altitude Control for Quadcopter," *ARPN Journal of Engineering and Applied Sciences*, vol. 11, no. 6, pp. 3789–3795, 2016.
- [72] M. D. L. Costa De Oliveira, *Modeling, Identification and Control of a Quadrotor Aircraft*. Czech Technical University in Prague, jun 2011.
- [73] T. Koussiouris and G. Kafiris, "Controllability indices, observability indices and the hankel matrix," *International Journal of Control*, vol. 33, no. 4, pp. 773–775, 1981.

- [74] H. Werner, *Lecture Notes - Control Systems Theory and Design*. Hamburg: Hamburg University of Technology, 2012.
- [75] M. Steinbuch and G. Meinsma, *Design Methods for Control Systems*, 2007.
- [76] R. M. Murray, *Optimization-Based Control*. California Institute of Technology, 2009.
- [77] B. Anderson and J. Moore, *Optimal Control, Linear Quadratic Methods*, T. Kailath, Ed. Prentice Hall International, Inc., 1989, vol. 1.
- [78] S. Skogestad and I. Postlethwaite, *Multivariable Feedback Control: Analysis and Design*. John Wiley and Sons, 2001, vol. 2.
- [79] A. Astudillo, P. Munoz, F. Alvarez, and E. Rosero, “Altitude and attitude cascade controller for a smartphone-based quadcopter,” in *2017 International Conference on Unmanned Aircraft Systems (ICUAS)*. IEEE, jun 2017, pp. 1447–1454.
- [80] Android Developer, “SensorEvent,” 2015. [Online]. Available: <https://developer.android.com/>
- [81] K. S. Lauszus, “Flight Controller for Quad Rotor Helicopter in X-configuration,” Bachelor Thesis, Technical University of Denmark, Kongens Lyngby, Denmark, 2015.